# A Tail-Integrated Boundary-Layer Ingesting Propulsion System for Turbo-Electric Aircraft

by

Zhibo Chen
B.S.E., The University of Michigan (Highest Honors) (2020)
B.E., Shanghai Jiao Tong University (Highest Honors) (2020)

Submitted to the Department of Aeronautics and Astronautics
in partial fulfillment of the requirements for the degree of
Master of Science in Aeronautics and Astronautics
at the
MASSACHUSETTS INSTITUTE OF TECHNOLOGY
August 2022

© Massachusetts Institute of Technology 2022. All rights reserved.

Author .....
Department of Aeronautics and Astronautics
August 16, 2022

Certified by .....
Edward M. Greitzer
H. N. Slater Professor of Aeronautics and Astronautics
Thesis Supervisor

Certified by .....
Jayant S. Sabnis
Senior Lecturer of Aeronautics and Astronautics
Thesis Supervisor

Certified by .....
Zoltán S. Spakovszky
T. A. Wilson Professor of Aeronautics and Astronautics
Thesis Supervisor

Accepted by .....
Jonathan P. How
R. C. Maclaurin Professor of Aeronautics and Astronautics
Chair, Graduate Program Committee

# A Tail-Integrated Boundary-Layer Ingesting Propulsion System for Turbo-Electric Aircraft

by

Zhibo Chen

Submitted to the Department of Aeronautics and Astronautics
on August 16, 2022, in partial fulfillment of the
requirements for the degree of
Master of Science in Aeronautics and Astronautics

## Abstract

In this thesis, we present conceptual design guidelines and results for a tail-integrated propulsion system for turbo-electric aircraft with boundary layer ingestion (BLI). This includes (i) definition of tail BLI electric fans and (ii) integration of the BLI propulsors on an aircraft tail, to meet the propulsive power requirements and performance goals, i.e. separation-free and shock-free operation with fuel burn reduction, compared with a baseline aircraft for the same mission. The assessment of BLI benefits incorporates CFD and TASOPT analyses, with emphasis placed on utilizing these analyses not only to identify potential challenges for integration of the BLI propulsors, but also to characterize the underlying mechanisms and thus establish the physical rationale for resolving these challenges.

The conceptual design resulting from the guidelines has nine BLI propulsors with electric fans on an axisymmetric tail, which is installed on a baseline single-aisle aircraft with twin underwing turbofans without BLI. For the tail-integrated BLI electric fans, the guidelines include the required fan loss buckets, and non-axisymmetric stators, to mitigate the fan efficiency drop due to rotor inlet incidence distortion. The design of the tail-integrated propulsor illustrates the aerodynamics of the propulsor inlet, nacelle, and nozzle that enable separation-free and shock-free operation at the cruise condition. The benefit of the defined tail BLI and twin underwing turbofan aircraft configuration is 10.4% in Propulsion Fuel Energy Intensity (PFEI) at a cruise Mach number of 0.8 and an altitude of 35100 ft, compared to a baseline twin underwing turbofan configuration. The sensitivity study shows that a 1% increase in installed (i.e. with BLI) fan efficiency translates to 0.8% rise in the PFEI benefit.

Thesis Supervisor: Edward M. Greitzer
Title: H. N. Slater Professor of Aeronautics and Astronautics

Thesis Supervisor: Jayant S. Sabnis
Title: Senior Lecturer of Aeronautics and Astronautics

Thesis Supervisor: Zoltán S. Spakovszky
Title: T. A. Wilson Professor of Aeronautics and Astronautics

# Acknowledgments

First and foremost, I would like to thank my advisors Prof. Spakovszky, Prof. Greitzer, and Dr. Sabnis for their support during the past two years when the global pandemic impacted everything. They not only offered insightful suggestions and knowledge for the project, but also helped me fit in the new environment and stayed on track with my research, especially during the first year when everything was remote. I would also like to thank Prof. Cumpsty for his advice on this project.

I want to acknowledge my collaborator, Dr. Marshall Galbraith, for his patient support when teaching me how to use all kinds of software to set up geometry, run CFD with SANS on clusters, interrogate flow fields, and write technical reports and papers, through countless emails, Slack messages, and Zoom calls. He always provided helpful and timely suggestions when I was stuck in research, even on weekends.

I am grateful to the team at Mitsubishi Heavy Industries (MHI), Takasago Research & Innovation Center in Japan, especially Imai-san and Yamashita-san for their questions and suggestions during monthly group meetings and/or weekly project meetings. This project could not have happened without the sponsorship of MHI.

I would like to thank all the people at the Gas Turbine Lab (GTL). The weekly social hour on Fridays, either virtual on Zoom or in person on the Building 31 flight deck, always brought me delicious food and happiness when chatting with professors, staff and fellow students. The people at the GTL are like a big family, and I am grateful to their accompany at the lab, in class, and/or after school. A special shoutout goes to the GTL system admins, for their effort enabling us to work remotely during the past two years.

I also owe many thanks to my friends for their encouragement and support that helped me go through the most difficult times. To Jianqiao, Sunbochen, Yuanjie and Zhaosen, it is so great to know you guys before I came to MIT and it is so lucky for me to study and hang out with you again in Cambridge and Boston. To Hanxu, Haoyang and Zhenmei, thank you for visiting me during the Independence Day holiday in 2021. It was one of my best times in the past two years. To Adela, Qian, Ruihan, Xiuneng

and Yang, it is so fortunate for me to meet you guys during these uncertain times. Also, to every friend in my life, thank you for accompanying and supporting me in the past years.

Finally, I want to express my sincerest gratitude to my parents for their endless support throughout this experience. It has been almost three years that I have not been home. Their daily video calls gave me power to overcome mental challenges and all other difficulties during the pandemic. I am always grateful to them for supporting me in studying aerospace in undergraduate years and now at MIT to realize my dream of becoming an aeronautical engineer.

I am looking forward to further exploring the tail BLI propulsion system design during my PhD studies at MIT!

# Contents

**1 Introduction** **21**

1.1 Background and Motivation . . . . . 21

1.2 Thesis Scope . . . . . 23

1.3 Contributions . . . . . 24

**2 Aircraft Mission and Operating Conditions** **25**

2.1 Mission Profile . . . . . 25

2.2 Modified Version of TASOPT for Turbo-Electric Aircraft Configurations 27

2.2.1 Modifications . . . . . 27

2.2.2 Assumptions and Limitations . . . . . 27

2.3 Power Balance Constraint in TASOPT and CFD . . . . . 28

2.4 TASOPT-CFD High-Fidelity Analysis . . . . . 29

2.5 Mission Power Requirement Analysis . . . . . 30

2.6 Cruise Operating Conditions for Baseline Aircraft . . . . . 33

2.7 Cruise Operating Conditions for Tail BLI Aircraft . . . . . 33

**3 Design Concept and Features** **35**

3.1 Integration Concept for Tail BLI . . . . . 35

3.2 Aerodynamic Performance Requirements . . . . . 37

3.2.1 Internal Flow . . . . . 37

3.2.2 External Flow Over The Propulsors . . . . . 38

**4 Design Methodology and Tools** **41**

4.1 Capture of Tail BLI Effects on Fan Performance via Body-Force Modeling 41
4.1.1 Body-Force Model . . . . . 42
4.1.2 Body-Force Camber Surface Parameterization . . . . . 44
4.1.3 Body-Force Camber Surface Optimization . . . . . 45
4.2 Design Tool for Nacelle Profile . . . . . 45
4.3 Overall Conceptual Design Procedure for Integrated Propulsors . . . 46

**5 Design Guidelines for Tail BLI Electric Fans 49**
5.1 Loss Buckets for Tail BLI Fan . . . . . 49
5.1.1 Profile Loss . . . . . 49
5.1.2 Design Guidelines . . . . . 50
5.1.3 Tail BLI Fan Body-Force Camber Surface . . . . . 51
5.1.4 Isentropic Efficiency of Tail BLI Fan in Uniform Flow . . . . . 53
5.1.5 Split of Rotor and Stator Losses Based on Reaction . . . . . 54
5.1.6 Effect of Loss Buckets on Tail BLI Efficiency Penalty . . . . . 55
5.1.7 Fan Map and Efficiency Curves in Uniform Flow and with BLI 58
5.2 Effect of Non-Axisymmetric Stators . . . . . 59

**6 Design Guidelines for Integrated Propulsors 63**
6.1 Tail Design and Propulsor Configuration . . . . . 63
6.1.1 Tail Design . . . . . 63
6.1.2 Propulsor Configuration . . . . . 65
6.2 Computational Domain . . . . . 67
6.3 Inlet Design for BLI . . . . . 68
6.3.1 Design Features and Guidelines . . . . . 68
6.3.2 Inlet Geometry and Flow Behavior . . . . . 69
6.4 Nacelle Design for BLI . . . . . 71
6.4.1 Design Features and Guidelines . . . . . 71
6.4.2 Nacelle Geometry and Flow Behavior . . . . . 71
6.5 Nozzle Design . . . . . 73
6.5.1 Design Features and Guidelines . . . . . 73

6.5.2 Annular Nozzle Design and Flow Behavior . . . . . 75

**7 Tail-Integrated Propulsor Performance 79**

7.1 Fan Responses to Tail BLI Inlet Distortion . . . . . 79

7.2 PFEI Benefit of Tail BLI Aircraft . . . . . 85

7.2.1 Relation between Shaft Power and PFEI . . . . . 85

7.2.2 Sensitivity of PFEI Benefit versus Tail BLI Electric Fan Efficiency 87

7.3 Comparison with Similar Tail BLI Conceptual Aircraft . . . . . 88

**8 Summary and Conclusions 91**

8.1 Primary Learnings . . . . . 91

8.2 Future Work . . . . . 92

**A Mechanical Power and Entropy Generation Ingested by Tail BLI Propulsors 95**

A.1 Non-Dimensionalization in CFD . . . . . 95

A.2 Mechanical Power and Entropy Generation Ingested vs. Propulsor Inlet Area . . . . . 96

**B Body-Force Camber Surface Optimization Framework 99**

B.1 Governing Equations and Turbulence Model . . . . . 99

B.2 Body-Force Camber Surface Optimization Statement . . . . . 100

**C Body-Force Camber Surface Optimization for BLI 103**

**D Tail Boundary Layer Profiles from 3D CFD of a Full Aircraft 107**

**E Geometry of Tail and Tail-Integrated Propulsors 111**

THIS PAGE INTENTIONALLY LEFT BLANK

# List of Figures

1-1 Examples of approaches to defining features of tail-BLI integration (flat plate BLI image from Ref. [4]; duct BLI image from Ref. [17]). These approaches from open literature are helpful for identifying flow issues due to BLI, but they cannot address the in-depth design guidelines for tail-mounted BLI propulsors and BLI fans. . . . . 22

1-2 Tail integration challenges. The upstream influence of the fan affects the evolution of the airframe boundary layer. The counter- and co-swirl at the rotor leading edge cause incidence angle non-uniformities, and possible fan efficiency decrease. . . . . 23

2-1 Schematic of a normal mid-range transport mission flight profile [8]. Cruise from C1 to C2 accounts for 90.6% of the total range. . . . . 26

2-2 Coupling of TASOPT and CFD for high-fidelity assessment of tail-integrated BLI propulsors. In each iteration, the tail BLI fan operating point as the TASOPT input is updated based on CFD calculations, to provide a more appropriate estimate of the fan diameter and propulsive power. . . . . 29

2-3 Schematic of baseline and tail integrated aircraft configurations. The baseline aircraft has twin underwing turbofans. The tail BLI configuration has two smaller underwing turbofans plus nine tail-integrated electric fans. . . . . 31

3-1 Installation of BLI tail with BLI propulsors on the baseline aircraft. To avoid tail strike, the tail profile and the location of tail BLI propulsors were designed to fit the integrated propulsors within the existing non-axisymmetric fuselage outline. . . . . 36

3-2 Comparison of non-axisymmetric and axisymmetric tails which fit in the existing fuselage outline. An axisymmetric tail, as in this thesis, needs to be shorter to avoid tail strike, compared with a non-axisymmetric tail. This increases the design difficulty for tail BLI propulsors on an axisymmetric tail, compared with the non-axisymmetric situation. . . . . 36

3-3 BLI mechanism in terms of internal flows. BLI benefit is a trade-off between propulsive efficiency increase due to ingested mechanical power, and fan shaft power increase due to fan efficiency decrease and higher rotational speed. . . . . 38

3-4 Example of reverse flow upstream of the tail BLI propulsor. An appropriate tail design must eliminate flow separation upstream of the tail BLI propulsors. . . . . 39

3-5 Example of reverse flow between adjacent propulsors with circular nozzles (top view). For the flow channel between propulsors, the exit flow area is three times the inlet flow area, which was excessive diffusion and led to the reverse flow. . . . . 40

3-6 Tail BLI issues in terms of external flows. Tail BLI propulsors need to achieve flow-separation-free operation through the tail, inlet, nacelle, and nozzle design. . . . . 40

4-1 Propulsor local cylindrical coordinates. . . . . 42

4-2 Unit acceleration direction vector. . . . . 42

4-3 Generation of lofted body-force camber surface by a stack of camber lines. . . . . 44

4-4 Parameterization of body-force camber lines by quadratic and cubic Bézier polynomials. . . . . 44

4-5 Parameters for the position of a body-force camber line. $\lambda$: stagger angle, $s$: sweep, $\zeta$: stacking line chord fraction, $c$: chord length, $\Lambda$: lean angle, $r$: radius. . . . . 44

4-6 GUI for design tool of nacelle circumferential profiles. This tool enables real-time adjustment of the nacelle profile by moving control points, i.e. asterisks and circles. . . . . 45

4-7 Single tail-integrated propulsor nacelle generated by profiles (in red) at various circumferential locations. This nacelle design tool enables the design exploration of tail BLI propulsors. . . . . 46

4-8 Design procedure for the tail-integrated propulsor. . . . . 47

5-1 Meridional view of fan flow path in an isolated duct. . . . . 52

5-2 Body-force camber surface optimization for minimizing shaft power at design. . . . . 52

5-3 Optimized body-force camber lines for the tail BLI operating point (left: rotor; right: stator). . . . . 53

5-4 Optimized body-force camber surfaces for rotor and stator. . . . . 53

5-5 Distribution of reaction along the rotor span. . . . . 54

5-6 Efficiency penalties for different fan loss buckets. A fan with a wider low loss region is preferred for the tail BLI. Compared to the design condition, there is a 5.1% efficiency decrease for the fan on the left, and a 7.4% decrease, for the fan on the right. . . . . 56

5-7 Rotor inlet incidence angle variation due to boundary layer ingestion. This incidence swing between $-3^\circ$ and $9^\circ$ is the cause of isentropic efficiency decrease for the tail BLI fan. . . . . 56

5-8 Circumferential distribution of rotor inlet incidence at mid span. $\theta = 0°$ corresponds to the top of the flow annulus and counter-clockwise is the positive direction. The incidence angle swings between 2° and 8.5° with an average about 5°. . . . . 57

5-9 Fan map and efficiency curves of the tail BLI fan in uniform flow. The design point $\delta_0$ is set in the middle of the fan map to ensure stall and choke margins. . . . . 58

5-10 Fan map and efficiency curves of the installed tail BLI fan. The design point $\delta_0$ has an efficiency $\eta = 87.8\%$, so there is an efficiency penalty of 5.1% compared with uniform flow, due to BLI. . . . . 59

5-11 The optimized non-axisymmetric stator has TE flow angle perturbations about 100° out of phase with rotor LE incidence variation (angles in degrees). . . . . 60

5-12 Stator TE pressure perturbations 90° out of phase with flow angle perturbations (static pressure normalized by freestream stagnation pressure; flow angles in degrees). This out-of-phase angle is consistent with the Cauchy-Riemann relation between static pressure perturbations and flow angle perturbations. . . . . 61

5-13 Limited influence of non-axisymmetric stator on rotor incidence variation (angles in degrees). . . . . 61

5-14 Majority of rotor relative flow is supersonic at the rotor leading edge. This causes the the stator pressure field upstream influence to be limited on the rotor incidence variation. . . . . 62

6-1 Centerline: axisymmetric tail with top and bottom BLI propulsors. . 64

6-2 Left hand side shows various tube-and-wing airframe profiles. btail refers to the transition from the constant-radius fuselage. Right hand side shows TASOPT based boundary layer edge Mach number at different axial locations for various tail profiles. At 90% of fuselage length, the boundary layer edge Mach number $M_e$ is approximately 0.7 for a range of tail shapes. . . . . 64

6-3 Centerline view of the tail and integrated propulsor with dimensions. 65

6-4 No separation upstream of tail BLI propulsors. This meets the design requirement of the tail transition upstream of the tail BLI propulsors. 65

6-5 Isometric view of tail BLI propulsors looking downstream. . . . . 66

6-6 Contours of axial Mach number at centerline for tail-integrated propulsor. The boundary layer edge streamline coming from the end of constant-radius fuselage enters the propulsor inlet at the top, with the local edge Mach number approximately 0.7. This tail design achieved the desired boundary layer edge Mach number at the propulsor inlet. 67

6-7 Computational domain for tail-integrated propulsor. This wedge-shaped domain and boundary conditions enable the CFD to be carried out in reduced computation cost, with flow conditions consistent with the full configuration. . . . . 68

6-8 Streamline curvature below the inlet lip results in local flow acceleration. The curvature of the inlet lip should be controlled to achieve no shock at cruise. . . . . 69

6-9 Sketch of centerline profile of the tail-integrated propulsor. . . . . 70

6-10 Calculations show no reverse flow and no shock in the vicinity of propulsor inlet. The cross-section cut at the inlet throat shows that the local axial Mach number ranges from 0.3 to unity, and is reverse-flow-free and shock-free at the station. This inlet design meets the design requirements. . . . . 70

6-11 Centerline: weak shock on nacelle surface. The maximum stagnation pressure drop across the shock is 0.5%. The nacelle outer contour similar to the profiles of supercritical airfoils achieves low-loss operation on the nacelle surface at cruise. . . . . 72
6-12 Internal flow passage absolute Mach number: acceleration achieved from stator TE to nozzle exit, with this non-axisymmetric nacelle design. 72
6-13 Non-uniform absolute Mach number at the annular nozzle exit. The highest Mach number is 1.3, at the top, due to the curvature of the local nacelle profile. In regions closer to left and right sides of the nozzle, the flow Mach number is around unity. . . . . 73
6-14 Geometry of integrated propulsors with circular nozzles. . . . . 74
6-15 Reverse flow at the circular nozzle exit, due to excessive diffusion between adjacent propulsors. . . . . 74
6-16 Top view of nacelles with circular nozzles. The ratio of the exit flow cross-section to the inlet flow cross-section is approximately 3, which results in excessive diffusion and thus flow separation. . . . . 75
6-17 Side view of the annular nozzle. . . . . 76
6-18 Rear view of the annular nozzle. . . . . 76
6-19 Mach number contour showing flow between adjacent nacelles. No flow separation is seen. Jagged edges of contour plots are due to finite mesh. This annular nozzle achieves flow-separation-free operation between nacelles at cruise. . . . . 77
6-20 Non-uniform axial Mach number at the annular nozzle exit. No flow separation is seen. This annular nozzle achieves flow-separation-free operation at the nozzle exit at cruise. . . . . 77
6-21 Top view of nacelle with the annular nozzle. The ratio of the exit flow cross-section to the inlet flow cross-section is approximately 1.4. This area ratio is less than half of that for the flow channel between nacelles with circular nozzles, leading to much less diffusion and no flow separation between adjacent nacelles. . . . . 78

7-1 Stagnation pressure non-uniformity at station a), propulsor inlet (non-circular); station b), rotor LE; station c), rotor TE; station d), stator TE. The change in the stagnation pressure non-uniformity pattern across the stage is due to the non-uniform rotor loading caused by the incidence variation. . . . . 80

7-2 Attenuation of axial velocity non-uniformity across fan, due to the higher impact of the favorable pressure gradient on the lower-velocity flow. Station a), propulsor inlet (non-circular); station b), rotor LE; station c), rotor TE; station d), stator TE. . . . . 82

7-3 Static pressure at station a), propulsor inlet (non-circular); station b), rotor LE; station c), rotor TE; station d), stator TE. . . . . 83

7-4 Flow angle and swirl non-uniformity at the stator trailing edge. . . . 84

7-5 Swirl non-uniformity at the nozzle exit. The increase in the magnitude of the flow swirl (vorticity) is because of the decrease in flow passage area at the nozzle exit compared with the stator trailing edge. Because swirl flow reduces the propulsive efficiency, guidelines to reduce the nozzle exit swirl should be considered in future work. . . . . 85

7-6 Sensitivity of PFEI benefit versus tail BLI electric fan installed efficiency by TASOPT analysis. A 1% increase in tail BLI electric fan efficiency leads to a BLI benefit increase of approximately 0.8%. . . 88

A-1 Concentric cuts at nacelle highlight to determine relation of mechanical power and entropy generation ingested vs. propulsor inlet area. . . . 96

A-2 Two types of tail necking profiles for tail BLI propulsors. . . . . 97

A-3 Relation between mechanical power ingested $P_{K,inl}$ and propulsor inlet area. An S-shaped tail profile is preferred because of the larger $P_{K,inl}$. 97

A-4 Relation between entropy ingested and propulsor inlet area. The S-shaped profile has larger mass-flow average ingested entropy than that for the arc-shaped tail for a propulsor inlet height equal to the local boundary layer thickness. . . . . 98

C-1 Boundary layer profile at the tail propulsor inlet is used as the inflow boundary condition for isolated duct, to enable the tail BLI fan design in an environment consistent with the tail-integrated propulsor. . . . 103
C-2 Comparison of baseline and optimized body-force camber lines. . . . . 104
C-3 Changes in body-force camber lines between optimized and baseline. The changes in the rotor body-force camber lines are smaller than changes in the stator body-force camber lines. . . . . 105
C-4 Stagnation pressure more uniform at rotor TE for optimized than baseline. This implies more attenuation of stagnation pressure non-uniformity by the optimized rotor than the baseline. . . . . 106

D-1 Meridional contour of Mach number. Boundary layer profile extracted at $x = 27.9m$, i.e. the end of constant-radius fuselage. Figure courtesy of MHI. . . . . 108
D-2 Seven circumferential locations to extract boundary layer profiles. Figure courtesy of MHI. . . . . 108
D-3 CFD boundary layer approximations by 2D Coles profile. The approximation by the 2D Coles boundary layer profile is 99% accurate in terms of the kinetic energy deficit at all the circumferential locations except 90°. . . . . 109

E-1 Centerline profiles of the axisymmetric tail with top and bottom BLI propulsors. Actual dimensions included. . . . . 111
E-2 Side view of the axisymmetric tail with integrated BLI propulsors. . . 112
E-3 Front view of the axisymmetric tail with integrated BLI propulsors. The tail upstream of the integrated propulsors is hidden to make the propulsors visible. . . . . 112
E-4 Rear view of the axisymmetric tail with integrated BLI propulsors. . 113

# List of Tables


2.1 Mission definitions. . . . . 25

2.2 Mission stages. . . . . 26

2.3 TASOPT input and output parameters for baseline aircraft. . . . . 31

2.4 TASOPT input and output parameters for electric fans on tail BLI aircraft. . . . . 32

2.5 Cruise operating conditions for baseline aircraft. . . . . 33

2.6 Cruise operating conditions for underwing turbofans on the tail BLI aircraft. . . . . 34

2.7 Cruise operating conditions for electric fans on the tail BLI aircraft. . 34

7.1 Power, propulsive efficiency, and PFEI breakdown for baseline and tail BLI aircraft, respectively. . . . . 86

THIS PAGE INTENTIONALLY LEFT BLANK

# Chapter 1

# Introduction

## 1.1 Background and Motivation

Boundary layer ingestion (BLI) and distributed propulsion (DP) are two important technologies for new aircraft configurations, particularly electrified aviation. Integrated propulsor concepts using BLI and DP can be enabled by high-power density motors, supplied with power from batteries, from a generator driven by a gas turbine, or from a combination [7, 19].

Much of the BLI literature has focused on assessing the impact on aircraft performance. For example, and relevant to the present work, analyses of regional and medium haul size tube-and-wing aircraft configurations indicate that tail-mounted electric propulsors with BLI can reduce the fuel energy consumption per payload range [19]. A major challenge that is, as yet, less addressed is the guiding principles for integration of BLI propulsion systems on an airframe to achieve performance benefit. BLI integration studies in existing literature include two main approaches to tail-BLI integration: integration on flat plate and integration on a notional tail to examine design with BLI, as illustrated by Figure 1-1. Two results from these are that the propulsor inlet should accommodate BLI inlet distortion without incurring flow separation [15] and that a non-axisymmetric stator can have the potential to reduce the incidence angle non-uniformity and thus the efficiency penalty [18]. Tse et al. [28] also conclude that tail-BLI propulsors with circular nozzles have flow sepa-

ration near nozzle exits, another issue to be resolved. These learnings are helpful for identifying flow issues associated with boundary layer ingestion, but as mentioned, in-depth design guidelines for tail-mounted BLI propulsors and BLI fans are yet to be addressed. The present thesis aims at this issue.

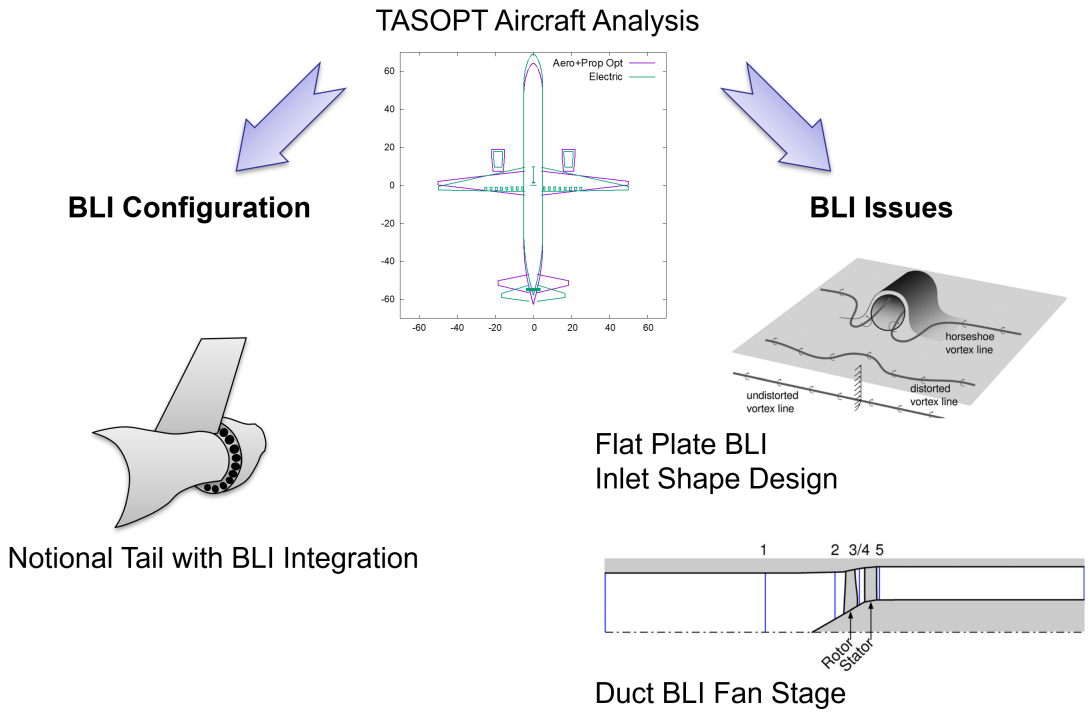



Figure 1-1: Examples of approaches to defining features of tail-BLI integration (flat plate BLI image from Ref. [4]; duct BLI image from Ref. [17]). These approaches from open literature are helpful for identifying flow issues due to BLI, but they cannot address the in-depth design guidelines for tail-mounted BLI propulsors and BLI fans.

There are other integration challenges as well. One is the coupling of external and internal flows as in Figure 1-2, where the upstream influence of the fan affects the evolution of the airframe boundary layer. Second is the counter- and co-swirl at the rotor leading edge, associated with the streamline vorticity created as shown in Figure 1-1, which causes incidence angle non-uniformities, and possible fan efficiency decrease. Finally, to achieve low-loss operation, i.e. reverse-flow-free and shock-free, at cruise, it is essential to determine the appropriate geometry of the propulsor inlet, nacelle, and nozzle for tail-mounted BLI propulsors.

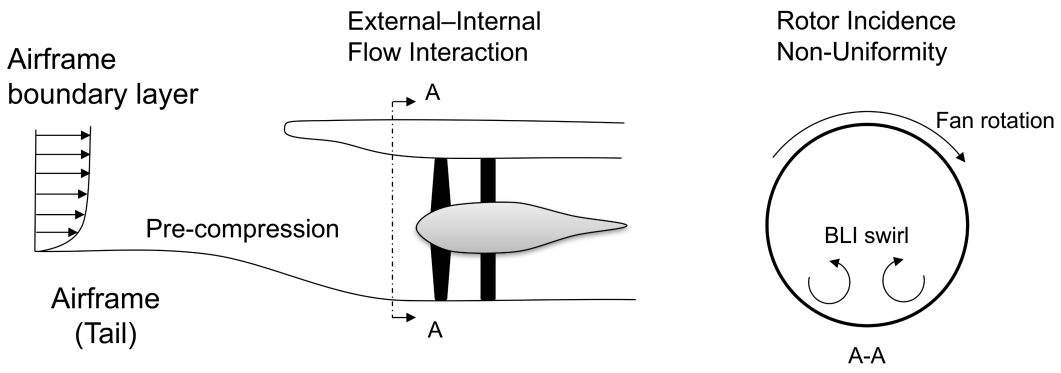



Figure 1-2: Tail integration challenges. The upstream influence of the fan affects the evolution of the airframe boundary layer. The counter- and co-swirl at the rotor leading edge cause incidence angle non-uniformities, and possible fan efficiency decrease.

## 1.2 Thesis Scope

This thesis describes design guidelines for integration of BLI propulsors on a tail for specific propulsive power requirements and presents the results of a successful integration based on the guidelines. A body-force turbomachinery model is used for capturing the effects of tail BLI integration on fan performances and parametric representation of propulsor geometry is utilized for tail BLI propulsor integration. The Transport Aircraft System OPTimization (TASOPT)[1] analysis is used for determining the specific propulsive power to set for the operating point of tail BLI propulsors. The metric used for the vehicle is Propulsion Fuel Energy Intensity(PFEI), defined as the ratio of total fuel heating value to the payload weight per range. Because the engine shaft power determines the rate of fuel burn, minimizing shaft power subject to a specific propulsive power is equivalent to optimizing aircraft fuel consumption and thus PFEI. Therefore, the fan stage is optimized for minimal shaft power, at design, with BLI and the tail-integrated propulsor is designed for shock-free and separation-free operation at cruise.

The research questions to be answered are:

- Given that a BLI/DP aircraft configuration has, conceptually, better fuel burn

[1]TASOPT is a software package for evaluation of future aircraft configurations based on low-order models using fundamental aerodynamic, thermodynamic, and structural mechanics theories [7].

than a conventional configuration, for the same mission, what is the quantitative improvement in the propulsive efficiency and PFEI for aircraft with a tail-mounted propulsor array?

- What is the impact of inlet distortion on fan performance? What approach is needed in fan aerodynamic design to meet BLI performance goals?

- What are design guidelines for the inlet, nacelle, and nozzle of tail-mounted BLI propulsors?

## 1.3 Contributions

There are three main contributions of this thesis:

- The benefit of a "tail BLI and twin underwing turbofan" single-aisle aircraft configuration is determined to be 10.4% in PFEI at a cruise Mach number of 0.8 and an altitude of 35100 ft, compared with a baseline aircraft configuration with twin turbofans. Further, it has been shown that 1% increase in BLI installed fan efficiency corresponds to approximately 0.8% PFEI benefit.

- Design guidelines have been established for tail-integrated BLI propulsors, with an annular nozzle, to achieve separation-free and shock-free operation at cruise. Based on the guidelines, a successful integration of BLI propulsors on an axisymmetric tail is created for the mission.

- A high-fidelity assessment of BLI benefits has been carried out, incorporating CFD and TASOPT analyses, which provides guidelines for BLI fans to mitigate the efficiency penalty due to rotor incidence non-uniformity.

# Chapter 2

# Aircraft Mission and Operating Conditions

## 2.1 Mission Profile

The definition of the mid-range civil transport aircraft mission considered in this thesis is given in Table 2.1. The mission, for both the tail BLI and baseline aircraft, is carrying 38700 lb of payload over a 3000 nmi range. The underwing engines for the two types of aircraft are low-FPR(Fan Pressure Ratio) turbofans[1] for the best possible efficiency.

| Technology Level | Cruise Mach Number | Range | Payload |
|---|---|---|---|
| Tail BLI & Twin Underwing Turbofans | 0.8 | 3000 nmi | 38700 lb |
| Baseline Twin Underwing Turbofans | 0.8 | 3000 nmi | 38700 lb |

Table 2.1: Mission definitions.

Table 2.2 and Figure 2-1 show the schematic of a normal mission flight profile, with range, $R$, as the abscissa and altitude, $h$, as the ordinate.

The cruise from C1 to C2 consumes 86% of fuel for the mission[2], and thus the analyses for aircraft performances, i.e. propulsive efficiency and PFEI, are based on

[1]The description of low-FPR turbofan performance is based on existing open literature about geared turbofans (GTF) and consideration of technology advancement by the time frame for introduction of tail BLI aircraft.

[2]Based on the TASOPT analysis for mission fuel consumption.

cruise operating conditions. Moreover, due to the small difference between C1 and C2, the aircraft cruise operating conditions are taken as the stage C1[3].

| | |
|---|---|
| ST | Start of take-off roll |
| RO | Rotation |
| TO | Take-off |
| CB | Cutback thrust level |
| B1 | Start of climb |
| B2-B4 | Climb points |
| B5 | End of climb |
| C1 | Start of cruise |
| C2 | End of cruise |
| D1 | Start of descent |
| D2-D4 | Descent points |
| D5 | End of descent: touch-down |

Table 2.2: Mission stages.

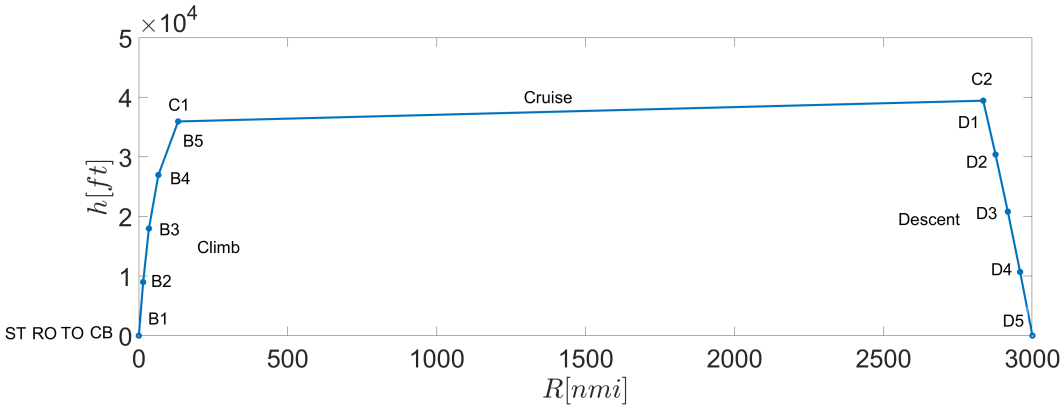



Figure 2-1: Schematic of a normal mid-range transport mission flight profile [8]. Cruise from C1 to C2 accounts for 90.6% of the total range.

[3]Analyzed by TASOPT.

## 2.2 Modified Version of TASOPT for Turbo-Electric Aircraft Configurations

### 2.2.1 Modifications

In this project, the public version 2.16 of TASOPT [8] was modified[4] to expand the capabilities to analyze turbo-electric configurations, including both wing and tail mounted electric fans with BLI. On top of the public version, this modified version has tightly coupled on-design turbofan and electric-fan sizing, electrical component weight estimates based on power densities, improved turbofan weight models for low-FPR turbofans and LPT weight for electrification. This modified version of TASOPT was used for assessing the baseline aircraft and exploring the benefits of different BLI configurations. It was found[5] that a mid-range civil aircraft has the highest improved efficiency from adding tail-mounted electric-fans with BLI.

### 2.2.2 Assumptions and Limitations

The assumption made in the TASOPT 1D propulsion system analysis, pertaining to our application, is the uniformity of flow quantities. This assumption is appropriate for the underwing turbofans which see uniform flows, but it does not hold well for tail-integrated BLI propulsors. The tail BLI electric fans see flow distortion and this non-uniformity cannot be captured by the TASOPT 1D analysis, so CFD calculations were used to complement TASOPT[6]. Besides, TASOPT cannot include the geometry information of the tail and tail BLI propulsors in its analysis. It cannot estimate changes in the mechanical power and entropy, ingested by the tail BLI propulsors, when the propulsor size varies, for a specific tail design. To overcome this limitation, we added the models of ingested mechanical power and entropy as functions of the tail BLI propulsor size, as inputs to TASOPT analyses[7].

[4]Implemented by Dr. Marshall Galbraith. This modified version is not available to the public at the time of this thesis.

[5]Work by Dr. Marshall Galbraith.

[6]More information is in Section 2.4.

[7]More information is in Section 2.4 and 2.5.

## 2.3 Power Balance Constraint in TASOPT and CFD

A power balance is utilized in both TASOPT and CFD to determine the fan operating point. At this condition, the airframe surface dissipation[8] is balanced by the net propulsor power $P_{prop}$ [6]. The statement of this condition is:

$$P_{prop} \equiv P_K + P_{V_{inl}} - \Phi_{jet}, \tag{2.1}$$

In Equation 2.1, $P_K$ is the net mechanical power into the propulsor, $P_{V_{inl}}$ is the pressure-volume work from the aircraft nose to the inlet of tail BLI propulsors, and $\Phi_{jet}$ is the jet dissipation downstream of the propulsor nozzles.

The terms in Equation 2.1 are computed in the CFD calculations as [6]

$$P_K = \int_{exit} [p - p_\infty + \frac{1}{2}\rho(V^2 - V_\infty^2)]\mathbf{V} \cdot \hat{n}\, dS - \int_{inl} [p - p_\infty + \frac{1}{2}\rho(V^2 - V_\infty^2)]\mathbf{V} \cdot \hat{n}\, dS, \tag{2.2}$$

$$\Phi_{jet} = \int_{exit} [(p - p_\infty)(\mathbf{V} - \mathbf{V}_\infty) \cdot \hat{n} + \frac{1}{2}\rho|\mathbf{V} - \mathbf{V}_\infty|^2 \mathbf{V} \cdot \hat{n}]\, dS, \tag{2.3}$$

$$P_{V_{inl}} = \iiint (p - p_\infty)\nabla \cdot \mathbf{V}\, d\mathcal{V}_{inl}. \tag{2.4}$$

The surface integrals are evaluated over the propulsor inlet and exit survey planes with the unit normal $\hat{n}$ pointing outward from the propulsor. The volume integral $P_{v_{inl}}$ is evaluated over the streamtube volume from the inflow boundary to the propulsor inlet $\mathcal{V}_{inl}$[9].

In TASOPT, the term $\Phi_{inl}$ defined in Equation 2.5 is evaluated based on an integral boundary layer analysis (IBL) [8]:

$$\Phi_{inl} = -\int_{inl} [p - p_\infty + \frac{1}{2}\rho(V^2 - V_\infty^2)]\mathbf{V} \cdot \hat{n}\, dS + \iiint (p - p_\infty)\nabla \cdot \mathbf{V}\, d\mathcal{V}_{inl} \tag{2.5}$$

[8]Surface dissipation for the entire aircraft.

[9]Information about the computation domain is in Chapter 6.

## 2.4 TASOPT-CFD High-Fidelity Analysis

For the baseline aircraft, whose propulsors see freestream, the inflow is circumferentially uniform. A one-dimensional analysis based on fan operating conditions, such as that in TASOPT, thus provides a useful estimation of the shaft power required for specified propulsive power. For the BLI electric fans in the tail-integrated propulsors, however, the inflow has a stratified[10] stagnation pressure distribution, so the fans see non-uniform flow. With the tail BLI propulsors, there is also an interaction between internal and external flows, creating a potential for reverse flows on the tail and propulsor surfaces. A one-dimensional analysis thus cannot be assumed to provide an appropriate assessment of the tail BLI flow features and benefits. For the tail-integrated propulsors with BLI, 3D RANS CFD has been paired with TASOPT to provide a high-fidelity analysis of propulsive power and shaft power for BLI propulsors. This coupling is depicted conceptually in Figure 2-2.

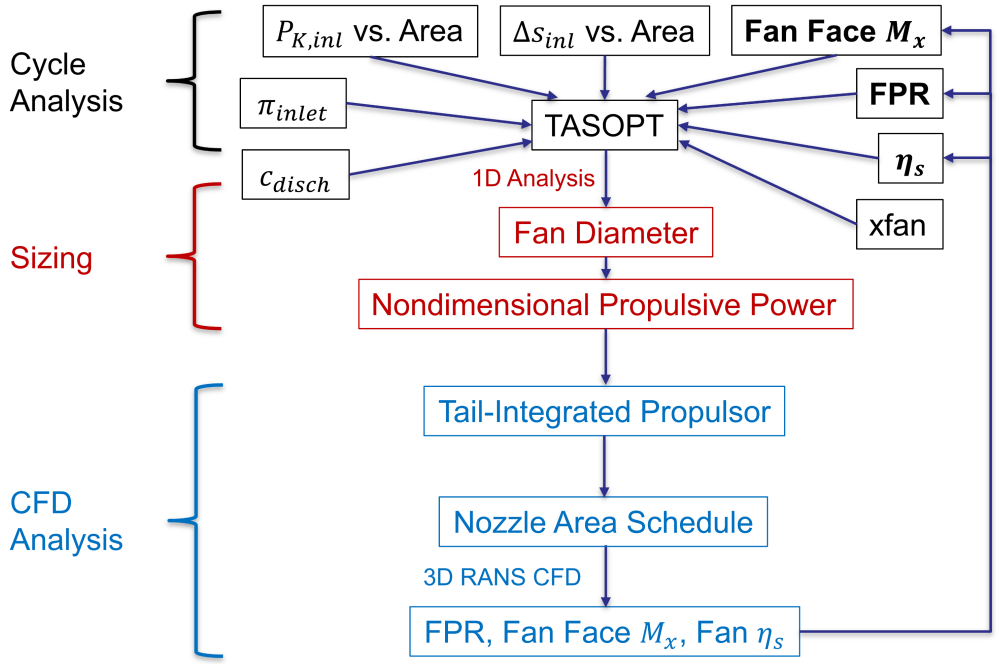



Figure 2-2: Coupling of TASOPT and CFD for high-fidelity assessment of tail-integrated BLI propulsors. In each iteration, the tail BLI fan operating point as the TASOPT input is updated based on CFD calculations, to provide a more appropriate estimate of the fan diameter and propulsive power.

[10]Stratified with respect to distance from the fuselage.

The computations modeled the tail section of the aircraft only, to achieve faster turnaround for design exploration, and we thus rely on TASOPT to obtain the net required propulsive power $P_{prop}$. The set of parameters described in Tables 2.3 and 2.4 are TASOPT inputs for estimation of the required propulsive power. Due to the effect of boundary layer ingestion on fan performance, the fan operating point needs to be determined from CFD for the specified propulsive power and fan pressure ratio estimated by TASOPT. Using the updated information of the fan operating point from CFD, TASOPT can then update its estimation of the tail BLI propulsive power. After several iterations, changes in the propulsive power analyzed by TASOPT converge to zero, giving us an appropriate estimation of the tail BLI fan operating conditions.

## 2.5 Mission Power Requirement Analysis

The baseline aircraft configuration in this study has twin underwing turbofans as in the upper sketch of Figure 2-3. The tail BLI configuration has two smaller underwing turbofans plus nine tail-integrated electric fans, as in the lower sketch. For the tail BLI aircraft, the gas generators of the underwing turbofans power all the electric fans as well as turbofans. The number of tail BLI propulsors was determined by setting the propulsor inlet diameter (approximately) equal to the local boundary layer thickness[11].

Table 2.3 shows the selected set of input and output parameters of the engines and flight conditions for the baseline aircraft with underwing turbofans. The fan operating point is characterized by the pressure ratio, fan face Mach number and isentropic efficiency. The fan leading edge (LE) hub-to-tip ratio (HTR) is used in fan diameter sizing. The propulsor inlet pressure recovery and nozzle discharge coefficient quantify the aerodynamic losses due to the propulsor inlet and nozzle, respectively. The ratio of the propulsor wetted area to the fan face area is used for weight estimation of propulsors.

[11] More information is in Chapter 6.

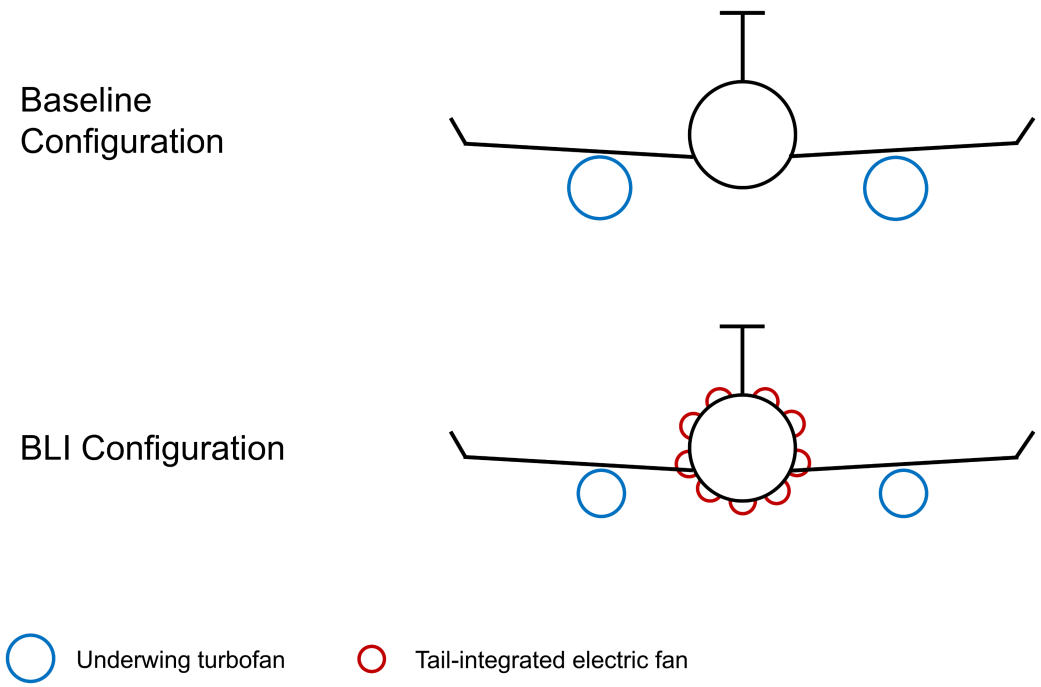



Figure 2-3: Schematic of baseline and tail integrated aircraft configurations. The baseline aircraft has twin underwing turbofans. The tail BLI configuration has two smaller underwing turbofans plus nine tail-integrated electric fans.

| Input Parameters (Turbofans) | Output Parameters |
|---|---|
| Fan Pressure Ratio | Fan Diameter |
| Fan Face Mach Number | Fan Mass Flow |
| Isentropic Efficiency | Propulsive Power |
| Fan LE HTR | Shaft Power |
| Inlet Pressure Recovery | Propulsive Efficiency |
| Nozzle Discharge Coefficient | TSFC |
| Bypass Ratio | |
| Propulsor Wetted Area / Fan Area | |
| Flight Mach Number | |

Table 2.3: TASOPT input and output parameters for baseline aircraft.

Table 2.4 shows the analogous set of input and output parameters for the tail BLI aircraft with underwing turbofans and tail-integrated electric fans. For the underwing turbofans, the set of parameters is the same as in Table 2.3, but for the electric fans Table 2.4 has three extra input parameters: the propulsor inlet location relative to tail tip (i.e. the end of tail), the mechanical power $P_{K,inl}$[12] and the mass-flow average

[12]This term comes from a power balance, as described in Section 2.3.

entropy generation, $\Delta s_{inl}$, relative to freestream, ingested by the integrated propulsor, as a function of the inlet area with BLI.

| Input Parameters (Electric Fans) | Output Parameters |
|---|---|
| Fan Pressure Ratio | Fan Diameter |
| Fan Face Mach | Fan Mass Flow |
| Isentropic Efficiency | Propulsive Power |
| Fan LE HTR | Shaft Power |
| Inlet Pressure Recovery | Propulsive Efficiency |
| Nozzle Discharge Coefficient | |
| Bypass Ratio | |
| Propulsor Wetted Area / Fan Area | |
| Propulsor Inlet Relative to Tail Tip | |
| Flight Mach Number | |
| $P_{K,inl}$ vs. Area | |
| $\Delta s_{inl}$ vs. Area | |

Table 2.4: TASOPT input and output parameters for electric fans on tail BLI aircraft.

The location of the tail BLI propulsor inlet is important in determining the inflow conditions. The mechanical power, $P_{K,inl}$, ingested by the propulsor inlet is defined in Equation 2.6. The mass-flow average entropy generation, $\Delta s_{inl}$, quantifies the stagnation pressure loss caused by ingesting the airframe boundary layer. This loss results in a higher-FPR tail BLI fan than the fans under the wing, which see uniform flow. Equation 2.7 relates the fan face stagnation pressure to entropy generation, $\Delta s_{inl}$, through the Gibbs equation[13].

$$P_{K,inl} = -\int_{inl} [p - p_\infty + \frac{1}{2}\rho(V^2 - V_\infty^2)]\mathbf{V} \cdot \hat{n}\, dS, \tag{2.6}$$

$$p_{t,fan} = p_{t,\infty} e^{(-\Delta s)},\ \Delta s = \frac{1}{\dot{m}} \iint [\frac{\gamma}{\gamma - 1} log(\frac{h}{h_\infty}) - log(\frac{p}{p_\infty})]\rho\mathbf{V} \cdot \hat{n}\, dS. \tag{2.7}$$

[13]Heat capacity ratio is assumed to be 1.4.

## 2.6 Cruise Operating Conditions for Baseline Aircraft

The cruise operating conditions for baseline aircraft are summarized in Table 2.5.

| Input Parameters (Turbofans) | | Output Parameters (Single Fan) | |
|---|---|---|---|
| Fan Pressure Ratio | 1.35 | Fan Diameter | 86 in |
| Fan Face Mach | 0.618 | Fan Mass Flow | 235 kg/s |
| Isentropic Efficiency | 0.930 | Propulsive Power | 4972 kW |
| Fan LE HTR | 0.375 | Shaft Power | 6063 kW |
| Inlet Pressure Recovery | 0.9995 | Propulsive Efficiency | 0.820 |
| Nozzle Discharge Coefficient | 0.9863 | TSFC | 0.513/hr |
| Bypass Ratio | 12.5 | | |
| Propulsor Wetted Area / Fan Area | 16.0 | | |
| Flight Mach Number | 0.80 | | |

Table 2.5: Cruise operating conditions for baseline aircraft.

## 2.7 Cruise Operating Conditions for Tail BLI Aircraft

Based on the TASOPT-CFD high-fidelity assessment described in Section 2.4, the cruise operating conditions for the tail BLI aircraft are summarized in Table 2.6 and Table 2.7 for the underwing turbofans and the electric fans, respectively. Curve fits for $P_{K,inl}$ vs. inlet area and $\Delta s_{inl}$ vs. inlet area are in Appendix A.

| Input Parameters (Turbofans) | | Output Parameters (Single Fan) | |
|---|---|---|---|
| Fan Pressure Ratio | 1.35 | Fan Diameter | 64 in |
| Fan Face Mach | 0.618 | Fan Mass Flow | 123 kg/s |
| Isentropic Efficiency | 0.930 | Propulsive Power | 2838 kW |
| Fan LE HTR | 0.375 | Shaft Power | 3347 kW |
| Inlet Pressure Recovery | 0.9995 | Propulsive Efficiency | 0.848 |
| Nozzle Discharge Coefficient | 0.986 | TSFC | 0.514/hr |
| Bypass Ratio | 12.5 | | |
| Propulsor Wetted Area / Fan Area | 16.0 | | |
| Flight Mach Number | 0.80 | | |

Table 2.6: Cruise operating conditions for underwing turbofans on the tail BLI aircraft.

| Input Parameters (Electric Fans) | | Output Parameter (Single Fan) | |
|---|---|---|---|
| Fan Pressure Ratio | 1.50 | Fan Diameter | 24 in |
| Fan Face Mach | 0.60 | Fan Mass Flow | 16 kg/s |
| Isentropic Efficiency | 0.878 | Propulsive Power | 517 kW |
| Fan LE HTR | 0.375 | Shaft Power | 560 kW |
| Inlet Pressure Recovery | 0.995 | Propulsive Efficiency | 0.876 |
| Nozzle Discharge Coefficient | 0.957 | | |
| Bypass Ratio | 12.5 | | |
| Propulsor Wetted Area / Fan Area | 10.33 | | |
| Nacelle Inlet Relative to Tail Tip | 16.8 ft | | |
| Flight Mach Number | 0.80 | | |
| $P_{K,inl}$ vs. Area | Curve Fit | | |
| $\Delta s_{inl}$ vs. Area | Curve Fit | | |

Table 2.7: Cruise operating conditions for electric fans on the tail BLI aircraft.

# Chapter 3

# Design Concept and Features

## 3.1 Integration Concept for Tail BLI

The baseline aircraft represents a B737-800 with low-FPR turbofans. The tail BLI aircraft is adapted from the baseline aircraft with a circumferential array of BLI propulsors mounted on the rear tail as in Figure 3-1[1]. To avoid tail strike, the tail profile and the location of tail BLI propulsors have been designed to fit the integrated propulsors within the existing non-axisymmetric fuselage outline.

The design adopted had an axisymmetric tail with nine identical tail BLI propulsors. This was done for two main reasons. First, using the axisymmetric tail enables us to partition the computation domain into $N_{prop}$ identical sub-domains, with $N_{prop}$ the number of tail-integrated propulsors. CFD simulations could thus be executed in one sub-domain, shortening the turnaround time to speed up the design exploration. Second, and more important, designing tail BLI propulsors with an axisymmetric tail does not lower the level of difficulty for design. The tail transition needs to be shorter than a non-axisymmetric tail to avoid tail strike and fit in the existing fuselage outline, as depicted in Figure 3-2. A shorter tail is more likely to result in flow separation upstream of the tail BLI propulsor inlet. Hence, a BLI propulsor design for the axisymmetric tail that meets performance goals should be appropriate for

[1]This figure shows a single-aisle mid-range airplane. The underwing turbofan in the figure does not represent the low-FPR engine to be used on the baseline aircraft.

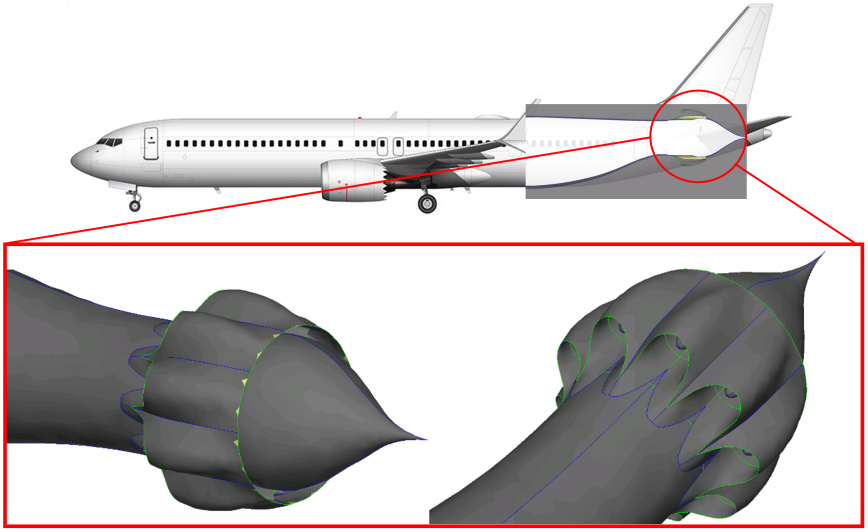


Figure 3-1: Installation of BLI tail with BLI propulsors on the baseline aircraft. To avoid tail strike, the tail profile and the location of tail BLI propulsors were designed to fit the integrated propulsors within the existing non-axisymmetric fuselage outline.

a non-axisymmetric tail. Finally, the critical learnings from the axisymmetric tail analysis should be well transferable for the non-axisymmetric situation.

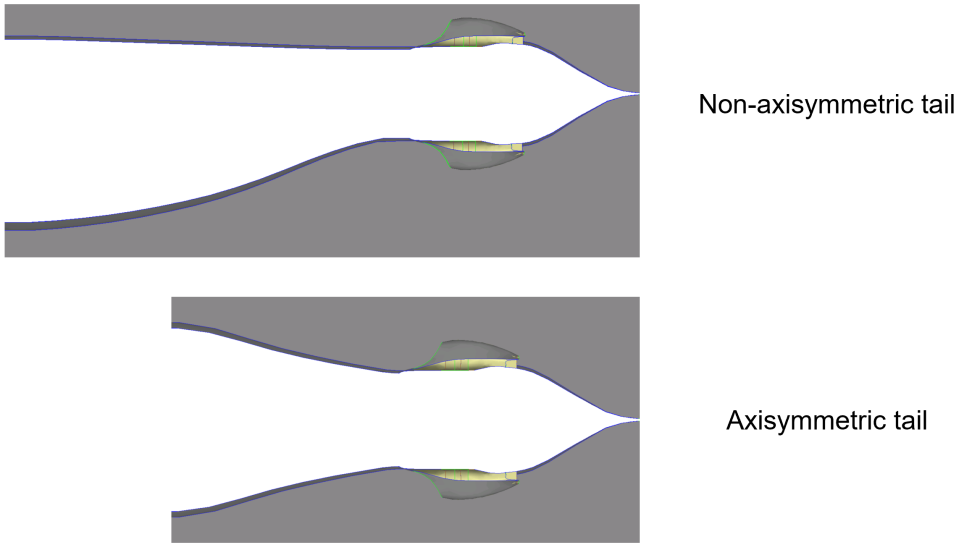



Figure 3-2: Comparison of non-axisymmetric and axisymmetric tails which fit in the existing fuselage outline. An axisymmetric tail, as in this thesis, needs to be shorter to avoid tail strike, compared with a non-axisymmetric tail. This increases the design difficulty for tail BLI propulsors on an axisymmetric tail, compared with the non-axisymmetric situation.

## 3.2 Aerodynamic Performance Requirements

### 3.2.1 Internal Flow

The number of tail-integrated propulsors depends on the target for airframe boundary layer ingestion. There is a trade between capturing boundary layer and increasing weight[2]. The configuration adapted has nine BLI propulsors mounted on the tail, with an inlet diameter approximately equal to the height of the local boundary layer[3]. With this amount of ingestion, the flow at the propulsor inlet is non-uniform, both radially and circumferentially, in stagnation pressure. The inlet distortion causes incidence angle variations at the rotor leading edge plane, resulting in a penalty on stage isentropic efficiency [9, 10]. Numbers quoted in literature for the isentropic efficiency drop vary from 1.5% [9], to 6% [10], 8% [28] or 10% [13] depending on the fan design and the inlet distortion[4]. The BLI benefit in fuel consumption is sensitive to the fan efficiency [26], and it is thus critical to design a fan with low efficiency penalty for incidence swings due to inlet distortion.

Because the stagnation pressure of the boundary layer is lower than freestream, a higher pressure ratio and a higher fan rotational speed are required for the tail BLI fan than for a fan in uniform flow, to produce the required propulsive power. In this aspect, BLI benefit is a trade-off between propulsive efficiency increase due to ingested mechanical power[5], and fan shaft power increase due to fan efficiency decrease and higher rotational speed. The elements that come into this trade are illustrated in Figure 3-3.

[2]If the tail BLI propulsors are too large, the total propulsion system weight of the tail BLI aircraft will be greater than the baseline. That may result in more fuel burn for the tail BLI aircraft than the baseline.

[3]More information about the tail BLI propulsor sizing for the target amount of boundary layer ingestion is described in Chapter 6.

[4]This will be discussed further in Chapter 5.

[5]This means lower jet kinetic energy for a given thrust.

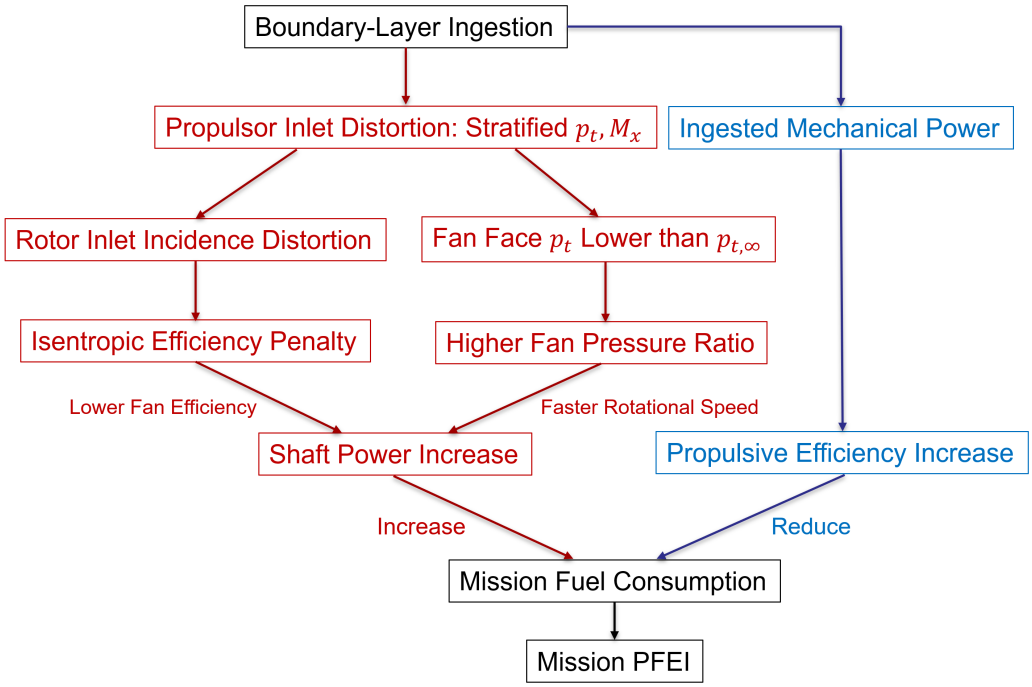



Figure 3-3: BLI mechanism in terms of internal flows. BLI benefit is a trade-off between propulsive efficiency increase due to ingested mechanical power, and fan shaft power increase due to fan efficiency decrease and higher rotational speed.

### 3.2.2 External Flow Over The Propulsors

The tail-integrated propulsors affect boundary-layer evolution on the aft-portion of the airframe because of upstream static pressure influence. The transition section between the constant-radius fuselage and the rear tail, where the BLI propulsors are mounted, should be designed to minimize adverse pressure gradients upstream of the propulsors. A smooth transition between the tail and the propulsor is required to avoid reverse flow due to an abrupt transition, which can increase losses and cause a penalty on the overall propulsive efficiency. An example of an inappropriate tail with substantial reverse flow upstream of the BLI propulsor (encountered in the early design exploration) is shown in Figure 3-4. The figure shows contours of the axial Mach number on the propulsor centerline plane, tail surface out of the centerline plane, and streamlines illustrating the reverse flow upstream of the propulsor. The contour plane of mostly green is at the propulsor centerline, with the tail profile highlighted by the black solid line. The contour of mostly blue and purple is on the

tail surface out of the propulsor centerline plane. The region of dark purple contours corresponds to the region of reverse flow, with the axial Mach number about -0.1.

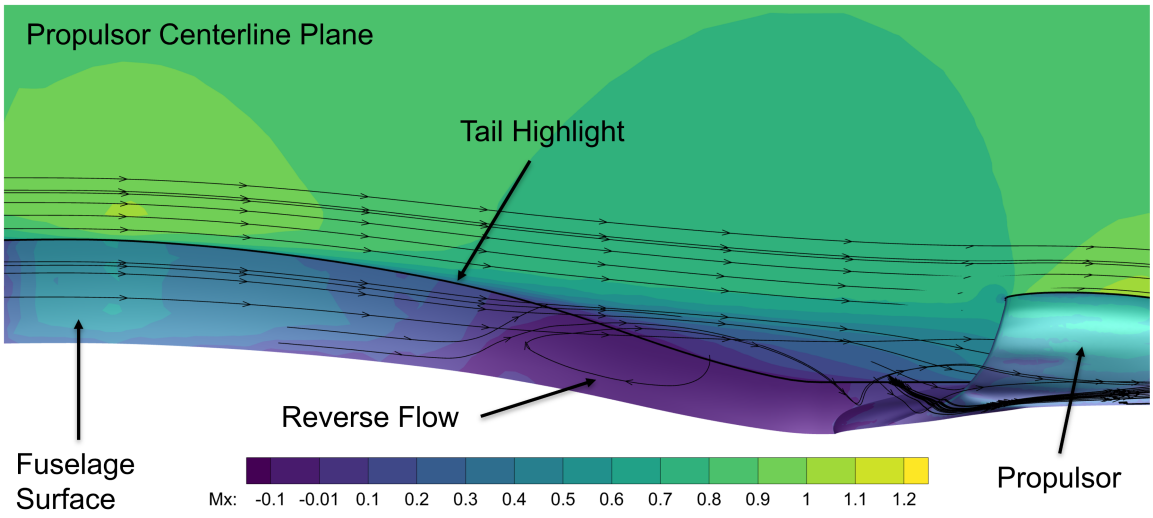



Figure 3-4: Example of reverse flow upstream of the tail BLI propulsor. An appropriate tail design must eliminate flow separation upstream of the tail BLI propulsors.

The channel between adjacent propulsors can also give rise to reverse flow due to excessive diffusion. With circular nozzles, for example, there is a diverging section between propulsors as one approaches the nozzle exit, because of the smaller nozzle exit area compared with the propulsor inlet area. The diffusion due to this diverging channel may become excessive and induce flow separation between adjacent propulsors [28]. An appropriate nacelle and nozzle design for tail BLI propulsors should avoid this flow separation. Figure 3-5 shows an example of reverse flow between adjacent propulsors with circular nozzles. For this configuration (another result of the initial exploration), the exit flow area is three times the inlet flow area, which was excessive diffusion and led to the reverse flow.

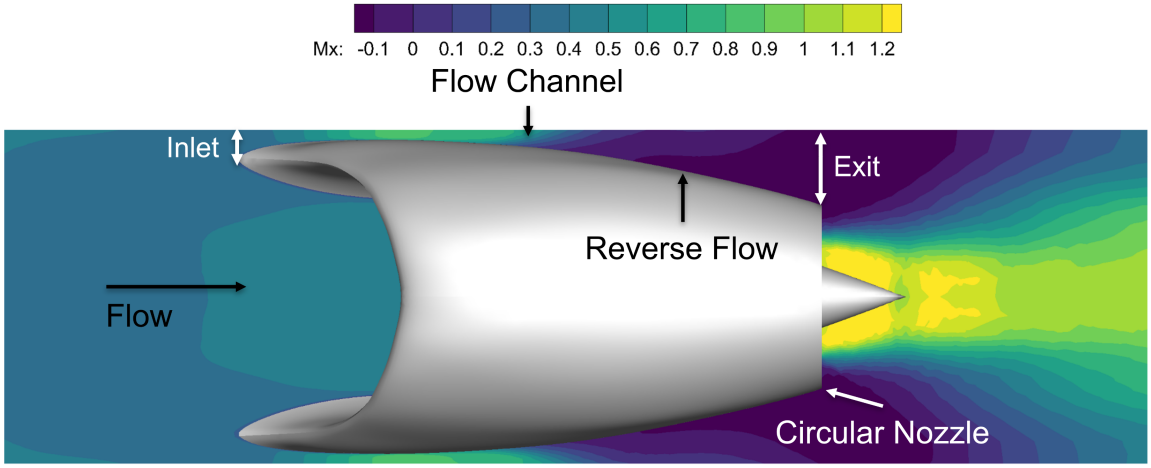



Figure 3-5: Example of reverse flow between adjacent propulsors with circular nozzles (top view). For the flow channel between propulsors, the exit flow area is three times the inlet flow area, which was excessive diffusion and led to the reverse flow.

Figure 3-6 lists the external flow issues and solutions in the integration of the BLI propulsors on a tail for these two aspects.

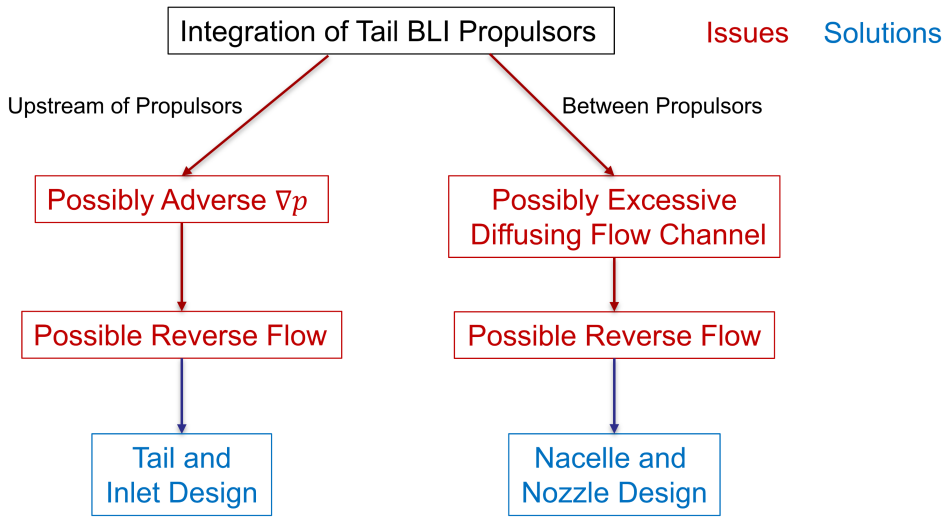



Figure 3-6: Tail BLI issues in terms of external flows. Tail BLI propulsors need to achieve flow-separation-free operation through the tail, inlet, nacelle, and nozzle design.

# Chapter 4

# Design Methodology and Tools

## 4.1 Capture of Tail BLI Effects on Fan Performance via Body-Force Modeling

One method to capture the effects of BLI on fan performances is to explicitly create blades with meshes, but this is expensive in terms of computation cost. Direct meshing of blades does not lend itself to iteratively modify the geometry within a reasonable amount of time, so embedding it in an optimization framework for maximizing fan efficiency is not feasible. A 3D body-force model, as used here, represents the effect of flow turning and viscous losses through a volumetric force field without meshing geometry and thus captures the impact of BLI on fan performance with much reduced computation cost [17, 30]. This reduced computation cost allows more rapid turnaround for the design space exploration.

The 3D body-force model involves a *body-force camber surface* plus a loss model. The body-force camber surface is a different concept from the camber surface of an actual blade. The body-force camber surface is used for defining the normal and tangential directions for local body-force vectors only, and it does NOT represent an actual blade geometry. It is constructed by stacking a series of body-force camber lines at various radial locations. To simplify the nomenclature, any mentioned rotor, stator, or fan thus means the corresponding body-force field. An actual blade is not

in the scope of this thesis.

### 4.1.1 Body-Force Model

The body-force model[1] is implemented in the Solution Adaptive Numerical Simulator (SANS) framework that was established by Galbraith et al. [11]. The normal component of the body-force vector, $\vec{\mathrm{f}}_\mathrm{n}$, follows that of Hall et al. [17]. For a specific propulsor, the axis of rotation is defined by a Cartesian point and a unit direction vector. The axis of rotation is then used for defining local cylindrical coordinates $\hat{\xi}$[2], $\hat{r}$, and $\hat{\theta}$ as in Fig. 4-1, where $\vec{r}$ is normal to the axis of rotation, and the blade rotational velocity is

$$\vec{U} = \Omega \left|\vec{r}\right| \hat{\theta}. \tag{4.1}$$

To prevent entropy generation, the direction of an inviscid body-force vector must be perpendicular to the local relative velocity vector, $\vec{W} = \vec{V} - \vec{U}$ [17, 30]. The unit inviscid body-force vector $\hat{\mathrm{f}}_\mathrm{n}$ is computed as

$$\hat{\mathrm{f}}_\mathrm{n} = \hat{W} \times \left(\hat{W} \times \hat{n}\right), \tag{4.2}$$

where $\hat{W} \times \hat{n}$ is the vector that defines the plane shared by the body-force normal vector $\hat{n}$ and the relative velocity vector $\hat{W}$ as in Figure 4-2.

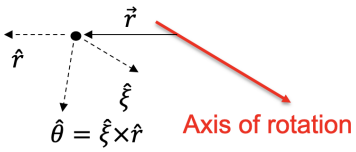



Figure 4-1: Propulsor local cylindrical coordinates.

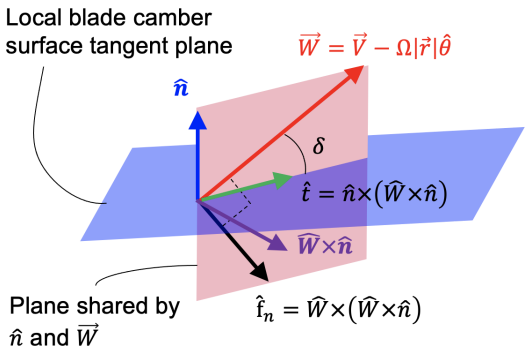



Figure 4-2: Unit acceleration direction vector.

[1] Implemented by Dr. Marshall Galbraith.
[2] Symbol ˆ denotes a unit vector.

The pressure force loading is modeled based on the description of Hall [17] using a thin airfoil theory approach. The local lift coefficient, $c_l$, is given by $c_l = 2\pi\delta$, where $\delta$ is the local relative flow deviation defined as the angle between the relative velocity vector $\vec{W}$ and the body-force tangent vector, $\hat{t} = \hat{n} \times (\hat{W} \times \hat{n})$. The angle $\delta$ is expressed as

$$\delta = \arctan\left(\vec{W} \cdot \hat{n}, \vec{W} \cdot \hat{t}\right). \tag{4.3}$$

The inviscid body-force vector component is thus

$$\vec{\mathsf{f}}_{\mathsf{n}} = \hat{\mathsf{f}}_{\mathsf{n}} \frac{2\pi\delta\left(\frac{1}{2}\vec{W}^2 / \left|\hat{n} \cdot \hat{\theta}\right|\right)}{2\pi\left|\vec{r}\right| / B}. \tag{4.4}$$

The formulation of the viscous body-force component follows the work of Gong[16] and Chen[3]. The viscous body-force is defined as

$$\vec{\mathsf{f}}_{\mathsf{v}} = -\hat{W} \frac{K_p\left(\frac{1}{2}\vec{W}^2 / \left|\hat{n} \cdot \hat{\theta}\right|\right)}{2\pi\left|\vec{r}\right| / B}. \tag{4.5}$$

The function $K_p$ is modeled as

$$K_p = c_D(K_{p0} + K_{\delta 1}\delta + K_{\delta 2}\delta^2 + K_{\delta 3}\delta^3 + K_{\delta 4}\delta^4 + K_{r1}s_r + K_{r2}s_r^2 + K_{r3}s_r^3 + K_{r4}s_r^4) \tag{4.6}$$

where $c_{\mathcal{D}} = 0.0024$, as suggested by Denton [5] for a diffusing boundary layer and $s_r$ stands for the span ratio (ratio of radial location to tip radius). The dependence of $K_p$ on the span ratio is used for modeling the reaction at different radial locations to split the losses between the rotor and stator appropriately. The deviation angle $\delta$ is also included in the definition of $K_p$ to allow the representation of blade loss versus incidence, or loss buckets. Fourth powers for both $\delta$ and $s_r$ allow flexible control of loss buckets and split of losses between the rotor and stator. More information is in Chapter 5.

### 4.1.2 Body-Force Camber Surface Parameterization

Figure 4-3 shows an example of body-force camber surface defined by body-force camber lines at various radial locations. Each body-force camber line is defined by quadratic or cubic Bézier polynomials with the inlet and exit angles as free variables. Figure 4-4 shows that for a quadratic Bézier curve, the inlet and exit angles are the same, both denoted by $\gamma_1$. For a cubic body-force camber line, the inlet angle is different from the exit angle, so they are marked as $\gamma_1$ and $\gamma_2$, respectively. Once a body-force camber line is defined by a Bézier polynomial, it can be positioned in a desired way using the parameters illustrated in Figure 4-5.

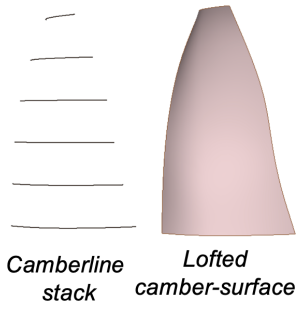



Figure 4-3: Generation of lofted body-force camber surface by a stack of camber lines.

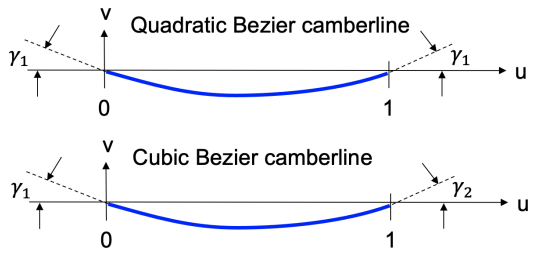



Figure 4-4: Parameterization of body-force camber lines by quadratic and cubic Bézier polynomials.

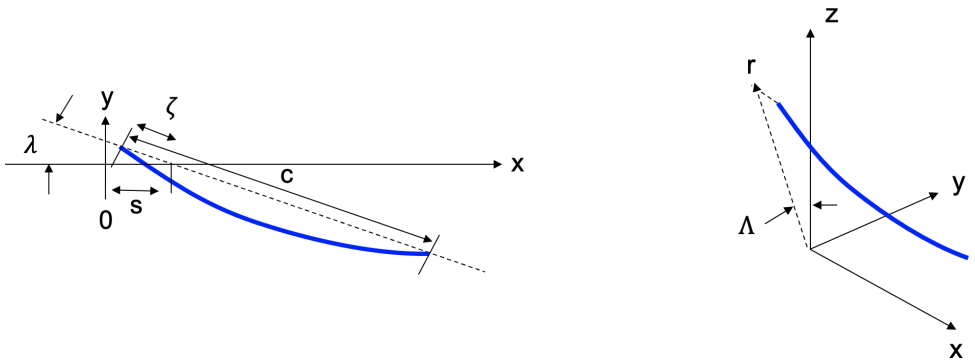



Figure 4-5: Parameters for the position of a body-force camber line. $\lambda$: stagger angle, $s$: sweep, $\zeta$: stacking line chord fraction, $c$: chord length, $\Lambda$: lean angle, $r$: radius.

### 4.1.3 Body-Force Camber Surface Optimization

The body-force model is embedded in the body-force camber surface optimization framework in SANS, which optimizes the camber surface to achieve minimal shaft power at a given operating point, defined by the fan face axial Mach number and pressure ratio. Appendix B provides additional information about the governing equations and optimization statement.

## 4.2 Design Tool for Nacelle Profile

To allow a flexible design process for the integrated propulsor, a design tool[3] was created for real-time interaction with the design of the different nacelle profiles that are needed at different circumferential locations for each propulsor. Those profiles are defined by Kulfan's universal representation of airfoils based on Bernstein polynomials [21].

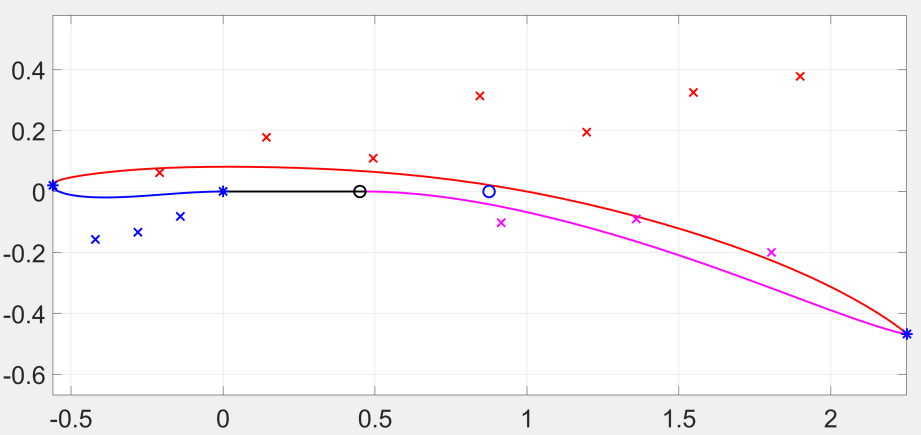



Figure 4-6: GUI for design tool of nacelle circumferential profiles. This tool enables real-time adjustment of the nacelle profile by moving control points, i.e. asterisks and circles.

Figure 4-6 is an example of the Graphical User Interface (GUI) for the nacelle design tool. The horizontal axis is the streamwise location and the vertical axis is the radial location, both normalized by the propulsor inlet diameter. The red crosses

[3]Initially established and implemented by Dr. Marshall Galbraith and revised by Zhibo Chen.

represent the coefficients of Bernstein polynomials for the upper nacelle contour (also given in red), whose individual values can be read from the ordinate. Similarly, the blue and magenta crosses stand for the Bernstein coefficients for the lower nacelle contours, in blue and in magenta, respectively. All the crosses can be moved up and down to control the shapes of corresponding sections of the nacelle profile. The curvature at the leading edge is controlled by a black hollow circle, whose abscissa is equal to the corresponding coefficient in Bernstein polynomials. The trailing edge curvature is controlled by a blue hollow circle. Both black and blue hollow circles can be moved horizontally to change the values of corresponding Bernstein coefficients. Parametric propulsor nacelles are generated by profiles at various circumferential locations, as in Figure 4-7, which is for a single propulsor.

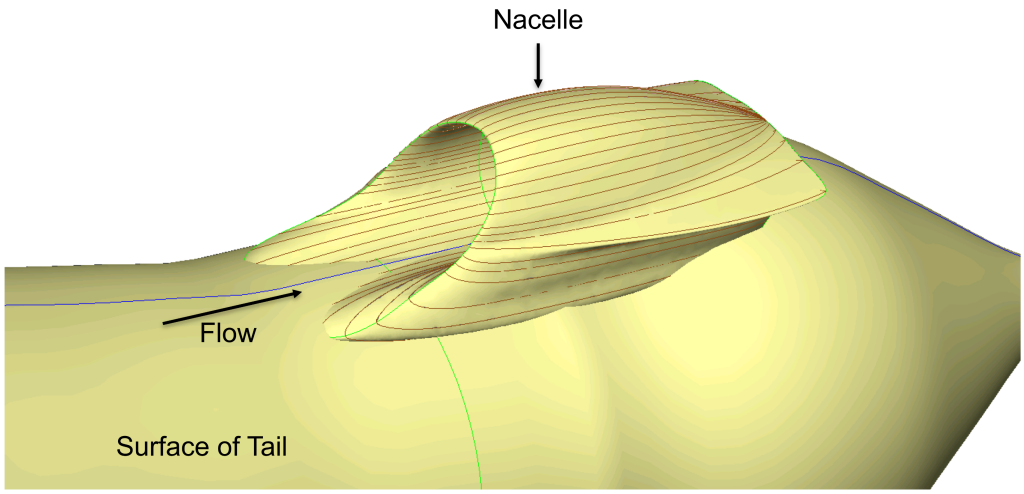



Figure 4-7: Single tail-integrated propulsor nacelle generated by profiles (in red) at various circumferential locations. This nacelle design tool enables the design exploration of tail BLI propulsors.

## 4.3 Overall Conceptual Design Procedure for Integrated Propulsors

Figure 4-8 depicts the conceptual design procedure for the integrated propulsors on the tail BLI aircraft. The TASOPT analysis determines the aircraft sizing and the specifications of the propulsors for the mission. To establish a propulsor design that

satisfies those requirements, we explore the design space of the propulsor configuration, inlet, nacelle, nozzle, and fan stage, with the exploration based on the body-force model and internal-external flow coupled computations. A power balance is utilized for setting the operating point of the tail BLI fan. The body-force camber surface optimization framework yields an optimal fan stage, defined as having minimized shaft power at design. The BLI benefits are quantified by comparing PFEI between the baseline and tail BLI aircraft configurations for the same mission.

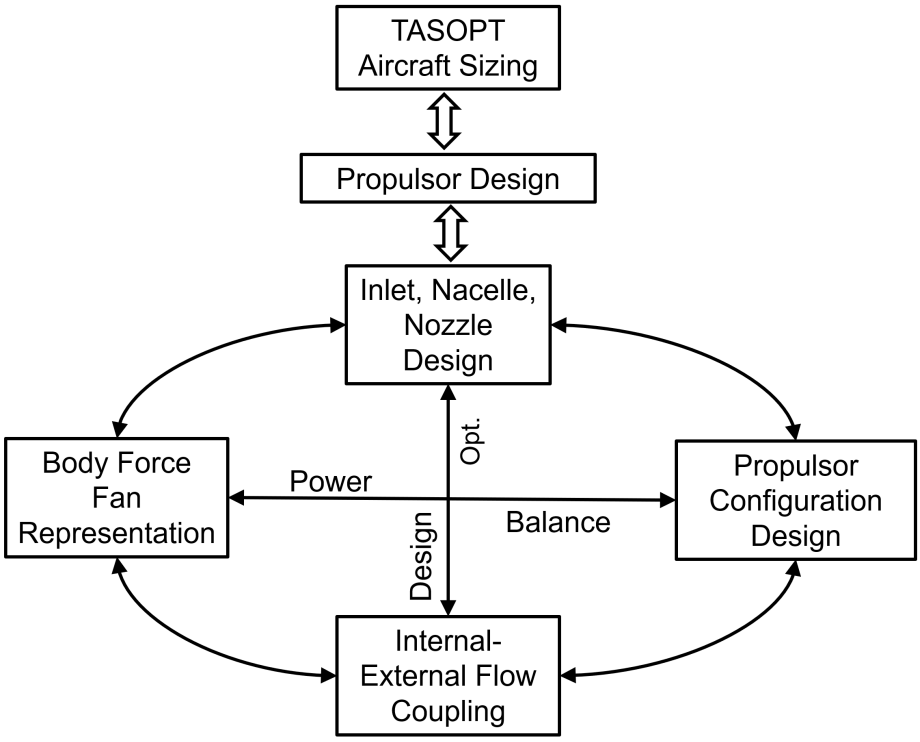



Figure 4-8: Design procedure for the tail-integrated propulsor.

THIS PAGE INTENTIONALLY LEFT BLANK

# Chapter 5

# Design Guidelines for Tail BLI Electric Fans

In Chapter 3, we discussed the aerodynamic requirements for a tail BLI fan and introduced a central issue for boundary layer ingesting turbomachinery, the inlet distortion and thus incidence angle variation, and local operation away from the aerodynamic design condition. This, in turn, results in reduced isentropic efficiency compared with the same fan in uniform flow. The PFEI benefit of BLI depends on the fan efficiency, and a design requirement is a fan with low loss for incidence angle excursions. In this chapter, we discuss the effects of rotor loss buckets on the fan efficiency, and examine the idea of using non-axisymmetric stators to reduce rotor incidence variation.

## 5.1 Loss Buckets for Tail BLI Fan

### 5.1.1 Profile Loss

The variations in profile loss coefficient with incidence, for rotors and stators, represent the aerodynamic responses of the turbomachinery to the range of inlet incidence angles. The loss coefficient, $\omega$, is defined in terms of the change in rotary stagnation pressure $p_{t_{rot}}$ from the leading edge to the trailing edge, and the leading edge relative

dynamic pressure $p_{t_{rel,LE}} - p_{LE}$. The variables to be used are

$$\omega = \frac{p_{t_{rot,LE}} - p_{t_{rot,TE}}}{p_{t_{rel,LE}} - p_{LE}}, \tag{5.1}$$

$$p_{t_{rot}} = p[1 + \frac{\gamma - 1}{2}(M_{rel}^2 - M_u^2)]^{\frac{\gamma}{\gamma-1}}, \tag{5.2}$$

$$p_{t_{rel}} = p[1 + \frac{\gamma - 1}{2}M_{rel}^2]^{\frac{\gamma}{\gamma-1}}, \tag{5.3}$$

$$M_{rel} = \frac{W}{\sqrt{\gamma RT}}, \tag{5.4}$$

$$M_u = \frac{\Omega r}{\sqrt{\gamma RT}}. \tag{5.5}$$

In Equations 5.4 and 5.4, $W$ is the relative velocity for the blade row of interest, rotor or stator, $\Omega$ is the rotor angular rotational speed, and $r$ is the radial location. The heat capacity ratio $\gamma$ is assumed to be 1.4 in this thesis.

The rotary stagnation pressure, $p_{t_{rot}}$, accounts for the centrifugal field due to radial streamline shifts. It is conserved along a streamline in the relative frame if there are no viscous losses, and its reduction from the leading edge to trailing edge indicates the losses. For stators, the rotary stagnation pressure reduces to the absolute stagnation pressure.

In the body-force model, the force component parallel to the relative streamlines models entropy generation due to viscous losses. The formulation of the parallel body-force component was defined by Equation 4.5, with function $K_p$ (Equation 4.6) determining the viscous loss as a function of incidence angles and for different radial locations. The body-force camber surface, coupled with the loss model $K_p$, represents the effects of flow turning and viscous losses.

### 5.1.2 Design Guidelines

Body-force modeling of the loss buckets of a tail BLI fan stage needs to satisfy the following requirements:

- Realistic representation of viscous losses: Isentropic efficiency of the tail BLI fan in uniform flow should be representative of actual, or at least conceptual,

blading. In this project, we have set the tail BLI fan to have the same polytropic efficiency as that assumed in the open literature for a geared turbofan, based on isentropic efficiency of 93% at a fan pressure ratio (FPR) of 1.35 [23, 24].

- Appropriate split of losses between rotor and stator: We have set the ratio of rotor loss to be equal to the reaction, i.e. the ratio of static enthalpy rise across the rotor to the static enthalpy rise across the stage. The tail BLI electric fan, i.e. a single stage, has rotor inlet flow with zero absolute swirl and a stage exit flow with nearly zero swirl. This type of axial-flow fan has a high reaction, typically above 70% [2, 22]. The ratio of rotor loss to total loss is set as 73.5% for our tail BLI fan in uniform flow.

- Low efficiency drop[1] due to BLI: A wide low loss region for the rotor loss bucket. A fan designed for tail BLI should have a low efficiency penalty over the local rotor incidences encountered. For the propulsion system examined here, the PFEI benefit was 10.4% for a fan that had an efficiency drop of 5.1% due to BLI. For each 1% increase in tail BLI installed fan efficiency, there was approximately 0.8% PFEI benefit[2].

### 5.1.3 Tail BLI Fan Body-Force Camber Surface

The tail BLI fan design is carried out in an isolated duct with an inflow boundary layer profile corresponding to the inlet of a tail-integrated propulsor[3]. The hub-to-tip ratios for the rotor LE, rotor TE, and stator TE are 0.375, 0.520, and 0.590, respectively. A meridional view of the duct is given in Figure 5-1.

A body-force camber surface optimization process is utilized to select the body-force camber surface to minimize shaft power at the design point with boundary layer ingestion. The process is depicted in Figure 5-2. For the design point, the

[1]The installed fan efficiency needs to yield positive BLI benefits compared with the baseline aircraft.

[2]The sensitivity study is described in Chapter 7.

[3]Further information about the boundary layer profile is in Appendix C.

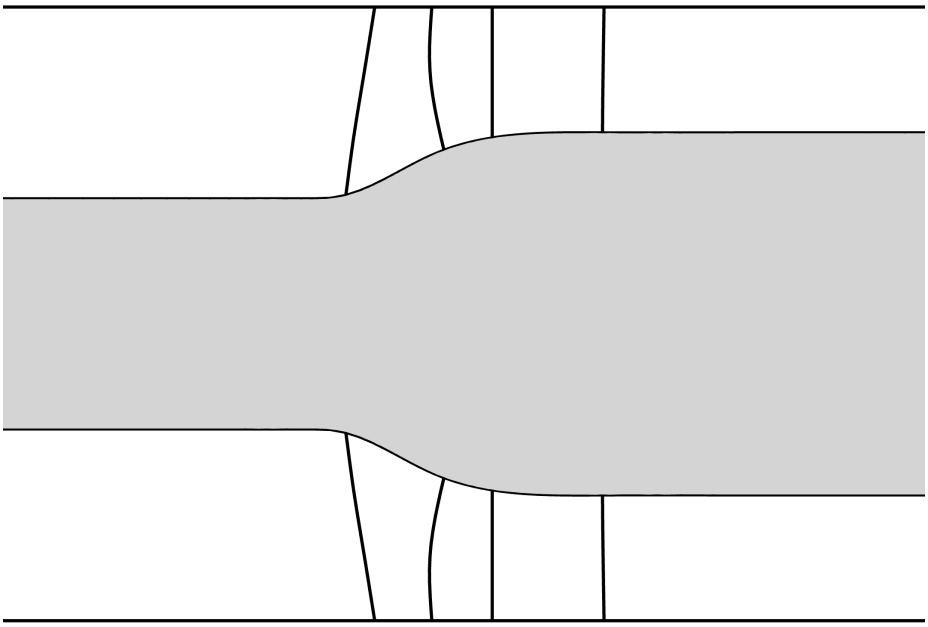


Figure 5-1: Meridional view of fan flow path in an isolated duct.

fan face axial Mach number and FPR are set to 0.60 and 1.50[4], respectively. The $K_p$ coefficients are defined by Equations 5.9 and 5.10, respectively. More detail concerning body-force camber surface optimization is in Appendix C.

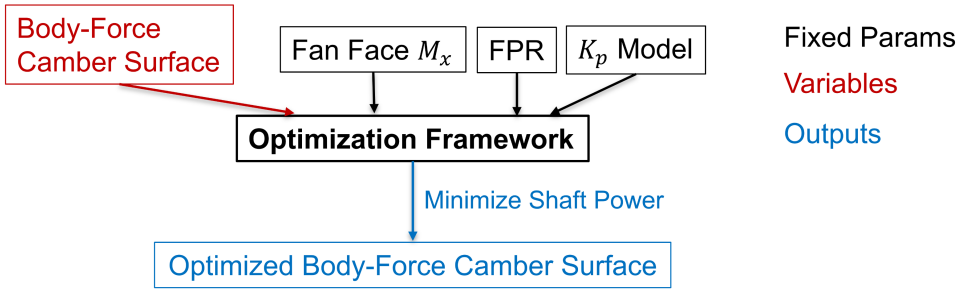



Figure 5-2: Body-force camber surface optimization for minimizing shaft power at design.

The optimized set of body-force camber lines are shown in Figure 5-3. The rotor is on the left and the stator is on the right. Sections 0, 1, and 2 represent locations near the root, at mid span, and near the tip, respectively. The abscissa corresponds to the axial direction and the ordinate to the tangential direction, with dimensions normalized by fan diameter. The surfaces that result from the optimized body-force

[4]FPR is set by the ratio of static back pressure to inflow total pressure in the isolated duct

camber lines for rotor and stator are shown in Figure 5-4.

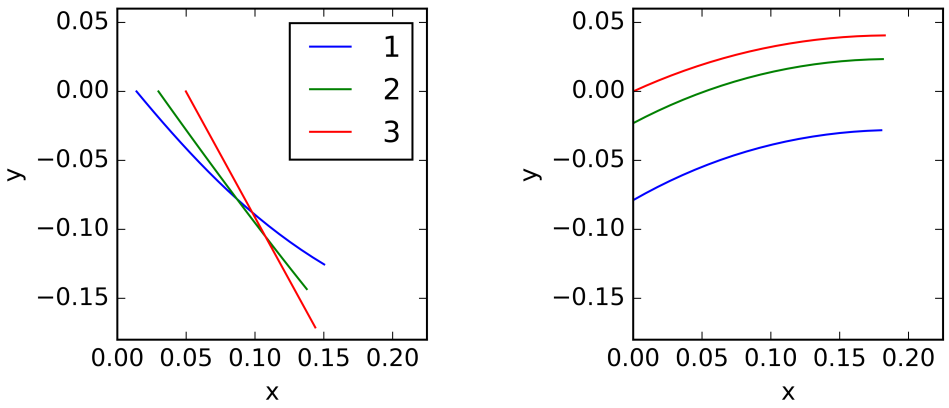



Figure 5-3: Optimized body-force camber lines for the tail BLI operating point (left: rotor; right: stator).

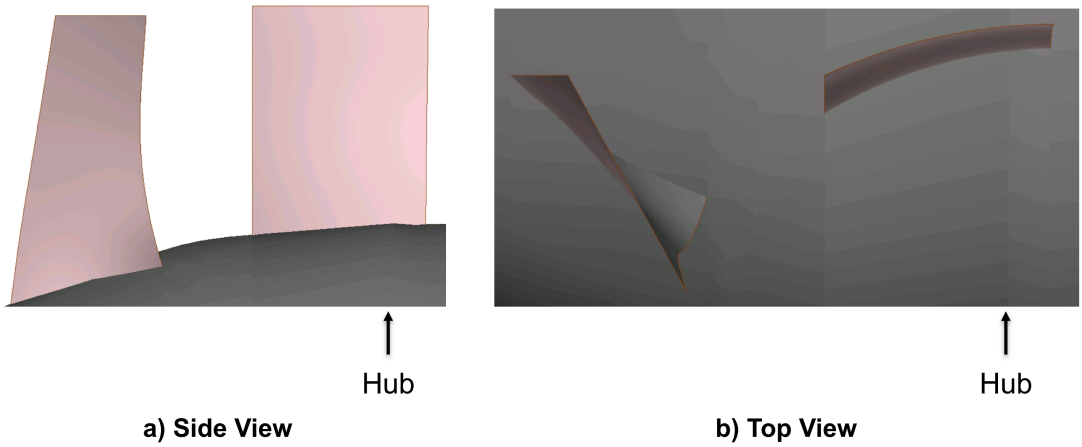



Figure 5-4: Optimized body-force camber surfaces for rotor and stator.

### 5.1.4 Isentropic Efficiency of Tail BLI Fan in Uniform Flow

To set the design efficiency for the tail BLI fan (the stage efficiency without BLI), we set, as mentioned in Section 5.1.2, the isentropic efficiency of 93% at an FPR of 1.35, as a reference. The relation between fan isentropic efficiency, $\eta_{fan}$, and polytropic efficiency, $\eta_{poly}$, is

$$\eta_{fan} = \frac{\pi^{\frac{\gamma-1}{\gamma}} - 1}{\pi^{\frac{\gamma-1}{\gamma\eta_{poly}}} - 1}. \tag{5.6}$$

The tail BLI fan polytropic efficiency is thus 93.3%, and the BLI fan isentropic efficiency is 92.9% at an FPR of 1.50 in uniform flow.

### 5.1.5 Split of Rotor and Stator Losses Based on Reaction

The fan stage reaction characterizes the asymmetry between rotor and stator loading and velocity triangles [2]. We applied the concept to different streamlines entering at different radial locations, to characterize the loss distribution between rotor and stator. Figure 5-5 shows the radial variation in reaction for the optimized rotor and stator body-force camber surfaces at design. The abscissa is the reaction and the ordinate is the span ratio (radial location normalized by the tip radius).

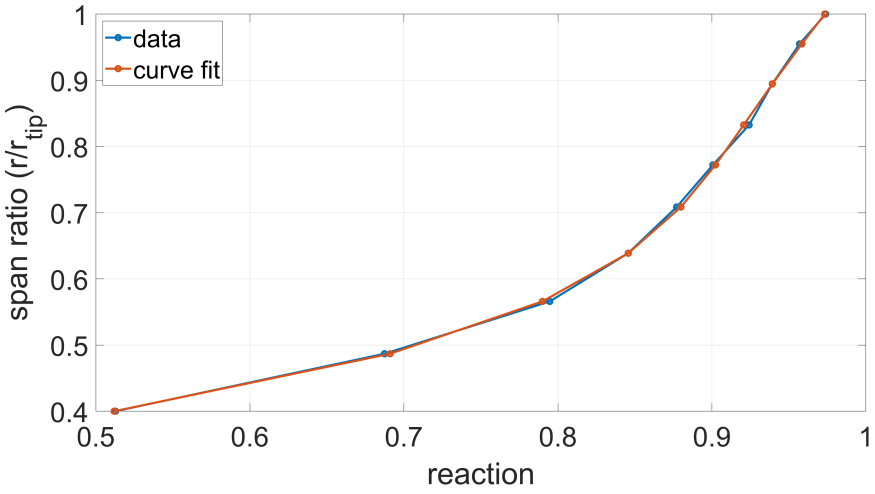



Figure 5-5: Distribution of reaction along the rotor span.

A quartic[5] curve fit was applied for establishing an empirical relation between the reaction $R_t$ and the span ratio $s_r$,

$$R_t = -4.5613 s_r^4 + 16.661 s_r^3 - 22.656 s_r^2 + 13.903 s_r - 2.3741, \tag{5.7}$$

where $s_r$ ranges from 0.4 to 1. Equation 5.7 was applied to Equation 4.6 (loss de-

[5]It can yields a fit within 1% of the data.

scription) to set the dependence of the coefficient $K_p$ on the rotor span ratio $s_r$,

$$\begin{aligned} K_{p,rotor} = c_D[&K_{\delta 1}\delta + K_{\delta 2}\delta^2 + K_{\delta 3}\delta^3 + K_{\delta 4}\delta^4 \\ &+ K_{p0}(-2.3741 + 13.903 s_r - 22.656 s_r^2 + 16.661 s_r^3 - 4.5613 s_r^4)]. \end{aligned} \tag{5.8}$$

### 5.1.6 Effect of Loss Buckets on Tail BLI Efficiency Penalty

For a fan in uniform flow, the aerodynamic design operating point is typically at or near peak efficiency. For a tail BLI fan, however, the rotor inlet incidence angle variation causes a penalty on the stage isentropic efficiency, and thus efficiency drop varies with different types of rotor loss buckets.

Figure 5-6 shows two rotor loss buckets for the same tail BLI operating point: FPR$= 1.50, M_x = 0.60$, installed efficiency $\eta = 87.8\%$ and with the same stator loss bucket. The abscissa is the rotor mid span incidence angle and the ordinate is the loss coefficient $\omega$. The incidence angle $\delta_0$ represents the design point for uniform flow[6]. About 70% of the fan loss occurs in the rotor. For the fan with a wider low loss region in the rotor, the efficiency penalty is 5.1%, compared to the design condition in uniform flow. For the fan with a narrower low loss region, the efficiency penalty is 7.4%, even though the design point loss is half that of the fan with the wider low loss region.

Figures 5-7 and 5-8 show the incidence angle variations due to BLI. The maximum incidence is 9° at the bottom of the flow annulus and the minimum is $-3°$ around $\theta = 120°$ close to the inner contour of the annulus. At the rotor leading edge, mid span, the incidence angle swings roughly 7° around the circumference, with an average of 5°, which is at the minimum loss point of the rotor loss bucket. The maximum incidence is located at the bottom, because the boundary layer has the lowest velocity at the bottom and the rotor linear velocity is the highest at the tip, leading to the largest relative flow angle.

The two fans that are shown in Figure 5-6 have the same installed efficiency of 87.8%. The one on the left, however, has a design efficiency of 92.9% in uniform flow

[6]For a fan with BLI, the rotor mid-span incidence swing is marked at the bottom of Figure 5-6.

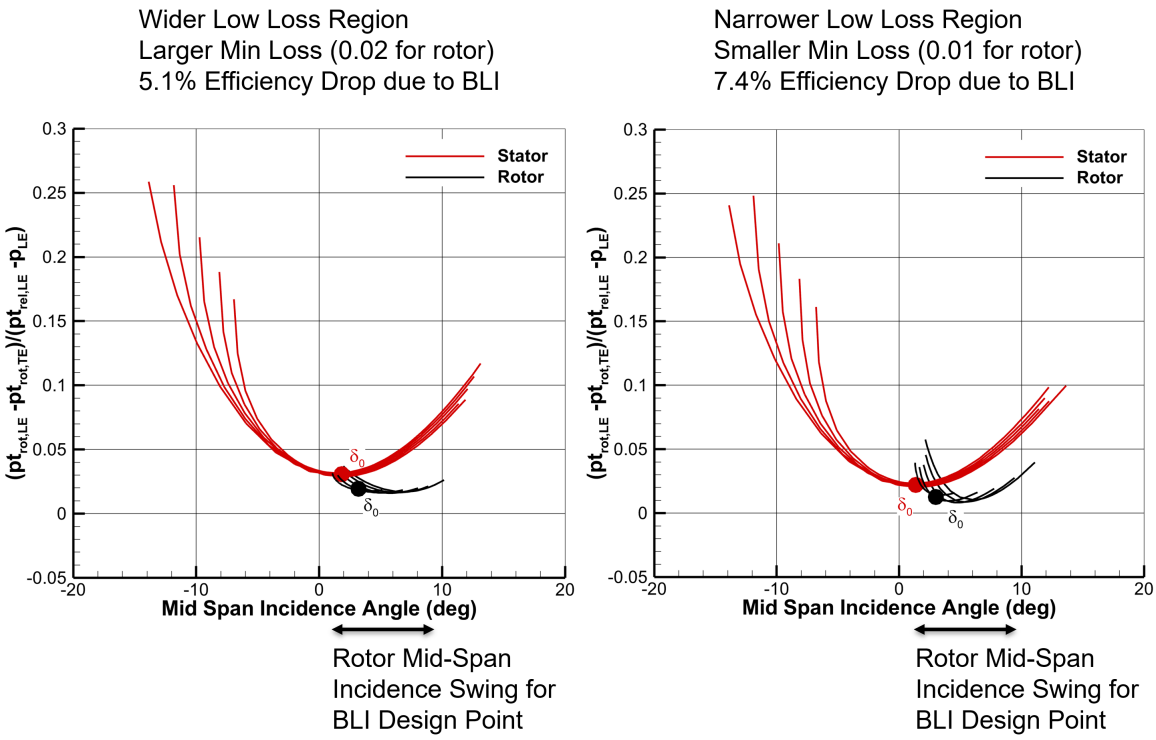



Figure 5-6: Efficiency penalties for different fan loss buckets. A fan with a wider low loss region is preferred for the tail BLI. Compared to the design condition, there is a 5.1% efficiency decrease for the fan on the left, and a 7.4% decrease, for the fan on the right.

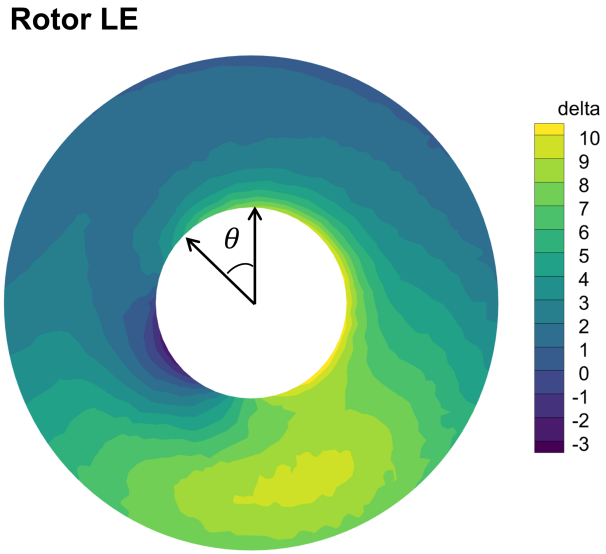



Figure 5-7: Rotor inlet incidence angle variation due to boundary layer ingestion. This incidence swing between $-3°$ and $9°$ is the cause of isentropic efficiency decrease for the tail BLI fan.

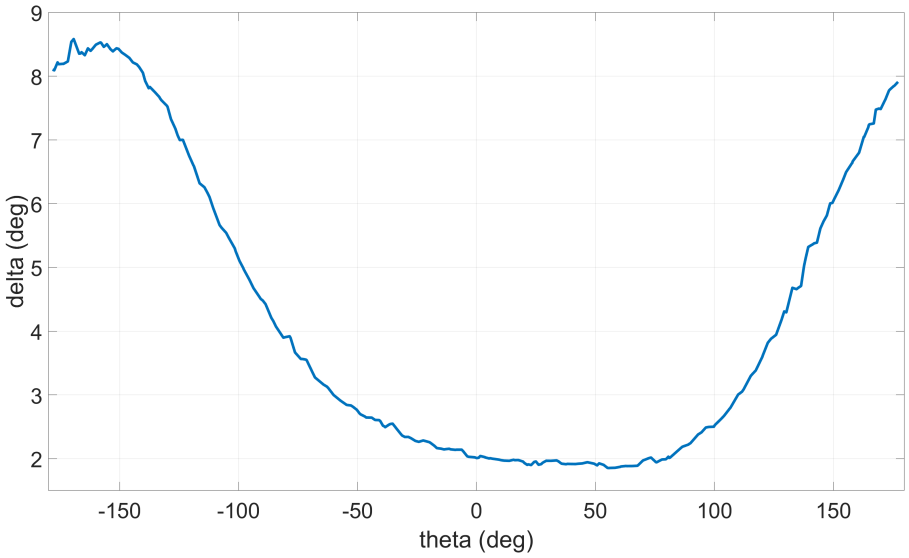



Figure 5-8: Circumferential distribution of rotor inlet incidence at mid span. $\theta = 0°$ corresponds to the top of the flow annulus and counter-clockwise is the positive direction. The incidence angle swings between 2° and 8.5° with an average about 5°.

while the one on the right has an efficiency of 95.2% at design, in order to achieve this same tail BLI installed efficiency. The latter value is optimistic and the installed efficiency should probably be lower than 87.8%. We have used the fan on the left to give the behavior for the tail BLI fan.

The calculations imply that a tail BLI fan should be designed with a wide low loss region in the rotor loss bucket, in order to mitigate the fan efficiency penalty due to inlet distortion[7].

The $K_p$ functions for the rotor and stator loss buckets on the left in Figure 5-6 are defined as

$$K_{p,rotor} = c_D[-125.66\delta + 493.48\delta^2 - 1550.3\delta^3 + 43834\delta^4 + 10.500(-2.3741 + 13.903s_r - 22.656s_r^2 + 16.661s_r^3 - 4.5613s_r^4)], \quad (5.9)$$

$$K_{p,stator} = c_D(3.3000 + 157.08\delta + 3947.8\delta^2). \quad (5.10)$$

The dissipation coefficient, $c_D$, is set as 0.0024.

[7]The efficiency drop of 5.1% for our tail BLI fan compared with uniform flow is within the published information range.

### 5.1.7 Fan Map and Efficiency Curves in Uniform Flow and with BLI

Figure 5-9 shows the uniform flow fan map and efficiency curves of the tail BLI fan with the wider low loss region. The design point, denoted by $\delta_0$, has FPR= 1.50, $M_x = 0.60, \eta = 92.9\%$, and it is set in the middle of the fan map to ensure stall and choke margins.

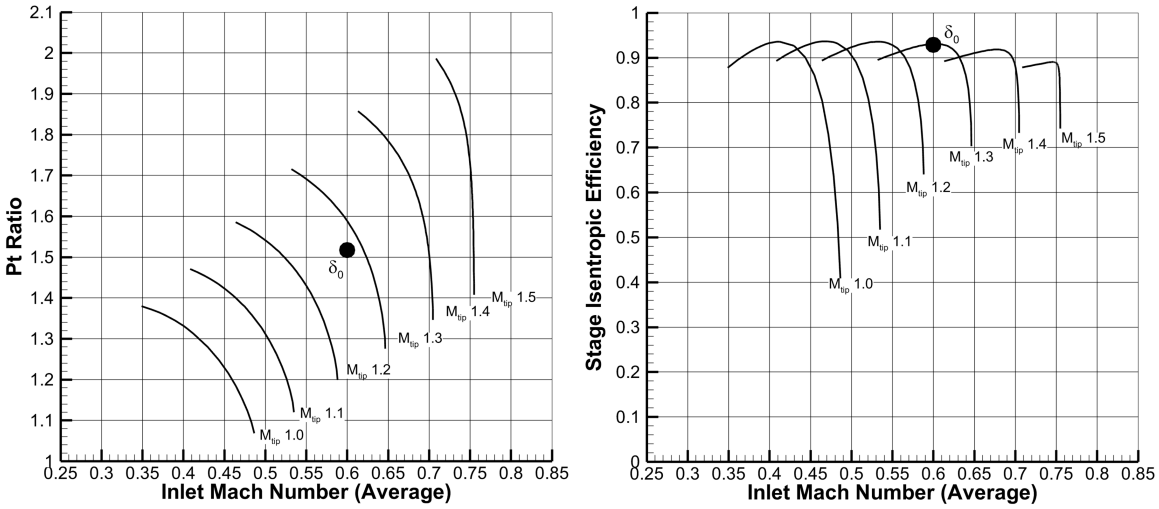



Figure 5-9: Fan map and efficiency curves of the tail BLI fan in uniform flow. The design point $\delta_0$ is set in the middle of the fan map to ensure stall and choke margins.

Figure 5-10 shows the corresponding fan map and efficiency curves for the fan with BLI. The design point, $\delta_0$, has FPR= 1.50, $M_x = 0.60$, but the efficiency is $\eta = 87.8\%$. There is an efficiency penalty of 5.1% compared with uniform flow, due to BLI.

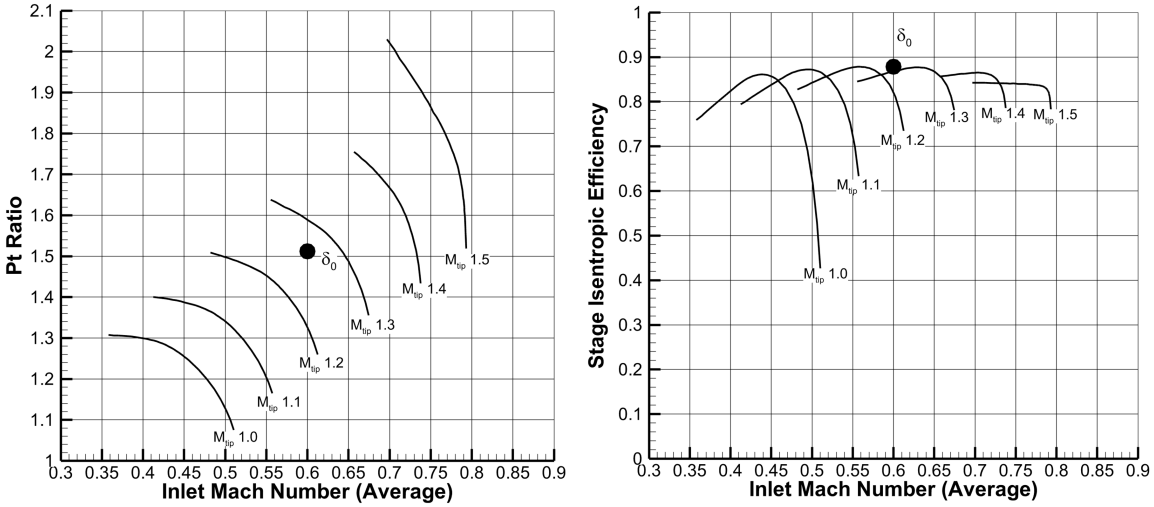



Figure 5-10: Fan map and efficiency curves of the installed tail BLI fan. The design point $\delta_0$ has an efficiency $\eta = 87.8\%$, so there is an efficiency penalty of 5.1% compared with uniform flow, due to BLI.

## 5.2 Effect of Non-Axisymmetric Stators

One potential way to reduce the rotor inlet incidence variation due to tail BLI is through the upstream influence of non-axisymmetric stators. Hall et al. [18] showed that for 2D flow stator exit flow angle perturbations 180 degrees out of phase with the rotor inlet incidence variation, which created non-uniform static pressure perturbations that were 90 degrees out of phase with the rotor incidence variation, were most effective in modifying the flow at the rotor inlet. For 3D flow, the most effective out-of-phase angle may depend on the specific boundary layer profile and fan operating conditions. Further, since the static pressure perturbation is not felt upstream in supersonic flow, the effectiveness of non-axisymmetric stators will also depend on the relative flow Mach number.

To examine this idea, the non-axisymmetric stators were modeled by rotating the body-force vectors about the local radial coordinates shown in Figure 4-1. The rotation angle $\xi$ is defined by parameters $a_0$ and $\theta_0$ for circumferential locations $\theta$:

$$\xi = \frac{a_0}{2}[1 - \cos(\theta + \theta_0)]. \tag{5.11}$$

The optimized non-axisymmetric stators created exit flow angle perturbations, approximately 100° out of phase with rotor incidence variances, as in Figure 5-11.

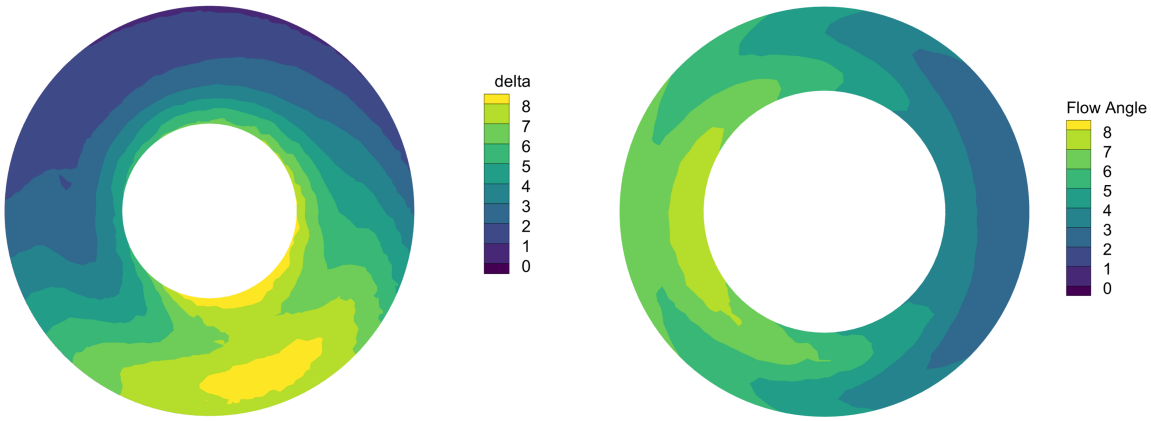
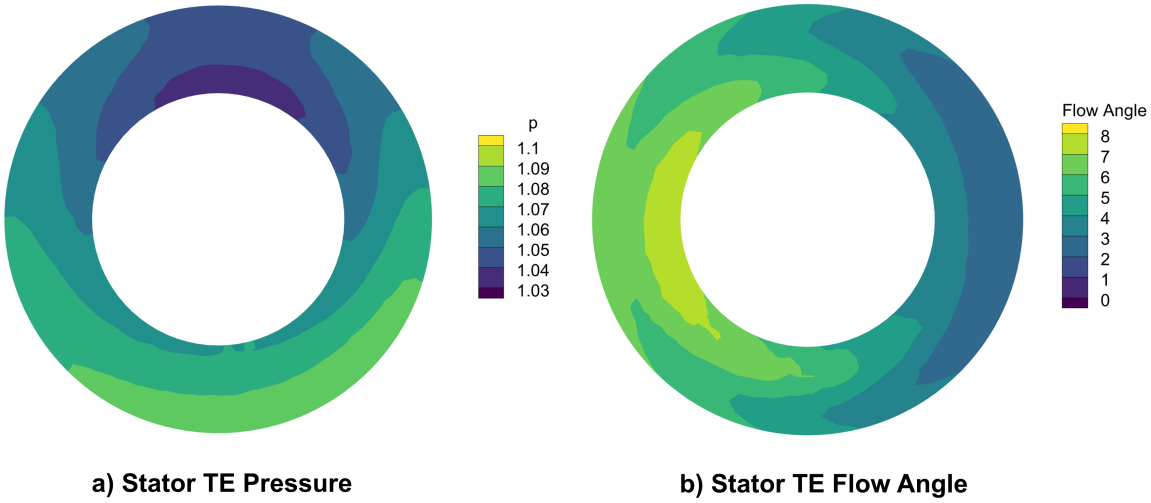



Figure 5-11: The optimized non-axisymmetric stator has TE flow angle perturbations about 100° out of phase with rotor LE incidence variation (angles in degrees).

Figure 5-12 shows that the static pressure perturbation at the stator trailing edge is 90° out of phase with the flow angle non-uniformity, consistent with the Cauchy-Riemann relation between static pressure perturbations and flow angle perturbations. The change in rotor incidence distortion, however, was small, as in Figure 5-13; the optimized non-axisymmetric stators reduced the shaft power by 0.8% at tail BLI design[8].

[8]This corresponds to 0.3% total fuel burn reduction of the tail BLI aircraft.




**a) Stator TE Pressure** **b) Stator TE Flow Angle**

Figure 5-12: Stator TE pressure perturbations 90° out of phase with flow angle perturbations (static pressure normalized by freestream stagnation pressure; flow angles in degrees). This out-of-phase angle is consistent with the Cauchy-Riemann relation between static pressure perturbations and flow angle perturbations.

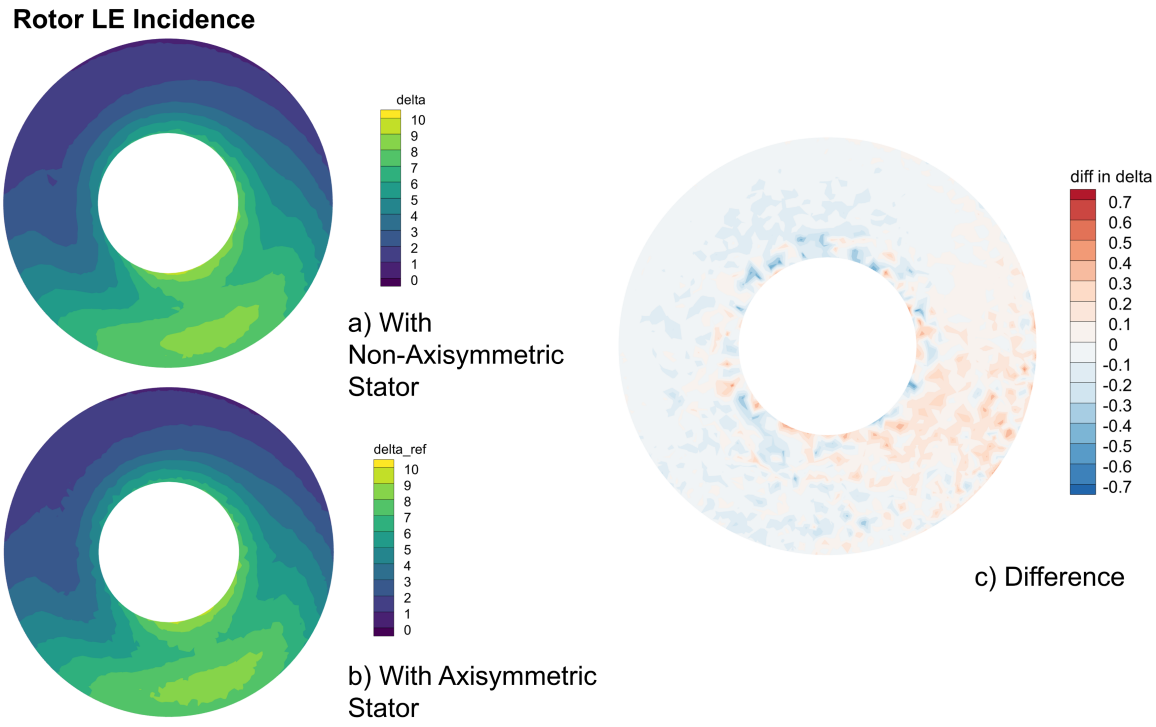



Figure 5-13: Limited influence of non-axisymmetric stator on rotor incidence variation (angles in degrees).

The main reason for the low effectiveness of the non-axisymmetric stators here is the supersonic rotor relative flow. The tip Mach number of the rotor is 1.26, and the

majority of the relative flow is supersonic, as in Figure 5-14, and the upstream effect of the static pressure field is thus limited.

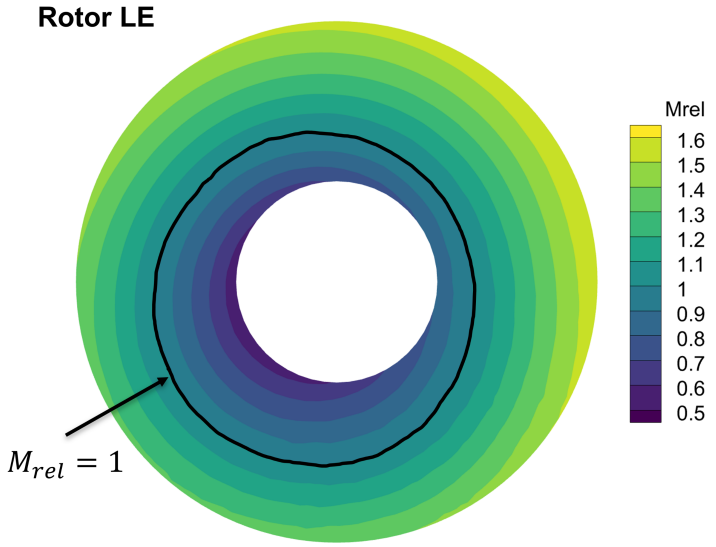



Figure 5-14: Majority of rotor relative flow is supersonic at the rotor leading edge. This causes the the stator pressure field upstream influence to be limited on the rotor incidence variation.

# Chapter 6

# Design Guidelines for Integrated Propulsors

## 6.1 Tail Design and Propulsor Configuration

### 6.1.1 Tail Design

The axisymmetric tail of proposed conceptual aircraft with multiple tail BLI propulsors is illustrated in Figure 6-1. Upstream of the propulsors there is a transition from the constant-radius fuselage to the propulsor inlet. The left hand side of Figure 6-2 shows various tube-and-wing airframe profiles from TASOPT for different tail contraction $R_{tail} = R_{fuse}(1-\xi^{b_{tail}}), \xi = \frac{\Delta x}{L_{tail}}, 0 \leq \Delta x \leq L_{tail}$, all having the same location for the end of constant-radius fuselage. The corresponding boundary layer edge Mach number distributions also from TASOPT, at various axial locations $x$ measured from the aircraft nose, at the cruise condition (freestream Mach number 0.8) are shown on the right hand side. The dimensions are normalized by the fuselage length. In this thesis, we intend to place the tail BLI propulsors around 90% of fuselage length, where the boundary layer edge Mach number $M_e$ is approximately 0.7 for a range of tail shapes.

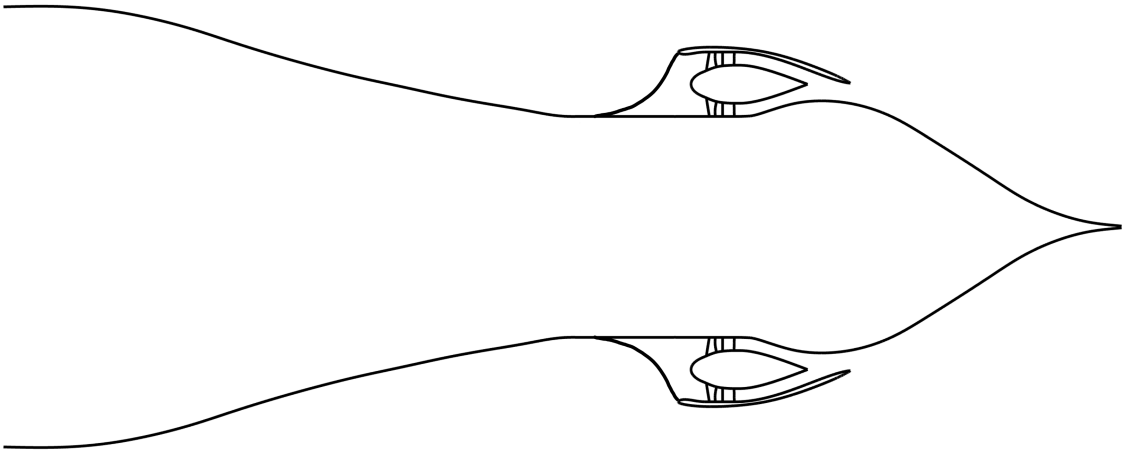


Figure 6-1: Centerline: axisymmetric tail with top and bottom BLI propulsors.

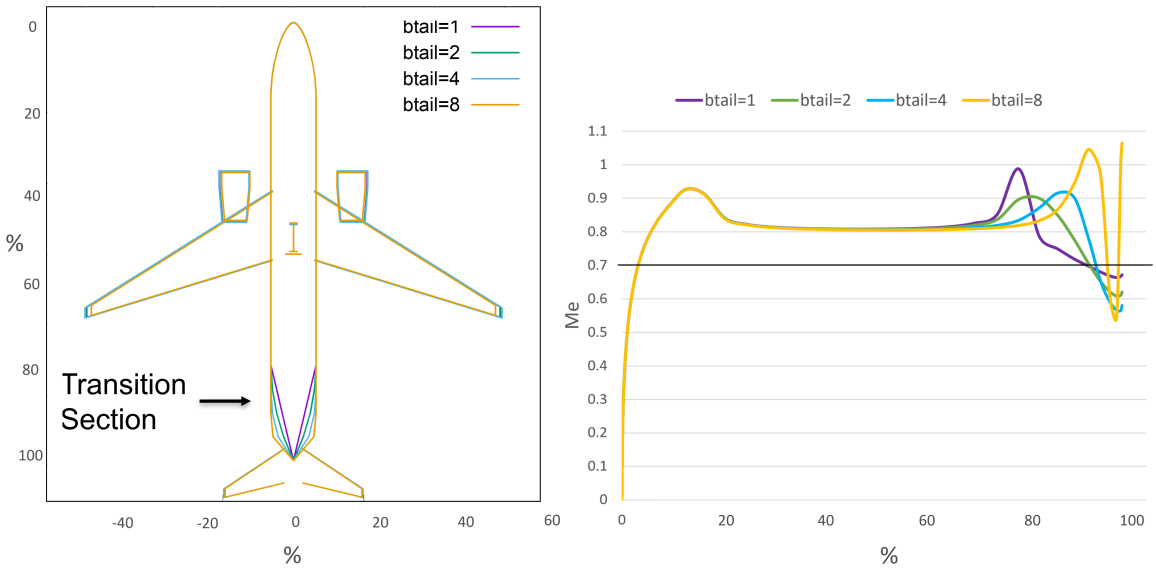



Figure 6-2: Left hand side shows various tube-and-wing airframe profiles. btail refers to the transition from the constant-radius fuselage. Right hand side shows TASOPT based boundary layer edge Mach number at different axial locations for various tail profiles. At 90% of fuselage length, the boundary layer edge Mach number $M_e$ is approximately 0.7 for a range of tail shapes.

The tail profile should be designed for no flow separation between the end of constant-radius fuselage and BLI propulsors, as well as for a boundary layer edge Mach number of 0.7 at the propulsor inlets[1]. The designed tail profile is shown in Figure 6-3 which has the "actual" dimensions included. No separation was seen

[1]We want this boundary layer edge Mach number to match the TASOPT analysis.

upstream of the tail BLI propulsor as indicated in Figure 6-4, which shows a side view of the tail streamlines and BLI propulsor. An analysis of the ingested mechanical power is given in Appendix A.

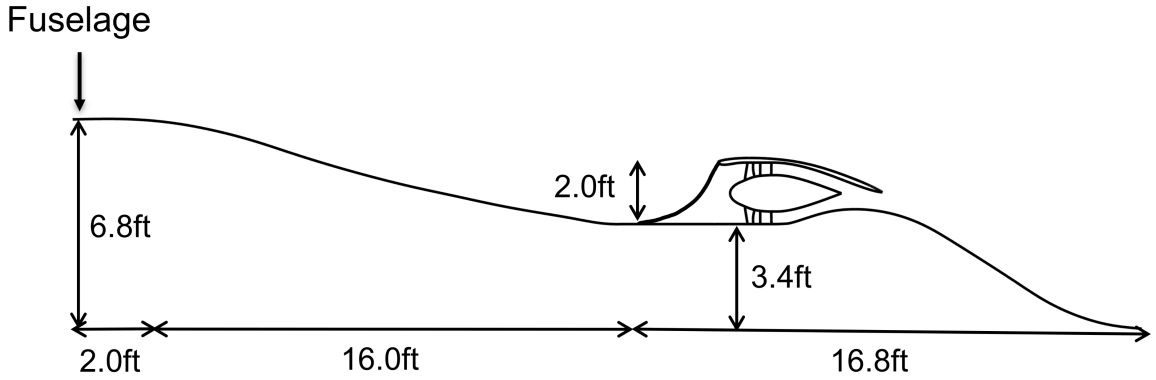



Figure 6-3: Centerline view of the tail and integrated propulsor with dimensions.

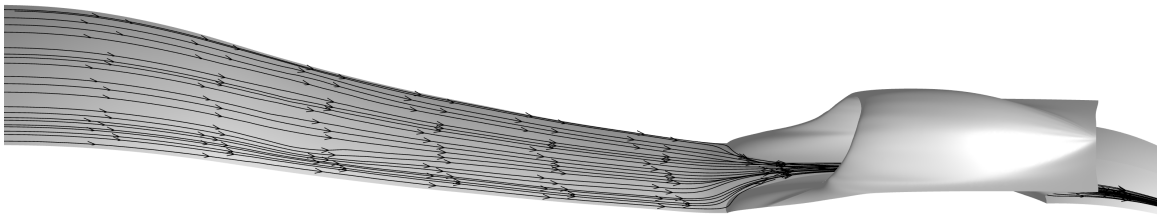


Figure 6-4: No separation upstream of tail BLI propulsors. This meets the design requirement of the tail transition upstream of the tail BLI propulsors.

### 6.1.2 Propulsor Configuration

The number of tail-integrated propulsors is determined by the desired amount of ingested boundary layer. Greater boundary layer ingestion by a propulsor implies more ingested mechanical power, which is beneficial for improving the propulsive efficiency. To do this, however, we require a larger propulsor inlet, which results in larger weight, more nacelle drag and thus higher cruise propulsive power.

The number of integrated propulsors was chosen to be nine. The principle was to make the propulsor inlet diameter approximately the same as the local boundary layer thickness[2]. Figure 6-5 is an isometric view of the BLI propulsors on the axisymmetric

[2]The local boundary layer thickness at the propulsor inlet depends on the tail profile. The number

tail (eight of nine propulsors can be seen). Figure 6-6 shows contours of the axial Mach number at propulsor centerline and the boundary layer edge streamline. It can be seen that the boundary layer edge streamline coming from the end of constant-radius fuselage enters the propulsor inlet at the top, with the local edge Mach number approximately 0.7. The propulsors thus ingest about 70% of the boundary layer[3]. We note that this configuration may not be optimal and a sensitivity study of tail BLI benefit versus number of integrated propulsors is planned for future work. As mentioned, however, flow behaviors and underlying mechanism do not depend on a specific configuration, and learnings from the current design are well applicable to other propulsor configurations.

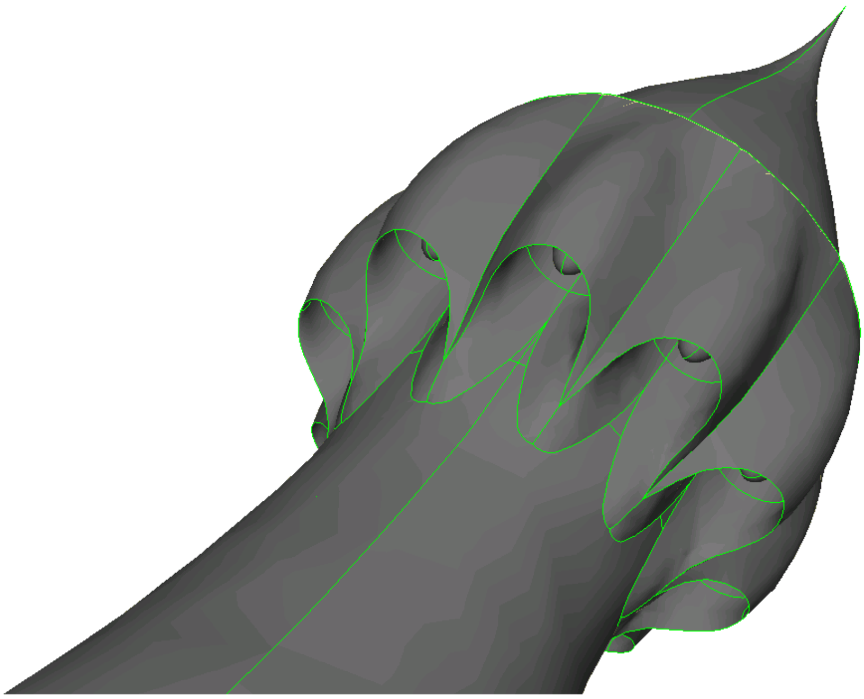


Figure 6-5: Isometric view of tail BLI propulsors looking downstream.

of propulsors is thus specific to the tail design.

[3]70% ingestion is in terms of mass flow.

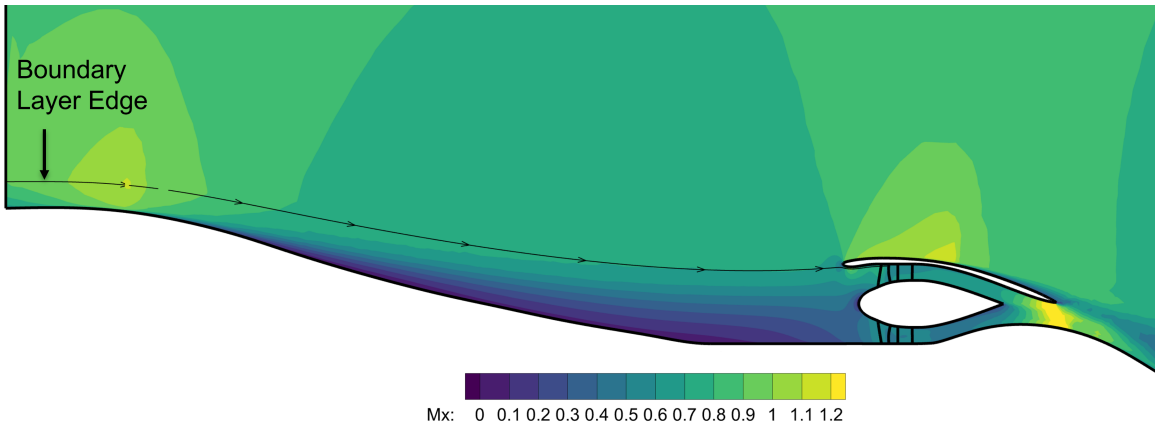



Figure 6-6: Contours of axial Mach number at centerline for tail-integrated propulsor. The boundary layer edge streamline coming from the end of constant-radius fuselage enters the propulsor inlet at the top, with the local edge Mach number approximately 0.7. This tail design achieved the desired boundary layer edge Mach number at the propulsor inlet.

## 6.2 Computational Domain

Because the propulsors are taken as the same around the tail, the computation domain for each of the tail-integrated propulsors is wedge-shaped. The domain is shown in Figure 6-7, which is $1/N_{prop}$ of the domain for the full configurations ($N_{prop} = 9$ in this design).

The wedge side boundaries are inviscid symmetry walls, which simulate the presence of adjacent tail BLI propulsors. The outflow boundary condition is freestream static pressure, and the outflow is placed at a distance far enough from the nozzle exit to avoid interference with the flow field surrounding the integrated propulsor. A 2D Coles profile boundary layer model is used to impose the boundary condition at the inflow of the computational domain (left hand side of Figure 6-7). The boundary layer parameters, $Re_\delta = 1.24 \times 10^6$ and $C_f = 0.001804$, for the Coles profile are obtained from TASOPT analysis for the baseline aircraft at cruise. The boundary layer profiles thus produced are similar to those extracted from 3D CFD simulations of a full aircraft[4] as in Appendix D.

[4]3D RANS CFD results of the baseline aircraft are provided by MHI.

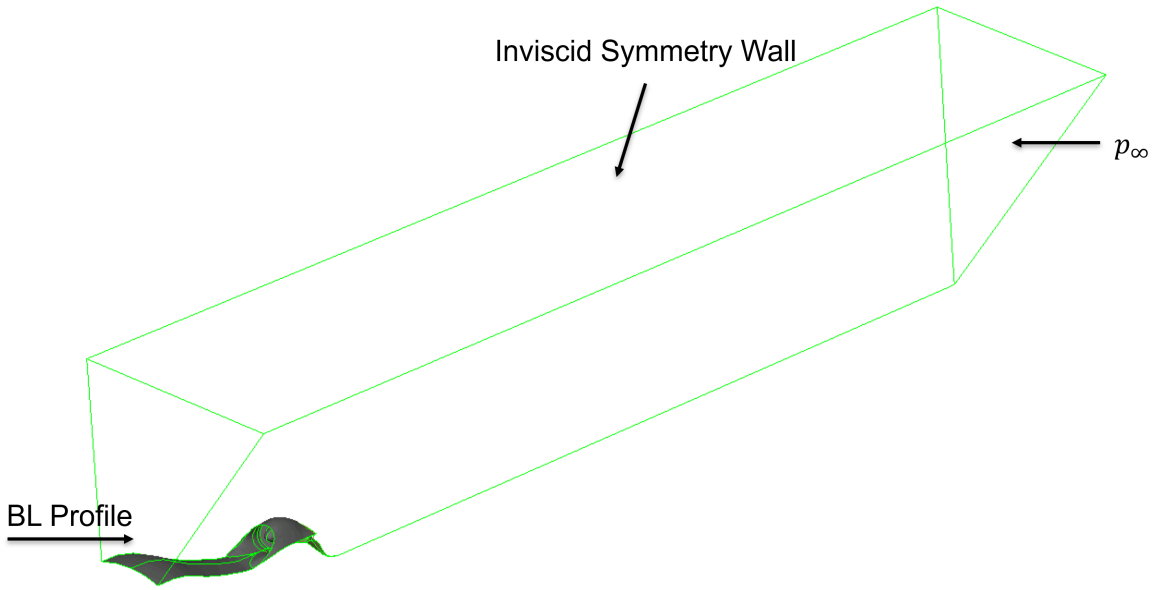



Figure 6-7: Computational domain for tail-integrated propulsor. This wedge-shaped domain and boundary conditions enable the CFD to be carried out in reduced computation cost, with flow conditions consistent with the full configuration.

## 6.3 Inlet Design for BLI

### 6.3.1 Design Features and Guidelines

The aerodynamic requirements for the tail BLI propulsor inlet are:

- **Reverse-flow-free at the inlet**: To achieve a smooth transition between the tail and inlet, without reserve flow entering the propulsors, the propulsor inlet should include an upstream extension. The inlet area is determined based on the highest inlet boundary layer edge Mach number[5], which occurs at cruise; with fixed turbomachinery, higher boundary layer edge Mach numbers is more likely to result in choked fan flow, for a fixed rotational speed, which needs to be avoid by the inlet area schedule.

- **Shock-free at the inlet lip**: Reducing the curvature of the inlet lip is effective in alleviating the local overspeed [25]. The streamline curvature below the inlet lip gives rise to local flow acceleration, as illustrated in Figure 6-8; excessive

[5]The largest amount of mass flow which may be ingested by the propulsor, can be estimated based on the fan face Mach number near choked, for a specific speed line.

acceleration can result in shock waves and losses. Overspeed around the inlet lip is more likely to occur as the freestream Mach number increases.

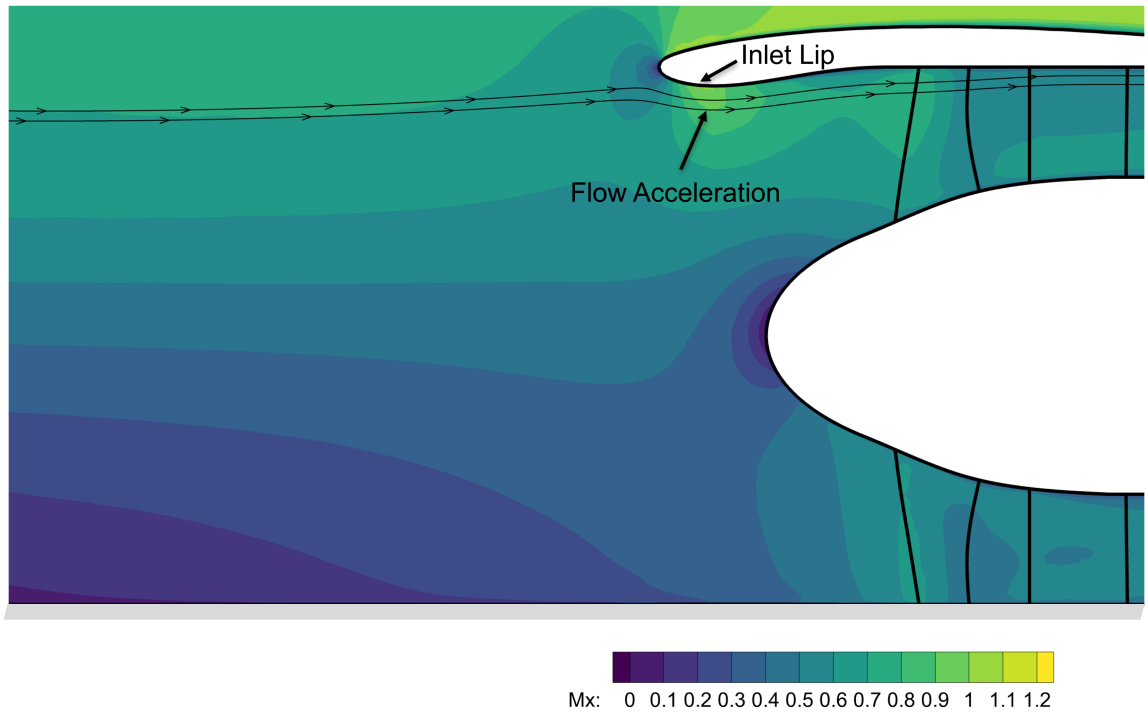



Figure 6-8: Streamline curvature below the inlet lip results in local flow acceleration. The curvature of the inlet lip should be controlled to achieve no shock at cruise.

### 6.3.2 Inlet Geometry and Flow Behavior

To complement the isometric view of the tail BLI propulsor inlet geometry in Figure 6-5, Figure 6-9 gives the centerline profile of the integrated propulsor, including the inlet lip and nacelle[6]. The inlet upstream extension formed by two adjacent propulors is effective for ensuring a smooth transition from tail to propulsor, and the absence of reverse flow is illustrated by Figure 6-10. In the vicinity of the propulsor inlet, the streamlines are attached to the surface and the axial Mach number is positive. The cross-section cut at the inlet throat shows that the local axial Mach number ranges from 0.3 to unity, and is reverse-flow-free and shock-free at the station. This inlet design meets the aerodynamic design requirements.

[6]Nacelle design will be covered in the next section.

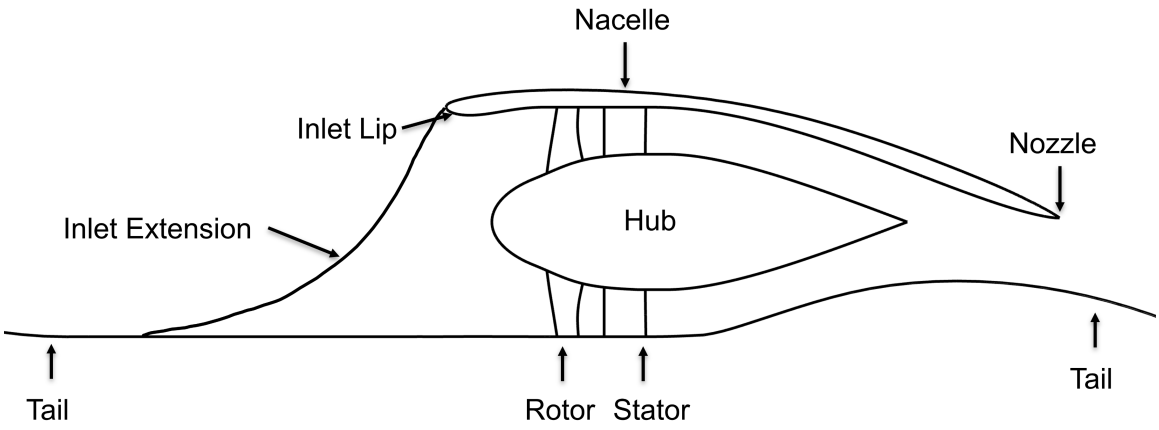



Figure 6-9: Sketch of centerline profile of the tail-integrated propulsor.

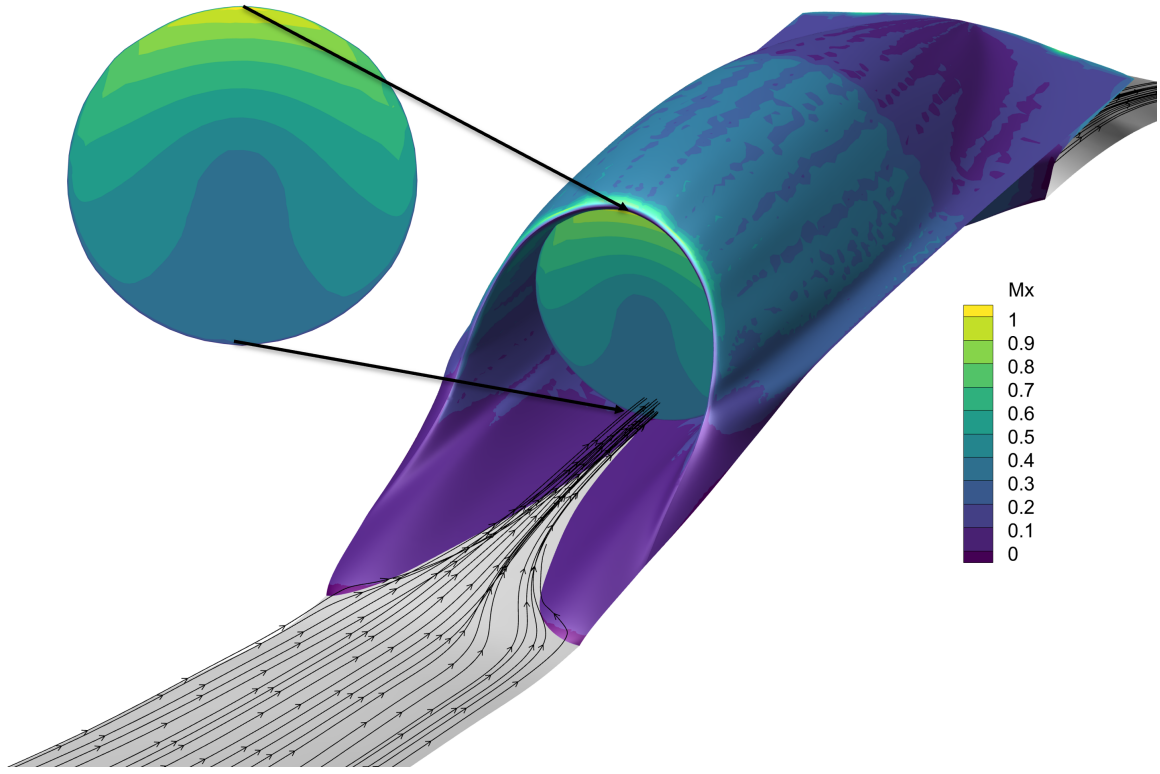



Figure 6-10: Calculations show no reverse flow and no shock in the vicinity of propulsor inlet. The cross-section cut at the inlet throat shows that the local axial Mach number ranges from 0.3 to unity, and is reverse-flow-free and shock-free at the station. This inlet design meets the design requirements.

## 6.4 Nacelle Design for BLI

### 6.4.1 Design Features and Guidelines

The tail BLI propulsor nacelle should have the following design features:

- **Low-loss on the nacelle surface**: To achieve this, we chose the nacelle outer contour to be similar to the profiles of supercritical airfoils to delay (or weaken) shock wave formation. This type of nacelle outer contour can turn the high-speed flow at cruise with stagnation pressure loss smaller than 1%.

- **Continuous acceleration of the internal flow from fan exit to nozzle**: The area of internal flow passage should be scheduled to monotonically decrease from fan exit to the nozzle. For conventional propulsors, the internal flow area is nearly axisymmetric and thus can be readily scheduled. For the integrated propulsor, however, the internal flow passage (i) is non-axisymmetric and (ii) also depends on the tail profile. Both effects need to be addressed in the nacelle design process.

### 6.4.2 Nacelle Geometry and Flow Behavior

Figure 6-11 is a contour plot of axial Mach number on the propulsor centerline. There is a weak shock on the aft nacelle outer contour, with axial Mach number of 1.15, and a maximum stagnation pressure drop across the shock of 0.5%.

In the internal flow passage, there is continuous flow acceleration from the fan stator trailing edge to the nozzle. Figure 6-12 shows the mass-averaged absolute Mach number of the internal flow, as a function of distance along the passage. The flow exits the fan stator at Mach 0.56 and continuously accelerates to Mach 1.1 at the nozzle. The flow is non-uniform at the annular nozzle exit, as in Figure 6-13. The highest Mach number is 1.3, at the top. The location of this highest Mach number is due to the curvature of the local nacelle profile, as in Figure 6-9. In regions closer to left and right sides of the nozzle, the flow Mach number is around unity, so the

overall mass-averaged Mach number is higher than unity at the annular nozzle exit.

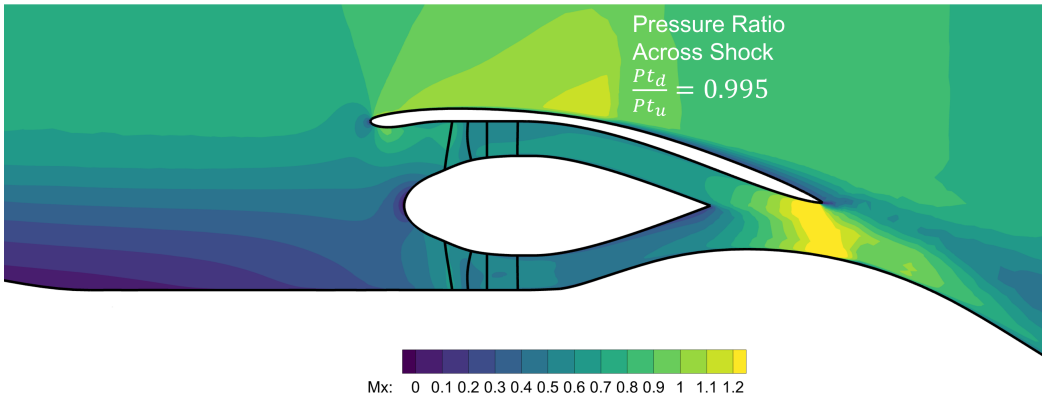



Figure 6-11: Centerline: weak shock on nacelle surface. The maximum stagnation pressure drop across the shock is 0.5%. The nacelle outer contour similar to the profiles of supercritical airfoils achieves low-loss operation on the nacelle surface at cruise.

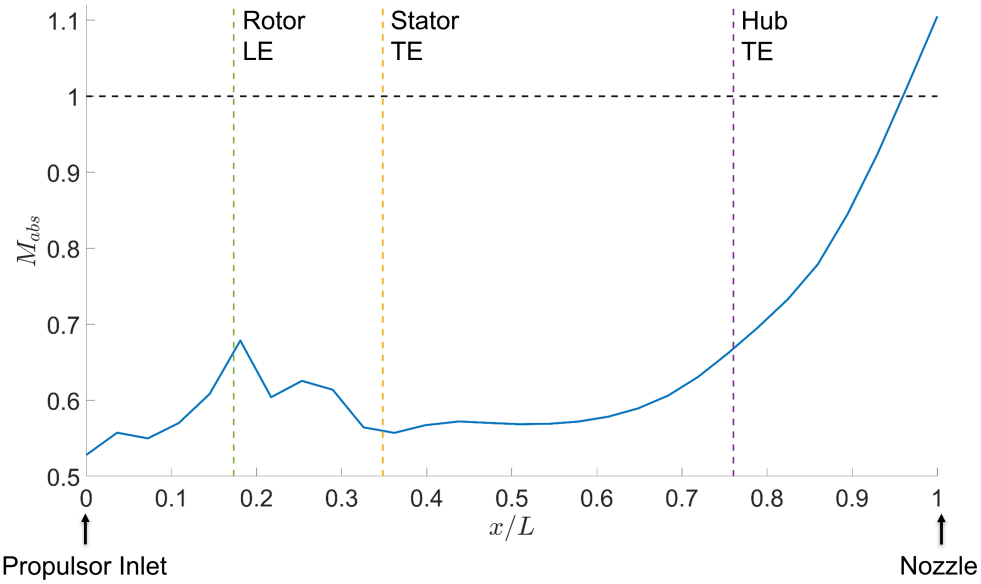



Figure 6-12: Internal flow passage absolute Mach number: acceleration achieved from stator TE to nozzle exit, with this non-axisymmetric nacelle design.

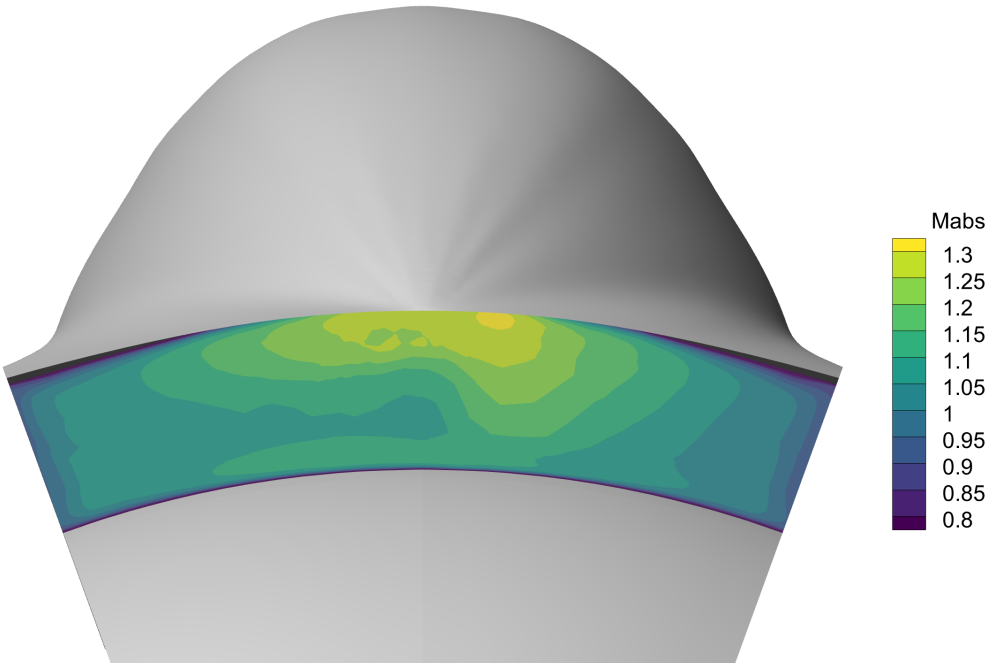



Figure 6-13: Non-uniform absolute Mach number at the annular nozzle exit. The highest Mach number is 1.3, at the top, due to the curvature of the local nacelle profile. In regions closer to left and right sides of the nozzle, the flow Mach number is around unity.

## 6.5 Nozzle Design

### 6.5.1 Design Features and Guidelines

There are two specific challenges in nozzle design for tail-integrated propulsors. First, a circular nozzle does not allow low-loss integration of BLI propulsors on the tail, because the area between the lower portion of nozzle surface and the tail exhibits flow separation beneath the nozzle [28]. Second, the nozzle exit area is smaller than the propulsor inlet area, so the flow passage between adjacent nacelles diverges as it approaches to the nozzle exit. In consequence, the flow between nacelles may experience excessive diffusion, and separate, from the nacelle surface as it moves towards the nozzle exit. Figure 6-14 highlights the area between a circular nozzle and the tail, as well as the diffusing channel between adjacent nacelles. These two regions are where flow separation may occur.

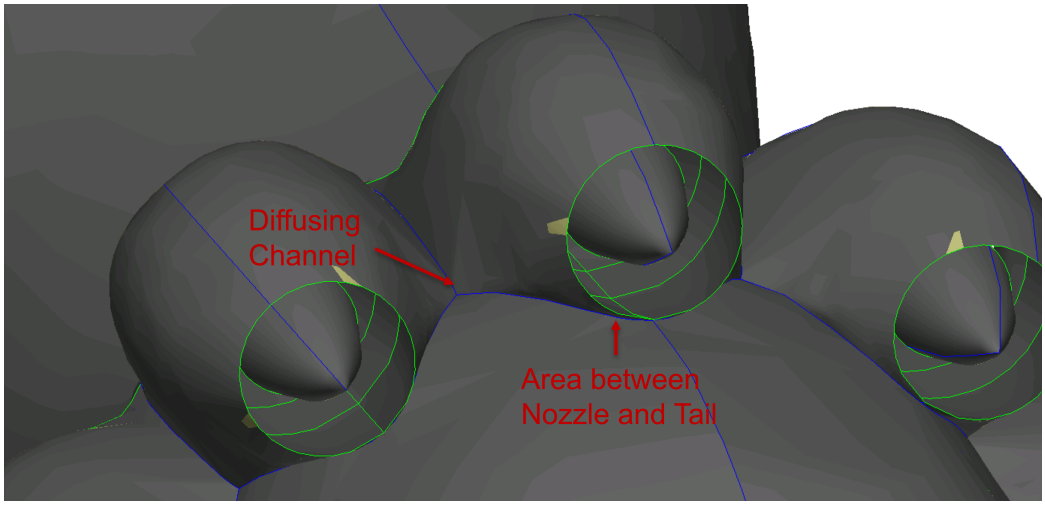



Figure 6-14: Geometry of integrated propulsors with circular nozzles.

An example of a circular nozzle with flow separation[7] is illustrated in Figure 6-15, in which there is substantial reverse flow near the nozzle exit. The circular nozzle results in an exit flow cross-section three times as large as the inlet flow cross-section, for the flow channel between nacelles. Figure 6-16 gives a top view of the situation, and the excessive diffusion.

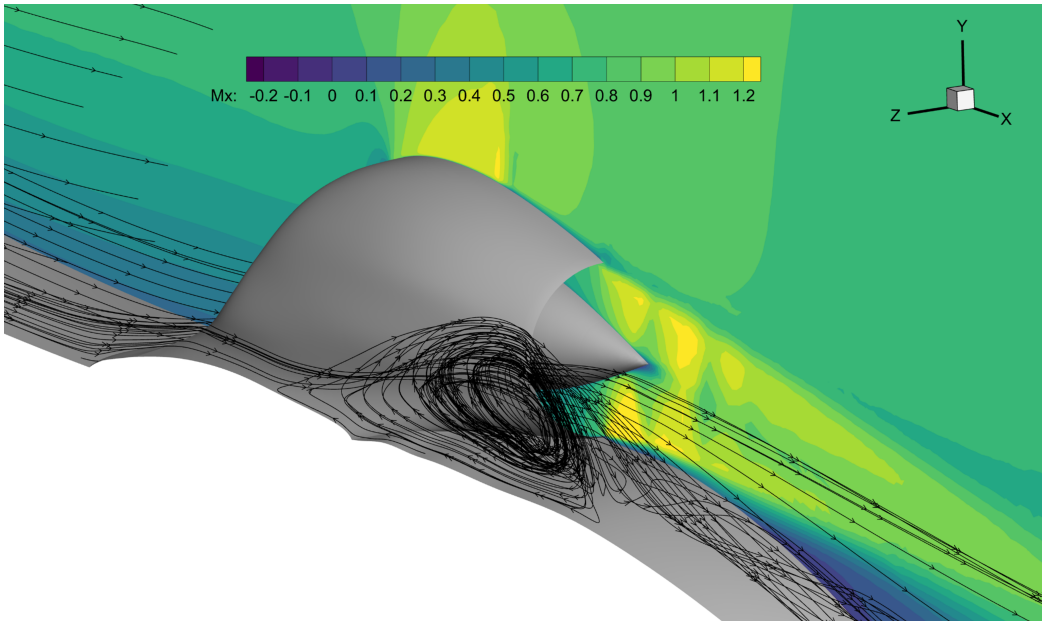



Figure 6-15: Reverse flow at the circular nozzle exit, due to excessive diffusion between adjacent propulsors.

[7]The several examples of unsatisfactory geometries to be shown are taken from the initial phases of our design exploration, in which the issues described had not yet been resolved.

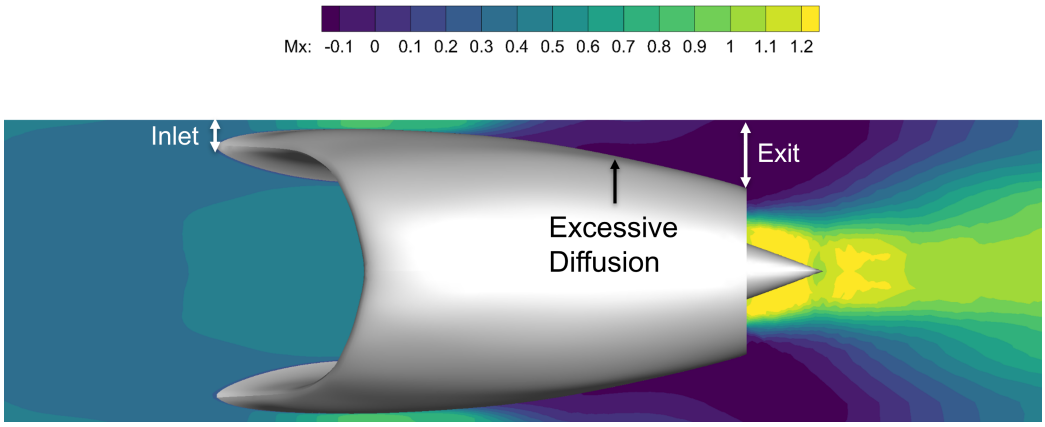



Figure 6-16: Top view of nacelles with circular nozzles. The ratio of the exit flow cross-section to the inlet flow cross-section is approximately 3, which results in excessive diffusion and thus flow separation.

A "good" nozzle design for tail-integrated BLI propulsors eliminates flow separation between nearby nacelles. In the design exploration, we were not able to fulfill the design requirements with separate-piece nozzle designs (circular nozzle, horseshoe nozzle, etc.). The learning was that an *annular nozzle* was an appropriate choice to eliminate flow separation between adjacent propulsors.

### 6.5.2 Annular Nozzle Design and Flow Behavior

Figures 6-17 and 6-18 give side and rear views of the annular nozzle, in which all nine tail-integrated propulsors share a common nozzle exit, with upstream walls separating the individual propulsors.

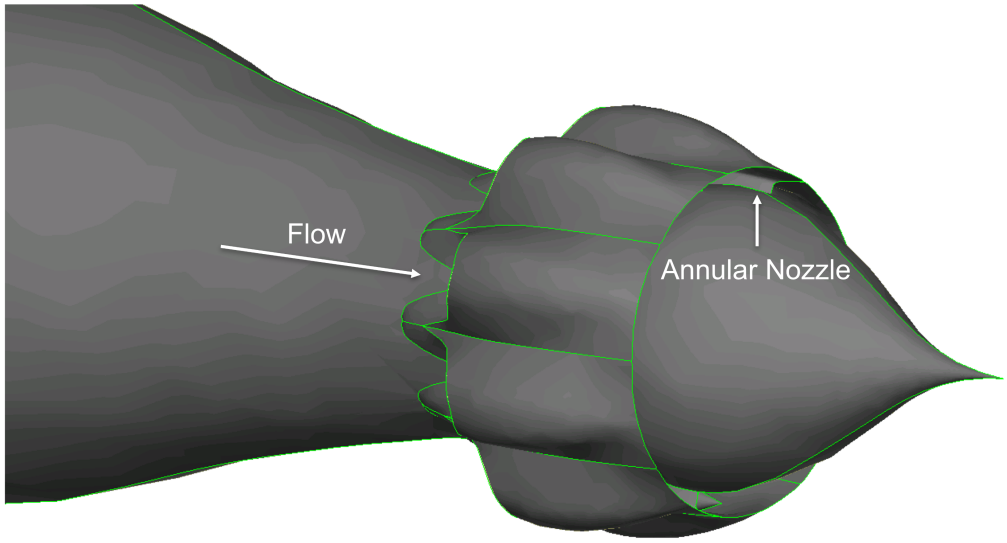



Figure 6-17: Side view of the annular nozzle.

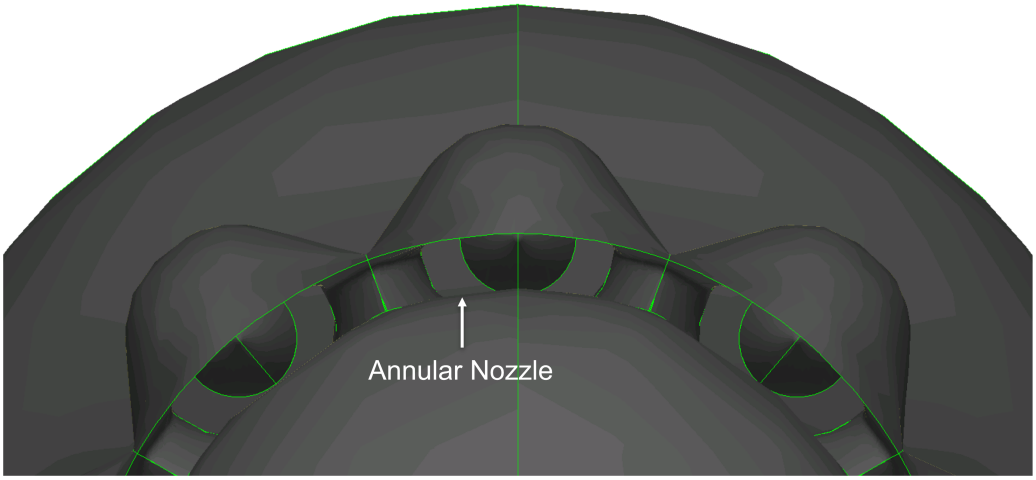



Figure 6-18: Rear view of the annular nozzle.

The flow separation between adjacent propulsors is eliminated, with an annular nozzle, as demonstrated by Figure 6-19. Further, there is no flow separation at the annular nozzle exit based on the axial Mach contours of Figure 6-20. The annular nozzle thus successfully achieves separation-free operation at cruise.

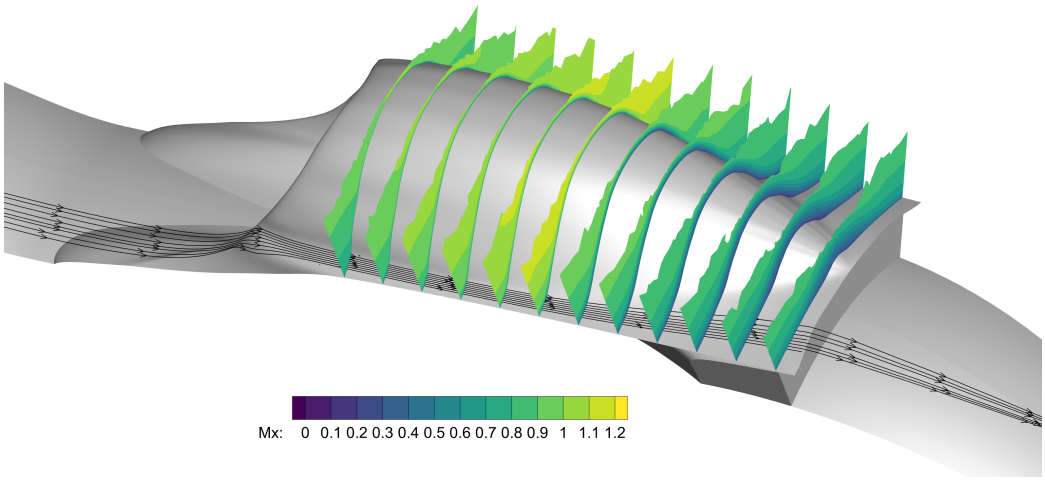



Figure 6-19: Mach number contour showing flow between adjacent nacelles. No flow separation is seen. Jagged edges of contour plots are due to finite mesh. This annular nozzle achieves flow-separation-free operation between nacelles at cruise.

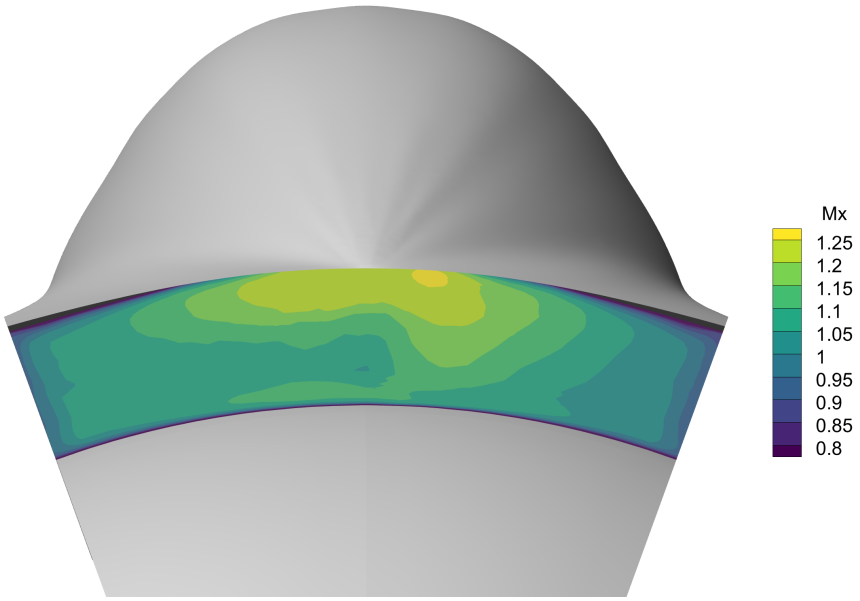



Figure 6-20: Non-uniform axial Mach number at the annular nozzle exit. No flow separation is seen. This annular nozzle achieves flow-separation-free operation at the nozzle exit at cruise.

With an annular nozzle, the ratio of exit flow cross-section to inlet flow cross-section is approximately 1.4, as in Figure 6-21. This area ratio is less than half of that for the flow channel between nacelles with circular nozzles. The flow diffusion in Figure 6-21 is much less than the diffusion in Figure 6-16, with the result that there

is no flow separation between nacelles with the annular nozzle.

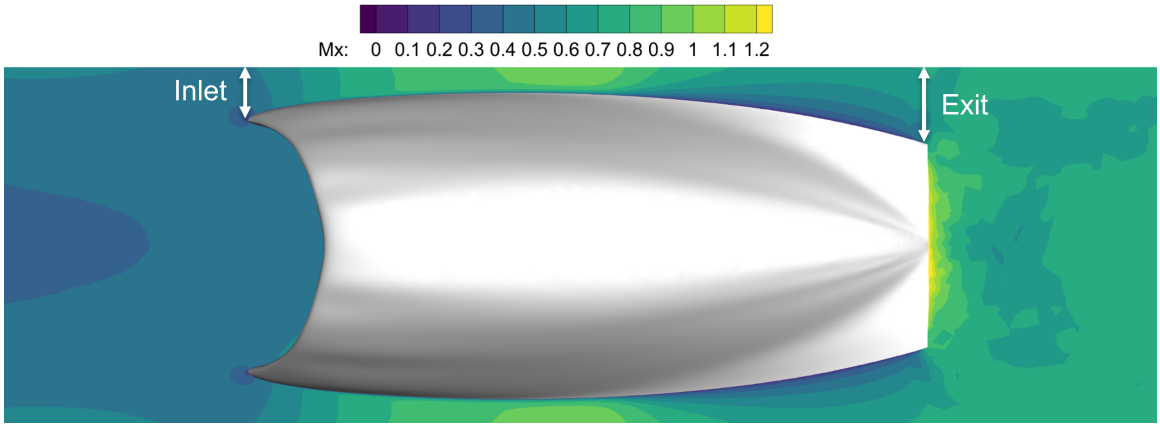



Figure 6-21: Top view of nacelle with the annular nozzle. The ratio of the exit flow cross-section to the inlet flow cross-section is approximately 1.4. This area ratio is less than half of that for the flow channel between nacelles with circular nozzles, leading to much less diffusion and no flow separation between adjacent nacelles.

Based on the design guidelines above, a successful integration of BLI propulsors on the axisymmetric tail was established[8], meeting all aerodynamic design requirements. This integrated geometry achieved low-loss operation at cruise and resolved all the flow issues observed in open literature or in the initial stage of design exploration. The highlight of this tail BLI propulsor design is the annular nozzle, enabling the appropriate flow channel area schedule between adjacent propulsors, to eliminate the flow separation due to excessive diffusion. This separation-free operation was not achieved by other nozzle designs in the open literature or in our initial design exploration. The key of the tail and inlet design is using an upstream inlet extension for a smooth transition between the tail and inlet, to eliminate flow separation. Further, controlling the curvature of the inlet lip is important for removing shock waves. For the nacelle design, a nacelle outer contour similar to the profiles of supercritical airfoils can delay or weaken shock formation. For a tail-mounted BLI propulsor, the internal flow passage is non-axisymmetric and depends on the tail profile. This requires the nacelle design to address these effects, in order to achieve continuous acceleration of the internal flow from fan exit to nozzle.

[8]More information about the geometry of tail and tail-integrated propulsors is in Appendix E.

# Chapter 7

# Tail-Integrated Propulsor Performance

In this chapter, we focus on the fan responses to tail BLI inlet distortion and the propulsor performance for the overall mission. We will first evaluate the fan responses to inlet distortion, in terms of stagnation pressure, static pressure, and axial Mach number. The benefit of tail BLI aircraft will then be determined in terms of shaft power, propulsive efficiency, and PFEI.

## 7.1 Fan Responses to Tail BLI Inlet Distortion

As discussed in Chapter 5, the tail BLI electric fan suffered a 5.1% drop in isentropic efficiency, compared with the design condition in uniform flow, due to rotor incidence variations, with about 70% of this loss occurring in the rotor.

The ratio of the fan face mass-averaged stagnation pressure to freestream ($p_{t,fan}/p_{t,\infty}$) is 83.6%. The stagnation pressure drop is 0.5% for the captured flow from propulsor inlet to fan face, due to viscous effects. Contours of stagnation pressure coefficient at various streamwise locations are illustrated in Figure 7-1. The stagnation pressure coefficient $C_{pt}$ is defined with respect to the freestream quantities as:

$$C_{pt} = \frac{p_t - p_{t,\infty}}{p_{t,\infty} - p_\infty}. \tag{7.1}$$

The boundary layer height is approximately equal to the propulsor inlet diameter. The tail BLI propulsors ingest about 70% of the total boundary layer coming from the freestream, and the rest of boundary layer passes between the propulsors.

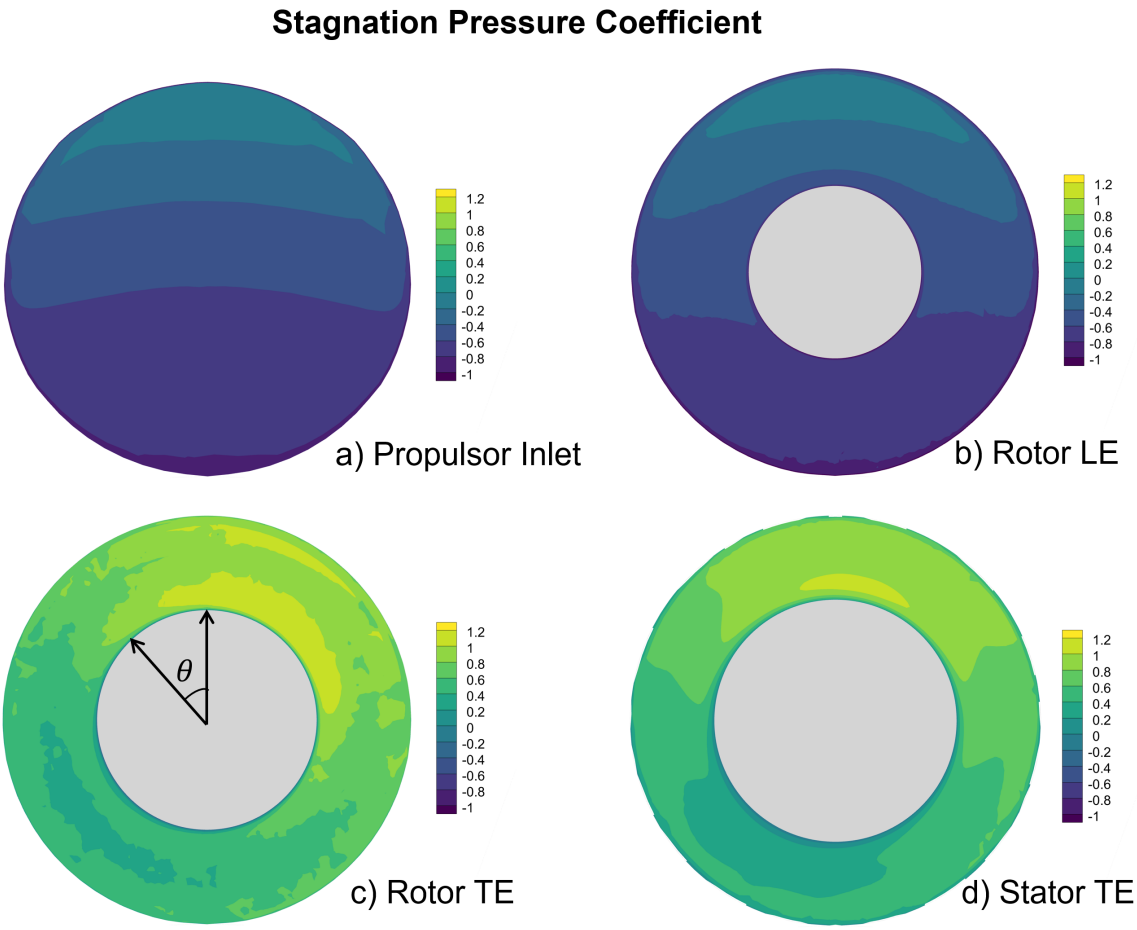



Figure 7-1: Stagnation pressure non-uniformity at station a), propulsor inlet (non-circular); station b), rotor LE; station c), rotor TE; station d), stator TE. The change in the stagnation pressure non-uniformity pattern across the stage is due to the non-uniform rotor loading caused by the incidence variation.

At the propulsor inlet, the stagnation pressure is stratified and is non-uniform in both radial and circumferential directions. The region of the maximum stagnation pressure is located at the top, between $-45°$ and $45°$ (top is $0°$ and counter-clockwise is the positive direction). This pattern persists, at least qualitatively, from propulsor inlet to rotor leading edge. At the rotor trailing edge, the stagnation pressure is no longer stratified, and the region of maximum stagnation pressure is located between $-90°$ and $0°$, with the region of minimum stagnation pressure between $90°$ and $180°$.

The circumferential location change of the maximum stagnation pressure is due to the rotor inlet incidence non-uniformity. As in Figure 5-7, the maximum incidence is located near 190° and it decreases from 190° to 0° and from 190° to 360° (i.e. top). The minimum is located at 120° close to the inner contour of the annulus. The incidence angle for circumferential locations between 180° to 360° is in general higher than that located at the same height from the bottom between 0° to 180°. A larger incidence means a larger force and thus more work on the flow. This rotor loading non-uniformity leads to the circumferential location change of maximum stagnation pressure in the clockwise direction, for the rotor trailing edge, compared with the rotor leading edge. At the stator trailing edge, the non-uniformity pattern is similar to that at the rotor trailing edge, because the stator does not do work on the flow. Due to the stagnation pressure drop[1] across the stator, the region of maximum stagnation pressure is smaller and the region of minimum stagnation pressure is larger than at the rotor trailing edge.

Figure 7-2 shows the axial Mach number at different stations. At the propulsor inlet, the pattern for axial Mach number is different from the pattern for stagnation pressure, because of the upstream static pressure field, and Figure 7-3 a) thus shows the static pressure[2] field at the propulsor inlet. The non-uniformity is mostly radial with a low pressure region at the top because of the high local Mach number[3]. The axial Mach number non-uniformity is attenuated across the fan stage, and the axial velocity at the stator trailing edge is almost uniform. This attenuation of the axial Mach number non-uniformity can be explained using the momentum equation. The lower-velocity flow has a smaller dynamic pressure than the higher-velocity flow, so the pressure gradient, which is favorable, has a larger impact on the lower-velocity flow and tends to attenuate the axial Mach number non-uniformity across the stage.

[1] About 30% of the total loss across the stage occurs in the stator.

[2] The static pressure coefficient is defined as $C_p = \frac{p - p_\infty}{p_{t,\infty} - p_\infty}$.

[3] This high Mach number is caused by the curvature of the local nacelle profile.

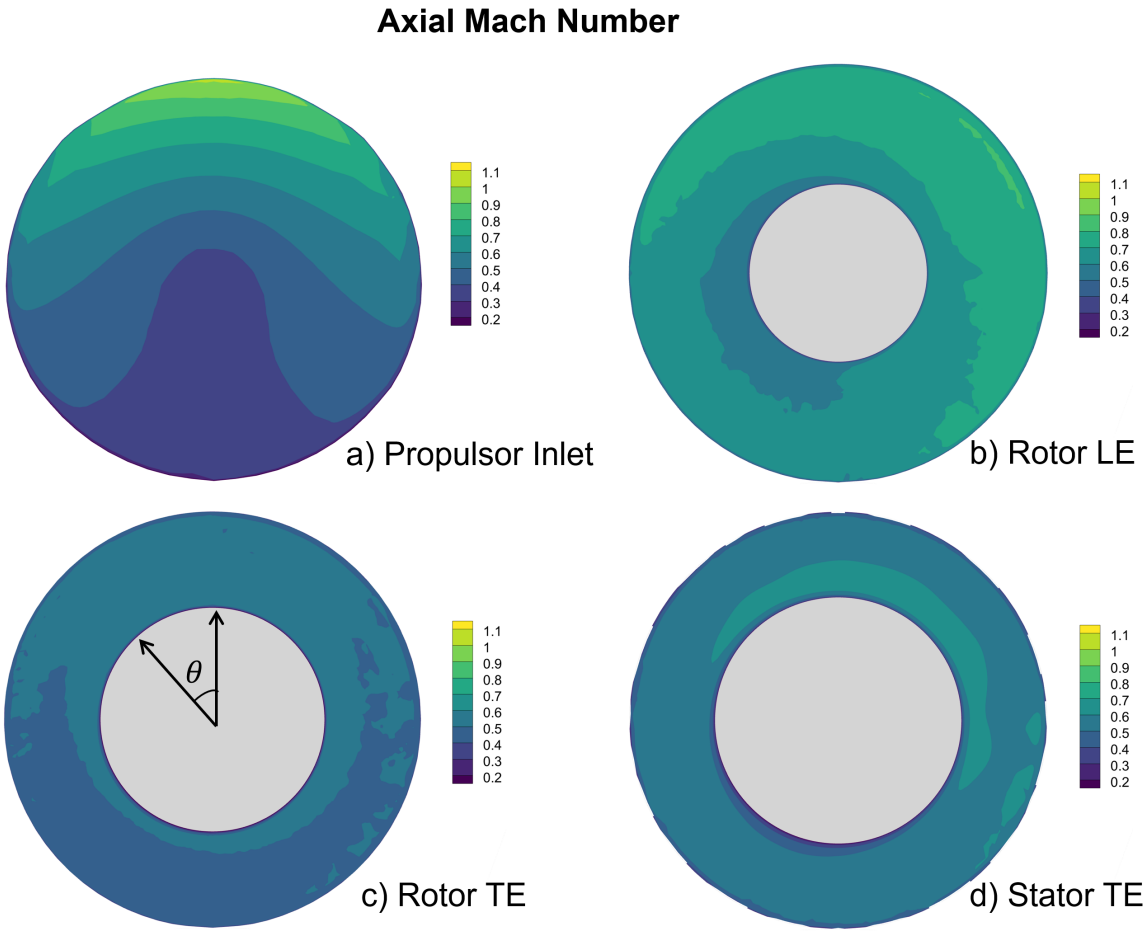



Figure 7-2: Attenuation of axial velocity non-uniformity across fan, due to the higher impact of the favorable pressure gradient on the lower-velocity flow. Station a), propulsor inlet (non-circular); station b), rotor LE; station c), rotor TE; station d), stator TE.

Figure 7-3 b) shows that the low pressure region has moved to the bottom of rotor LE plane. This is caused by acceleration of low-speed flow at the bottom of the boundary layer, where the stagnation pressure is the lowest. At the rotor TE, the region of maximum static pressure is located between $-60°$ and $0°$, with the region of minimum static pressure between $120°$ and $180°$. This non-uniformity pattern is similar to the stagnation pressure non-uniformity, because the flow velocity non-uniformity is small.

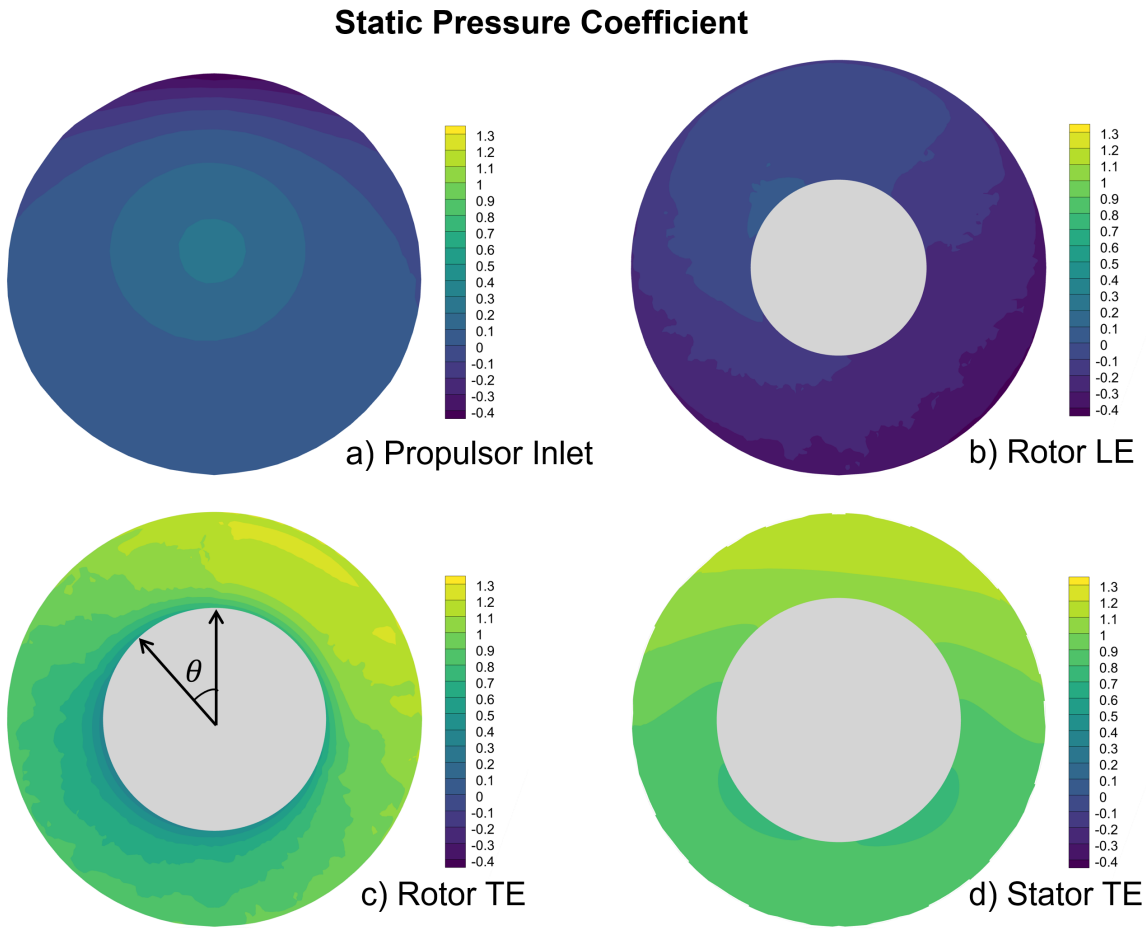



Figure 7-3: Static pressure at station a), propulsor inlet (non-circular); station b), rotor LE; station c), rotor TE; station d), stator TE.

Figure 7-4 shows that at the stator trailing edge, there is a static pressure non-uniformity, due to the non-zero flow angles. The stator exit flow angles range from $1°$ to $7°$ with corresponding swirl Mach numbers between 0 and -0.07, and mass-flow-averaged swirl Mach number of -0.03. At the nozzle exit, the swirl Mach number

swings between -0.3 and 0.3, as in Figure 7-5. The increase in the magnitude of the flow swirl (vorticity) is due to the decrease in the flow passage area at the nozzle exit compared with the stator trailing edge. A vortex tube gets stretched because of the decrease in the cross-sectional area, leading to an increase in the vorticity based on the Helmholtz theorem. The maximum magnitude of swirl Mach number is located at the top. This is due to the highest Mach number located at the top, which causes the most reduction in the flow cross-section area than other regions, compared with the stator trailing edge (where the flow Mach number is almost uniform). Because swirl flow reduces the propulsive efficiency, it would be beneficial to reduce the swirl exiting the nozzle. Guidelines to reduce the nozzle exit swirl should be considered in the future work.

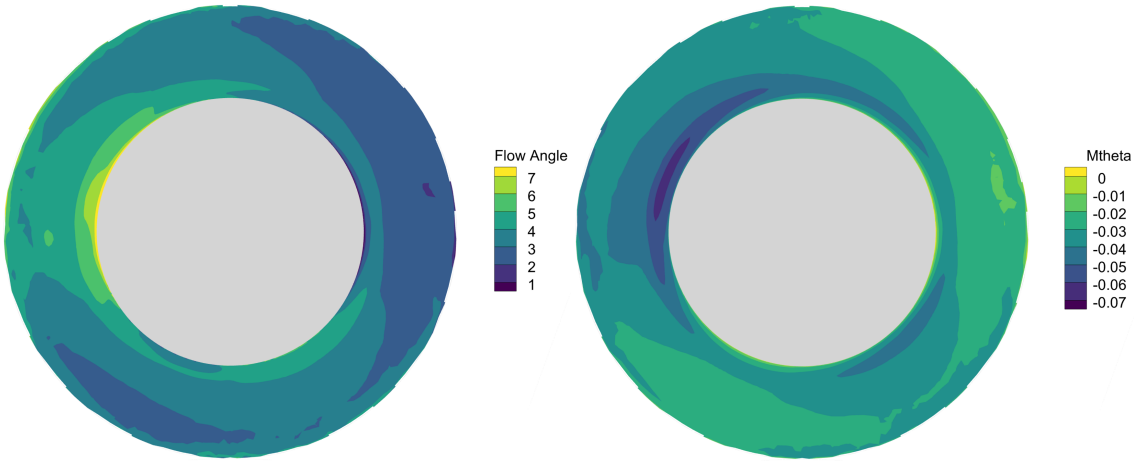



Figure 7-4: Flow angle and swirl non-uniformity at the stator trailing edge.

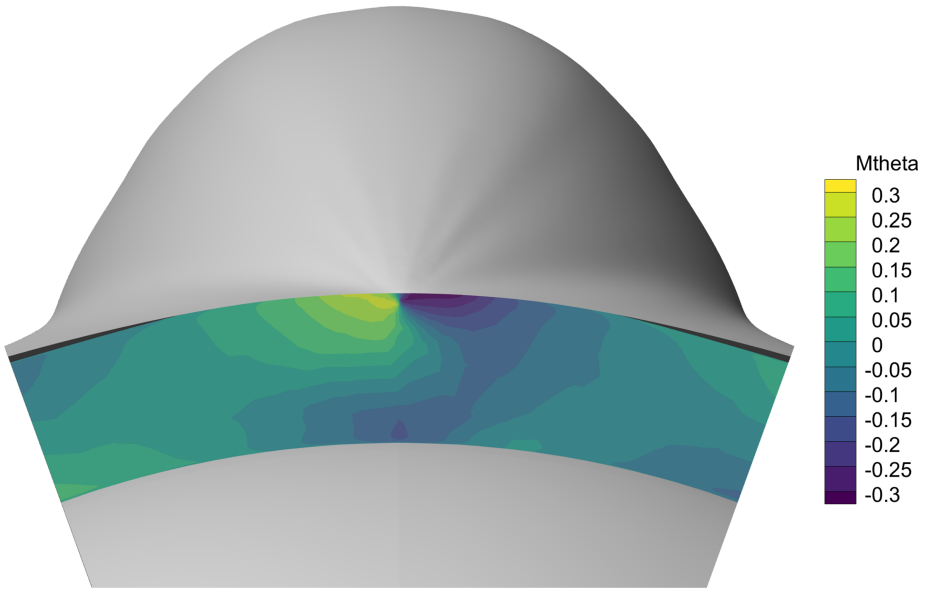



Figure 7-5: Swirl non-uniformity at the nozzle exit. The increase in the magnitude of the flow swirl (vorticity) is because of the decrease in flow passage area at the nozzle exit compared with the stator trailing edge. Because swirl flow reduces the propulsive efficiency, guidelines to reduce the nozzle exit swirl should be considered in future work.

## 7.2 PFEI Benefit of Tail BLI Aircraft

### 7.2.1 Relation between Shaft Power and PFEI

At cruise, the PFEI for the tail BLI aircraft is 10.4% lower than the baseline aircraft. The largest contribution to the improvement in PFEI is the reduction of airframe surface dissipation by 9.7% for the tail BLI aircraft than the baseline. That corresponds to the reduction of total net propulsive power[4] by the same percentage, 9.7%, for the tail BLI aircraft than the baseline. Further, the tail BLI aircraft has propulsive efficiency 5.6% higher than the baseline. The combined effects of reduced airframe surface dissipation and improved propulsive efficiency for the tail BLI aircraft result in a PFEI benefit of 10.4%. Table 7.1 shows the breakdown of engine propulsive power $P_{prop}$, shaft power $P_{shaft}$ and propulsive efficiency $\eta_p$ for the baseline and tail BLI

[4]Total net propulsive power must balance surface dissipation of the whole aircraft at cruise, based on the power balance relation.

aircraft configurations, respectively. The turbofans on tail BLI aircraft have a higher propulsive efficiency than those on the baseline aircraft, because the jet velocity is lower for the former[5]. The required shaft power[6] for the tail BLI aircraft is 3.2% lower than the baseline. The metric for the overall aircraft performance is PFEI, because it is directly proportional to the fuel consumption for the entire mission. Shaft power, however, is the quantity to be minimized during the process of fan design, and it can be computed directly in CFD.

| Baseline Aircraft | | Tail BLI Aircraft | |
|---|---|---|---|
| Turbofan Total $P_{prop}$ [kW] | 10826 | Turbofan Total $P_{prop}$ [kW] | 5682 |
| Turbofan Total $P_{shaft}$ [kW ] | 12127 | Turbofan Total $P_{shaft}$ [kW] | 6695 |
| Turbofan $\eta_p$ | 0.820 | Turbofan $\eta_p$ | 0.848 |
| | | Electric Fan Total $P_{prop}$ [kW] | 4094 |
| | | Electric Fan Total $P_{shaft}$ [kW] | 5042 |
| | | Electric Fan $\eta_p$ | 0.923 |
| Overall $\eta_p$ | 0.820 | Overall $\eta_p$ | 0.876 |
| Total Prop. System Weight [lb ] | 22537 | Total Prop. System Weight [lb ] | 21257 |
| Operating Empty Weight [lb] | 97289 | Operating Empty Weight [lb] | 95897 |
| PFEI [kJ/(kg $\cdot$ km) ] | 6.60 | PFEI [kJ/(kg $\cdot$ km) ] | 5.91 |

Table 7.1: Power, propulsive efficiency, and PFEI breakdown for baseline and tail BLI aircraft, respectively.

The reduction in shaft power has an exponential impact on the decrease in PFEI, which is explained as follows. PFEI is defined in terms of payload $W_{pay}$, fuel weight $W_{fuel}$, specific heating value $h_{fuel}$, and total range $R_{total}$:

$$\text{PFEI} = \frac{W_{fuel} h_{fuel}}{g W_{pay} R_{total}}. \tag{7.2}$$

The quantities $W_{pay}$ and $R_{total}$ are constant for the present analyses, and $g$ is the gravitational constant. The rate of fuel consumption $\dot{m}_{fuel}$ can be related to the shaft power via the specific heating value $h_{fuel}$, thermal efficiency $\eta_{th}$[7] and transfer

[5]The jet Mach number is 0.99 for the turbofans on the tail BLI aircraft and 1.06 for the baseline.
[6]The total shaft power to power all the engines.
[7]Defined as the ratio of kinetic energy change rate to fuel chemical energy consumption rate.

efficiency $\eta_{tr}$[8]:

$$\dot{m}_{fuel} = \frac{P_{shaft}}{h_{fuel}\eta_{th}\eta_{tr}}. \tag{7.3}$$

Based on the Breguet equation, the weight ratio $\frac{W_{C2}}{W_{C1}}$ with range $R_{cruise}$ can be written as

$$\frac{W_{C2}}{W_{C1}} = \exp\left[-\left(\frac{g}{W}\frac{1}{V}\frac{P_{shaft}}{h_{fuel}\eta_{th}\eta_{tr}}\right)R_{cruise}\right]. \tag{7.4}$$

The quantity $V$ is the cruise velocity. The cruise fuel burn $W_{fuel}^{cruise}$ is given by

$$W_{fuel}^{cruise} = W_{C1} - W_{C2}. \tag{7.5}$$

Reducing the shaft power $P_{shaft}$ decreases the fuel burn during cruise (from C1 to C2 of the flight profile in Figure 2-1) exponentially. Cruise accounts for 86% of fuel used in the mission[9], so the total fuel consumption $W_{fuel}$ and thus PFEI also decrease exponentially with respect to the reduction in shaft power at cruise.

### 7.2.2 Sensitivity of PFEI Benefit versus Tail BLI Electric Fan Efficiency

The BLI benefit in terms of PFEI is defined as

$$\text{BLI Benefit} = \frac{\text{PFEI}_{\text{baseline}} - \text{PFEI}_{\text{TailBLI}}}{\text{PFEI}_{\text{baseline}}}. \tag{7.6}$$

The PFEI benefit for tail BLI aircraft with an installed electric fan efficiency $\eta_{fan} = 0.878$, is 10.4% compared with the baseline. The sensitivity to the installed electric fan efficiency, can be found by varying the tail BLI electric fan efficiency while holding the underwing turbofan efficiency constant. Figure 7-6 indicates that a 1% increase in tail BLI electric fan efficiency produces a BLI benefit increase of approximately 0.8%.

[8]Defined as the ratio of shaft power to kinetic energy change rate.
[9]Based on the TASOPT analysis.

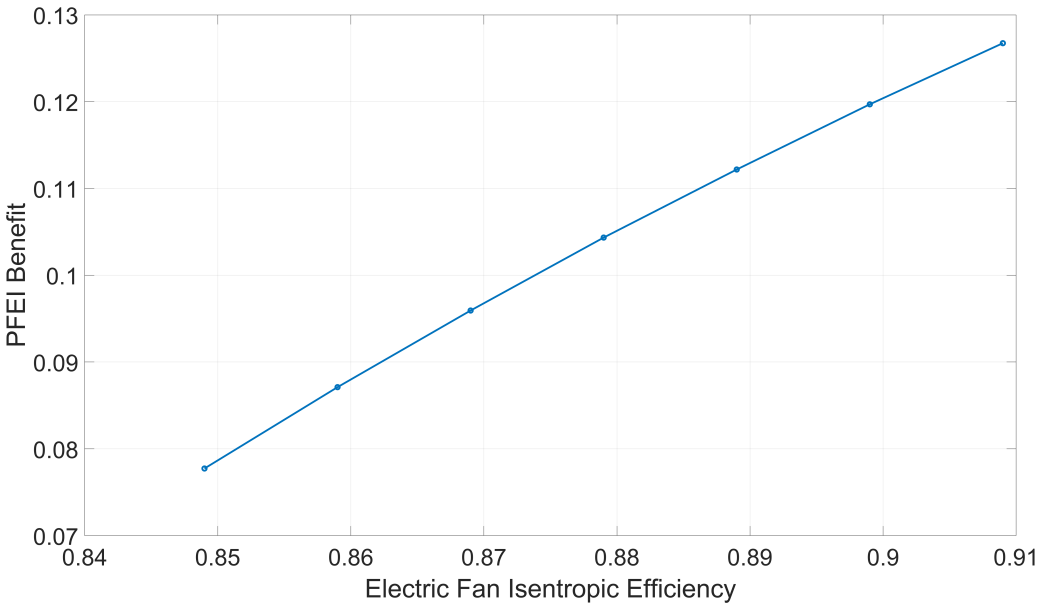



Figure 7-6: Sensitivity of PFEI benefit versus tail BLI electric fan installed efficiency by TASOPT analysis. A 1% increase in tail BLI electric fan efficiency leads to a BLI benefit increase of approximately 0.8%.

## 7.3 Comparison with Similar Tail BLI Conceptual Aircraft

A tail BLI aircraft concept for a similar mission is NASA STARC-ABL. Hall et al. [20] showed an increase in fuel burn by 5% for the STARC-ABL configuration, compared to an equivalent twin turbofan configuration. STARC-ABL has a tail cone fan of $\eta_{fan} = 94\%$, which is a more efficient conceptual tail BLI fan compared with ours[10]. The tail BLI fan of STARC-ABL has a diameter of 77 in and total pod weight of 2311 lb. Our nine integrated propulors have an individual fan diameter of 24 in, and the total pod weight of nine propulsors is 1366 lb. The fuel burn increase for STARC-ABL is caused by the total propulsion system mass 38% higher than the baseline configuration, and the operating empty mass 6.8% higher than the baseline. This weight penalty surpasses the propulsive efficiency increase due to

[10]The inflow condition seen by the tail cone fan is almost axisymmetric, and the non-uniformity is in the radial direction. It is thus feasible to design a tail cone fan that operates at a higher efficiency than our tail BLI fan. An isentropic efficiency of 94%, however, is still high for a fan even in uniform flow.

BLI, leading to an increase in mission fuel burn compared with the baseline. For our tail BLI aircraft, however, the total propulsion system mass is 5.7% lower than the baseline and operating empty mass is 1.5% lower. This reduced weight and the improved propulsive efficiency leads to 10.4% fuel burn reduction for our tail BLI aircraft compared with the baseline twin turbofan aircraft.

THIS PAGE INTENTIONALLY LEFT BLANK

# Chapter 8

# Summary and Conclusions

## 8.1 Primary Learnings

The four major learnings in this thesis are (i) the aerodynamic attributes needed for integration of an array of BLI propulsors on the tail of a mid-range civil aircraft, (ii) design guidelines to achieve these attributes, (iii) conceptual design of a BLI aircraft with a 10.4% benefit in PFEI compared to a baseline aircraft, including its sensitivity versus the installed fan efficiency and (iv) challenges in moving up the technology readiness level.

An appropriate integration of the tail BLI propulsors requires smooth transitions between the tail and inlet and between the tail and nozzle, to eliminate flow separation in these regions. Because the nozzle exit area is smaller than the propulsor inlet area, there is diffusion in the channel between adjacent propulsors when approaching the nozzle exit. Especially in the case of a circular nozzle, the flow diffusion can become excessive and result in flow separation between nacelles. The tail BLI propulsor design needs to eliminate this flow separation, as done in the current aircraft using a tailored nozzle design. For fans with BLI, the rotor inlet incidence angle variation imposes a penalty on isentropic efficiency; the design of tail BLI fans needs to include low efficiency drop with incidence. In summary, design guidelines are described for the number of integrated propulsors, the propulsor inlet, nacelle, and nozzle, and the tail BLI fans, respectively.

- The proposed design uses nine BLI propulsors with electric fans on an axisymmetric tail, which is installed on a baseline single-aisle airplane with twin underwing low-FPR turbofans. The propulsor inlet includes an upstream extension, which achieves a smooth transition between the tail and inlet and eliminates reverse flow. The outer contour of nacelle follows the profiles of supercritical airfoils in order to delay (or weaken) shock waves. An annular nozzle shared by all tail BLI propulsors was found to be essential for eliminating flow separation between adjacent propulsors.

- A fan designed for tail BLI should have a low efficiency penalty for rotor inlet incidence away from the nominal design point; i.e. the profile loss bucket should have a wide low loss region around the minimum loss. This is a major technology challenge in moving up the technology readiness level. Non-axisymmetric stators can yield some reduction in rotor inlet incidence distortion, but effectiveness is limited if the rotor relative flow is mostly supersonic, as in the current example.

The benefit of a "tail BLI and twin underwing turbofans" aircraft configuration was estimated as 10.4% in PFEI at a cruise Mach number of 0.8 and an altitude of 35100 ft, compared to a baseline twin turbofan configuration. For the configuration investigated, a 1% increase in the tail BLI fan efficiency leads to approximately 0.8% rise in PFEI benefit.

## 8.2 Future Work

There are four specific aspects recommended for advancing the design. First, a sensitivity study of tail BLI benefit versus the number of integrated propulsors should be carried out to determine the optimal propulsor configuration. The current design of nine propulsors integrated on the tail might be improved by using a different number of tail-mounted BLI propulsors.

Second, the strategy for blade design with a wide low loss region needs to be

created. In this thesis, it has been shown that a rotor with such feature has the potential to improve PFEI.

Third, the impact of stator exit and nozzle exit swirl on propulsive efficiency should be determined, and design guidelines to reduce flow swirl need to be established. In the current design, stator exit and nozzle exit swirl were observed, and it would be useful to establish the physical rationale to tackle this issue.

Finally, the current work was focused on assessing the integrated propulsors at cruise. The aerodynamic performances of tail BLI propulsors should be evaluated at off-design conditions (takeoff, landing, etc.) to ensure that performance goals (separation-free, shock-free, etc.) are met.

THIS PAGE INTENTIONALLY LEFT BLANK

# Appendix A

# Mechanical Power and Entropy Generation Ingested by Tail BLI Propulsors

## A.1 Non-Dimensionalization in CFD

All the physical quantities used in the CFD analyses are non-dimensionalized by freestream stagnation quantities (as reference quantities) at the specified altitude and flight Mach number, which is determined via TASOPT analysis, as shown below

$$p^* = \frac{p}{p_{t,\infty}}, \tag{A.1}$$

$$T^* = \frac{T}{T_{t,\infty}}, \tag{A.2}$$

$$\rho^* = \frac{\rho}{\rho_{t,\infty}}, \tag{A.3}$$

$$R^* = \frac{R}{R_\infty}. \tag{A.4}$$

In Equations from A.1 to A.4, the superscript $*$ denotes the non-dimensionalized property, the subscript $t$ refers to the stagnation quantity, and the subscript $\infty$ represents the freestream state. The freestream stagnation properties are related by the

ideal gas law $p_{t,\infty} = \rho_{t,\infty} R_\infty T_{t,\infty}$. The reference velocity $V_{ref}$ and the non-dimensional velocity $V^*$ are defined as

$$V_{ref} = \sqrt{\frac{p_{t,\infty}}{\rho_{t,\infty}}} \tag{A.5}$$

$$V^* = \frac{V}{V_{ref}} \tag{A.6}$$

The non-dimensional freestream velocity is therefore defined as $V_\infty = M_\infty V_{ref}$.

## A.2 Mechanical Power and Entropy Generation Ingested vs. Propulsor Inlet Area

Consistent with the CFD non-dimensionalization, the mechanical power $P_K$ is normalized by $\rho_\infty V_\infty^3$ and the propulsor inlet area is normalized by the fuselage radius $r_{fuse}^2$. Figure A-1 shows a series of concentric cuts placed at the nacelle highlight to determine the total mechanical power and the mass-flow average of the entropy passing through the various areas.

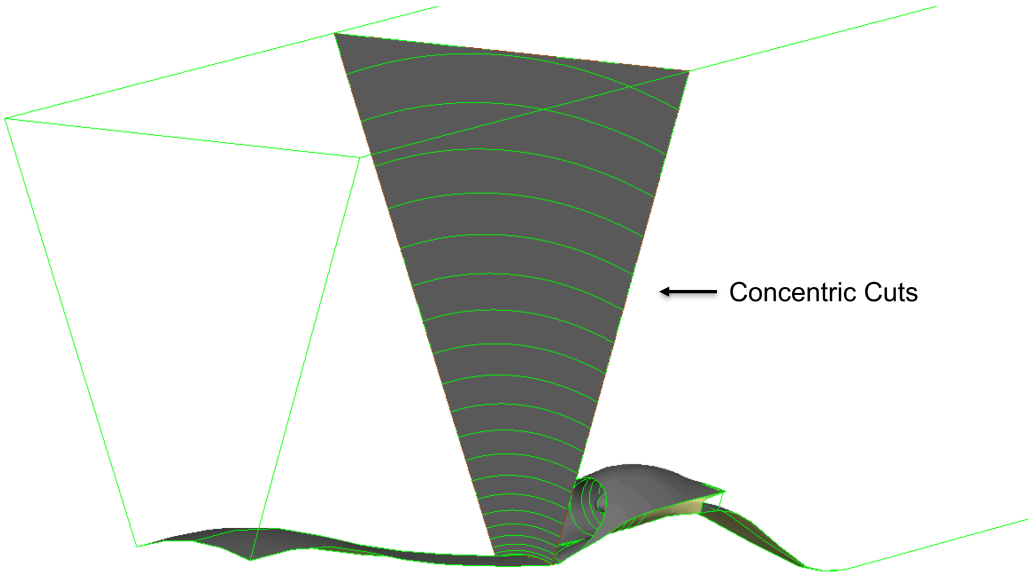



Figure A-1: Concentric cuts at nacelle highlight to determine relation of mechanical power and entropy generation ingested vs. propulsor inlet area.

An S-shaped tail was chosen rather than an arc-shaped tail due to the larger $P_{K,inl}$ that was found for the S-shaped tail profile, thus resulting in larger ingested mechanical power. Figure A-2 illustrates the two types of tail profiles and Figures A-3, A-4 show the mechanical power $P_{K,inl}$ and entropy generation $\Delta s_{inl}$ ingested by the propulsor versus the inlet area $A_{inl}$.

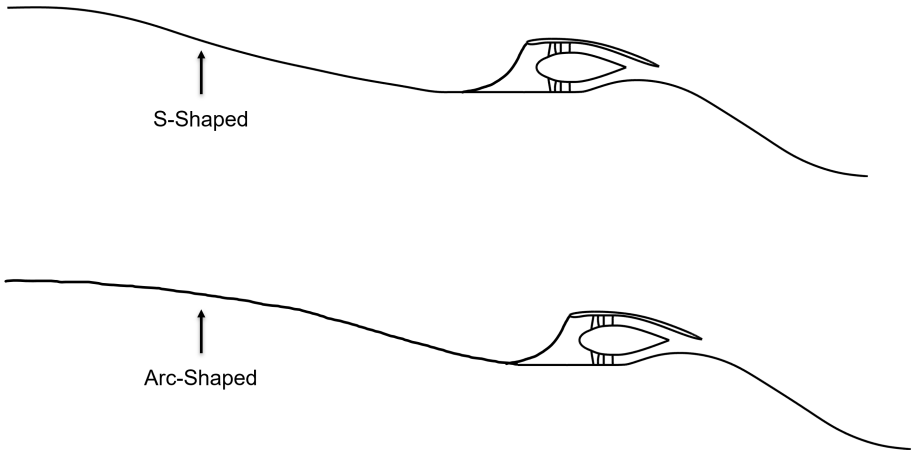



Figure A-2: Two types of tail necking profiles for tail BLI propulsors.

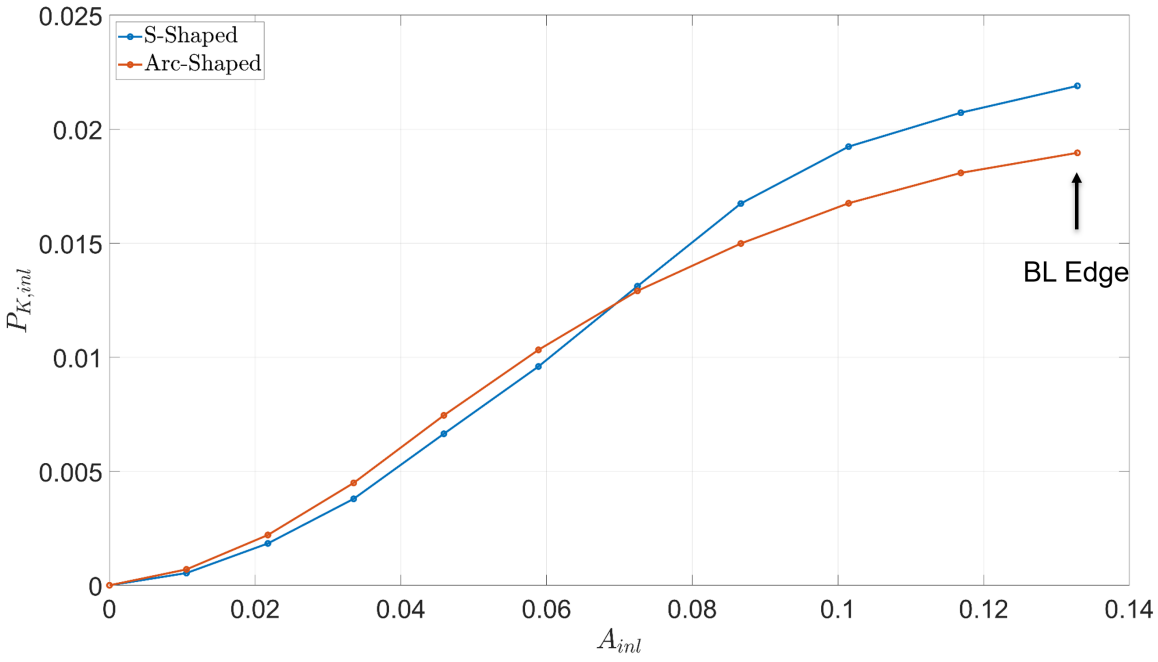



Figure A-3: Relation between mechanical power ingested $P_{K,inl}$ and propulsor inlet area. An S-shaped tail profile is preferred because of the larger $P_{K,inl}$.

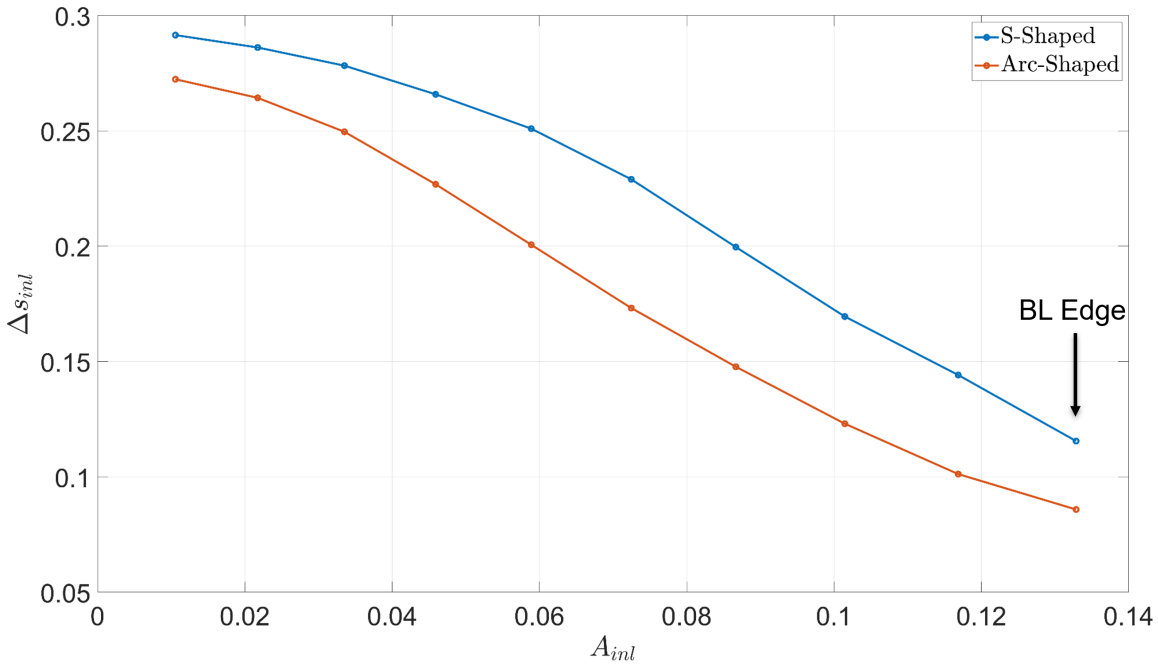



Figure A-4: Relation between entropy ingested and propulsor inlet area. The S-shaped profile has larger mass-flow average ingested entropy than that for the arc-shaped tail for a propulsor inlet height equal to the local boundary layer thickness.

For the S-shaped tail profile, the curve fits for mechanical power $P_{K,inl}$ and entropy generation $\Delta s_{inl}$ versus inlet area $A_{inl}$ are

$$P_{K,inl} = 2159.832A_{inl}^5 - 659.527A_{inl}^4 + 48.728A_{inl}^3 + 0.982A_{inl}^2 + 0.0482A_{inl} \tag{A.7}$$

$$\Delta s_{inl} = -21571.470A_{inl}^5 + 8438.079A_{inl}^4 - 1124.237A_{inl}^3 + 51.729A_{inl}^2 - 1.507A_{inl} + 0.303 \tag{A.8}$$

# Appendix B

# Body-Force Camber Surface Optimization Framework

## B.1 Governing Equations and Turbulence Model

In this project, all CFD simulations are carried out in the SANS framework, which uses the compressible Reynolds-Averaged Navier-Stokes (RANS) equations with the Spalart-Allmaras (SA) turbulence model [27] in a fully turbulent mode with modifications proposed by Allmaras et al. [1] to improve the solver robustness[1]. Molecular and turbulent Prandtl numbers are taken as constant: $Pr = 0.72$, $Pr_t = 0.9$, with the molecular viscosity governed by Sutherland's law [29].

The RANS-SA governing equations (ordered as continuity, moment, energy, and turbulence model) with the body-force and quasi-1D blockage models are

$$\mathcal{R}(\boldsymbol{u}) \equiv \frac{\partial b\boldsymbol{u}}{\partial t} + \nabla \cdot \left( b\vec{\boldsymbol{F}}_{\mathsf{i}}(\boldsymbol{u}) - b\vec{\boldsymbol{F}}_{\mathsf{v}}(\boldsymbol{u}, \nabla\boldsymbol{u}) \right) + b\boldsymbol{\mathcal{S}}_{\mathsf{SA}}(\boldsymbol{u}, \nabla\boldsymbol{u}) + b\boldsymbol{\mathcal{S}}_{\mathsf{BF}}(\boldsymbol{u}) = \boldsymbol{0}, \quad \text{(B.1)}$$

where $\boldsymbol{u}$ are the conservation variables, $b$ is the quasi-1D area restriction to model blockage, $\vec{\boldsymbol{F}}_{\mathsf{i}}$ and $\vec{\boldsymbol{F}}_{\mathsf{v}}$ are inviscid and viscous fluxes, respectively, $\boldsymbol{\mathcal{S}}_{\mathsf{SA}}$ are source terms in the SA equation, and $\boldsymbol{\mathcal{S}}_{\mathsf{BF}}$ are the body-force source terms; all have six components in 3D. In this thesis, blockage effects are not considered, so $b = 1$.

[1] Established and implemented by Dr. Marshall Galbraith.

The body-force term,

$$\boldsymbol{\mathcal{S}}_{\mathsf{BF}}(u) = \begin{bmatrix} 0 \\ -\rho\vec{\mathrm{f}} \\ -\rho\vec{\mathrm{f}} \cdot \vec{U} \\ 0 \end{bmatrix}, \tag{B.2}$$

only contributes to the momentum and energy equations, where $\vec{\mathrm{f}}$ is the body-force and $\vec{U}$ is the local blade rotational speed. The body-force can be decomposed as $\vec{\mathrm{f}} = \vec{\mathrm{f}}_{\mathsf{n}} + \vec{\mathrm{f}}_{\mathsf{v}}$. The normal component of the body-force $\vec{\mathrm{f}}_{\mathsf{n}}$ turns the flow without any viscous losses while the parallel component $\vec{\mathrm{f}}_{\mathsf{v}}$ models the viscous dissipation and the entropy generation. The RANS equations with body-forces are discretized using a Continuous Galerkin (CG) finite element method (FEM) stabilized by the Streamline Upwind Petrov-Galerkin (SUPG)[12] with the SANS framework.

## B.2 Body-Force Camber Surface Optimization Statement

The power balance states that the airframe dissipation must be balanced by the net propulsive power for a fan operating at cruise. The tail-integrated propulsor nozzle area is fixed by geometry in the design process[2]. The fan face axial Mach number and stagnation pressure ratio is thus a function of the fan rotational speed $\Omega$. For the purpose of simplification, the discrete equations $\mathcal{R}_h(\boldsymbol{u}_h)$, are augmented by a single discrete global constraint equation

$$R_{J,h}(\boldsymbol{u}_h) = \mathcal{J}_h(\boldsymbol{u}_h) - \mathcal{J}_{spec} \tag{B.3}$$

where $\mathcal{J}_h(u_h)$ is an output functional and $\mathcal{J}_{spec}$ is the corresponding target value of $\mathcal{J}_h(u_h)$. For the tail BLI propulsors, $\mathcal{J}_h(u_h)$ is taken as the net propulsive power $P_{prop}$ and $\mathcal{J}_{spec}$ is therefore the power requirement determined by TASOPT. For the fan in

[2]For a fan stage in an isolated duct, the pressure ratio is controlled by setting the static back pressure for a given inflow stagnation pressure.

an isolated duct with BLI, however, $\mathcal{J}_h(u_h)$ is the fan face axial Mach number and $\mathcal{J}_{spec}$ is thus the expected value for the operating point. With the rotational speed $\Omega$ as a free variable, the augmented discrete residual and solution state can be denoted

$$\tilde{\mathcal{R}}_h(\tilde{\boldsymbol{u}}_h) = [\mathcal{R}_h(\tilde{\boldsymbol{u}}_h), R_{J,h}(\tilde{\boldsymbol{u}}_h)] \tag{B.4}$$

$$\tilde{\boldsymbol{u}}_h = [\boldsymbol{u}_u, \Omega] \tag{B.5}$$

To explore the ways to mitigate the inlet distortion and improve the fan isentropic efficiency for BLI, an optimization statement is set up using the vector of parameters that define the body-force camber surface, denoted as $\boldsymbol{\eta}$. Because the propulsive shaft power is a surrogate for PFEI, the optimization statement[3] can be expressed as

$$\begin{aligned} &\text{Find } \boldsymbol{\eta} \text{ such that} \\ &\quad P_{\mathsf{shaft}}(\tilde{\boldsymbol{u}}_h) \text{ is minimized} \\ &\text{subject to} \qquad \tilde{\mathcal{R}}_h(\tilde{\boldsymbol{u}}_h; \boldsymbol{\eta}) = 0, \end{aligned} \tag{B.6}$$

where $\boldsymbol{\eta}$ is a set of parameters that define the body-force camber surface. A gradient-based optimization can minimize the evaluation times of object functions, but it requires computing the derivatives of objective functions with respect to each optimization parameter, $\eta_i$. Giles and Pierce[14] showed that an efficient computation method is to use an adjoint, $\psi$, based on the equations as follows

$$\frac{dP_{\mathsf{shaft}}}{d\eta_i} = -\psi^T \frac{\partial \tilde{\mathcal{R}}_h(\tilde{\boldsymbol{u}}_h; \eta_i)}{\partial \eta_i} + \frac{\partial P_{\mathsf{shaft}}}{\partial \eta_i}, \tag{B.7}$$

$$\psi = \left[\frac{\partial \tilde{\mathcal{R}}_h}{\partial \tilde{\boldsymbol{u}}_h}\right]^{-T} \left[\frac{\partial P_{\mathsf{shaft}}}{\partial \tilde{\boldsymbol{u}}_h}\right]^T. \tag{B.8}$$

The transposed Jacobian of the discrete system is required for the adjoint calculation, whose value is then used for computing all partial derivatives with respect to optimization parameter.

The derivative of the discrete residual $\frac{\partial \tilde{\mathcal{R}}_h(\tilde{\boldsymbol{u}}_h; \eta_i)}{\partial \eta_i}$ is computed according to the

[3]Established and implemented by Dr. Marshall Galbraith.

chain rule

$$\frac{\partial \tilde{\mathcal{R}}_h(\tilde{\boldsymbol{u}}_h;\eta_i)}{\partial \eta_i} = \frac{\partial \tilde{\mathcal{R}}}{\partial \vec{\mathrm{f}}} \cdot \frac{\partial \vec{\mathrm{f}}}{\partial \hat{n}} \cdot \frac{\partial \hat{n}}{\partial \eta_i} \tag{B.9}$$

where the term $\hat{n}$ is the normal vector of the body-force camber surface.

# Appendix C

# Body-Force Camber Surface Optimization for BLI

The boundary layer profile at the propulsor inlet (CFD) is shown in Figure C-1, which is used as the inflow boundary condition for the body-force camber surface optimization. This enables the tail BLI fan design (in the isolated duct) to be implemented in an environment consistent with the tail-integrated propulsor.

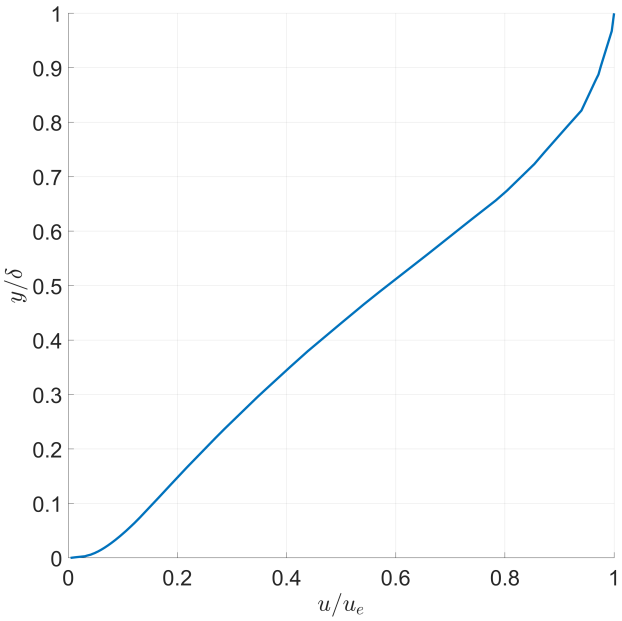



Figure C-1: Boundary layer profile at the tail propulsor inlet is used as the inflow boundary condition for isolated duct, to enable the tail BLI fan design in an environment consistent with the tail-integrated propulsor.

The fan body-force camber surface is optimized to minimize shaft power at tail BLI design. We started with body-force camber surface inspired by NASA Rotor 67 with modified flow path for the tail BLI operating condition. Figure C-2 shows the body-force camber lines near root (section 1), at mid span (section 2), and near tip (section 3) for the baseline and optimized, respectively. The changes in body-force camber lines from the baseline to the optimized are illustrated by Figure C-3.

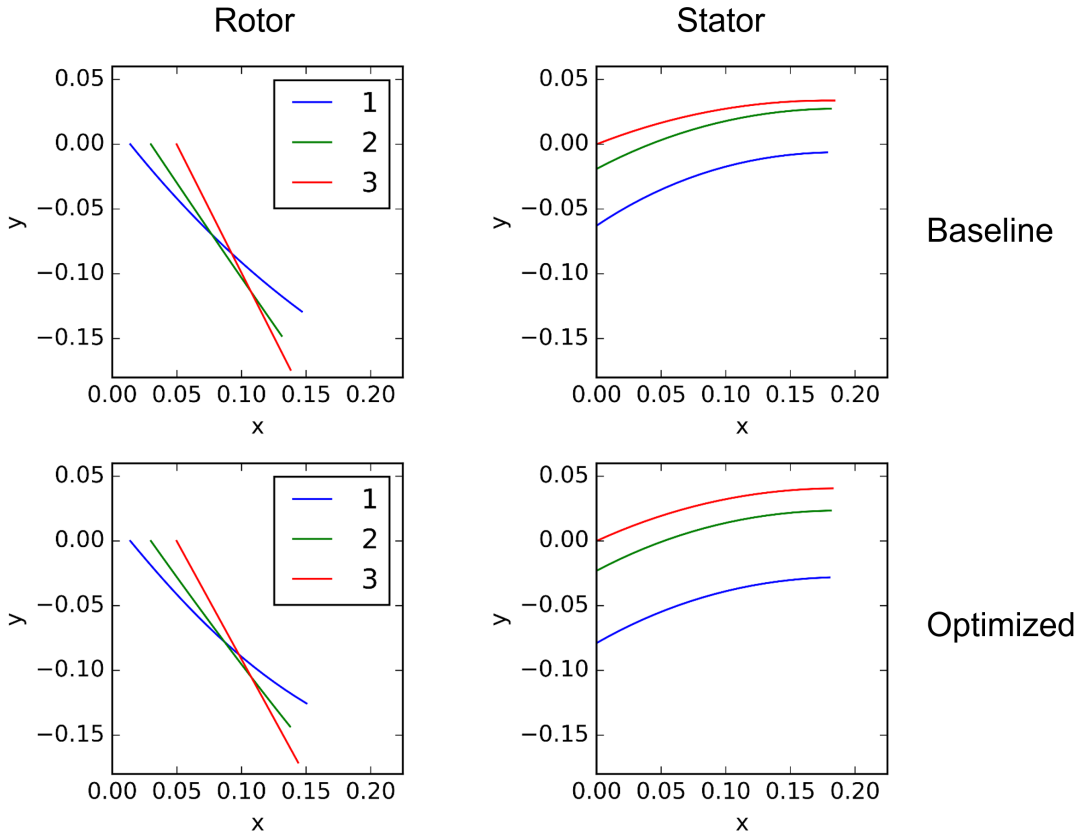



Figure C-2: Comparison of baseline and optimized body-force camber lines.

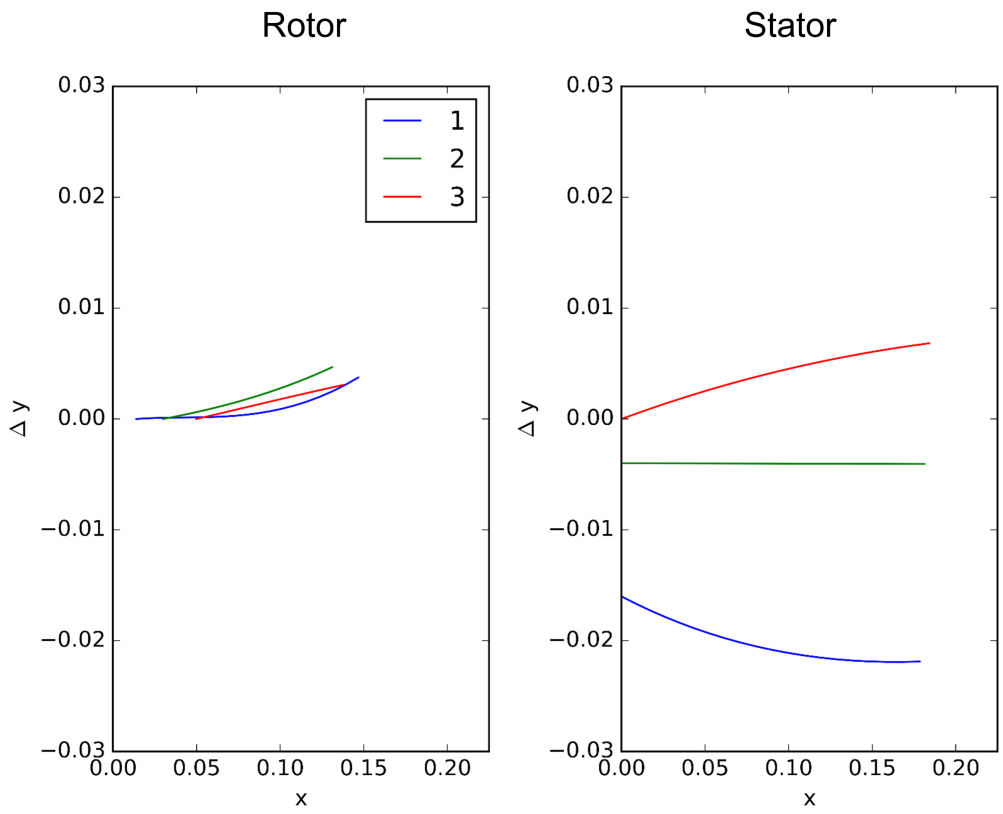



Figure C-3: Changes in body-force camber lines between optimized and baseline. The changes in the rotor body-force camber lines are smaller than changes in the stator body-force camber lines.

With the body-force camber surface optimization, the shaft power is reduced by about 1% due to the increase in fan isentropic efficiency by approximately 1%. More uniform stagnation pressure is seen at the rotor trailing edge, as in Figure C-4. This implies more attenuation of stagnation pressure non-uniformity by the optimized rotor than the baseline.

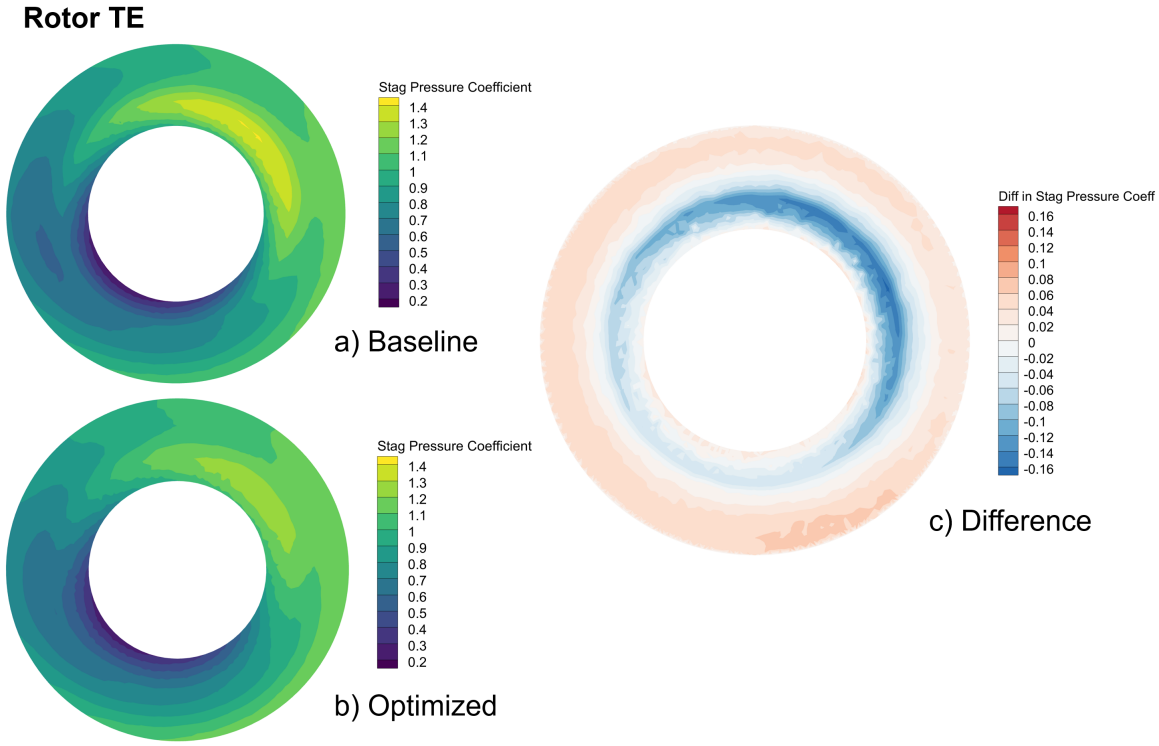



Figure C-4: Stagnation pressure more uniform at rotor TE for optimized than baseline. This implies more attenuation of stagnation pressure non-uniformity by the optimized rotor than the baseline.

# Appendix D

# Tail Boundary Layer Profiles from 3D CFD of a Full Aircraft

Three-dimensional CFD calculations have been carried out for a half of the full aircraft by MHI. Boundary layer profiles were extracted at the end of the constant-radius fuselage, i.e. $x = 27.9\,m$, as shown in Figure D-1. There are seven circumferential locations to extract the boundary layer, which are marked as red dots in Figure D-2. The approximation by the 2D Coles boundary layer profile is 99% accurate in terms of the kinetic energy deficit at all the circumferential locations except 90°. Details of the boundary layer profiles and approximations by the 2D Coles profile are depicted in Figure D-3.

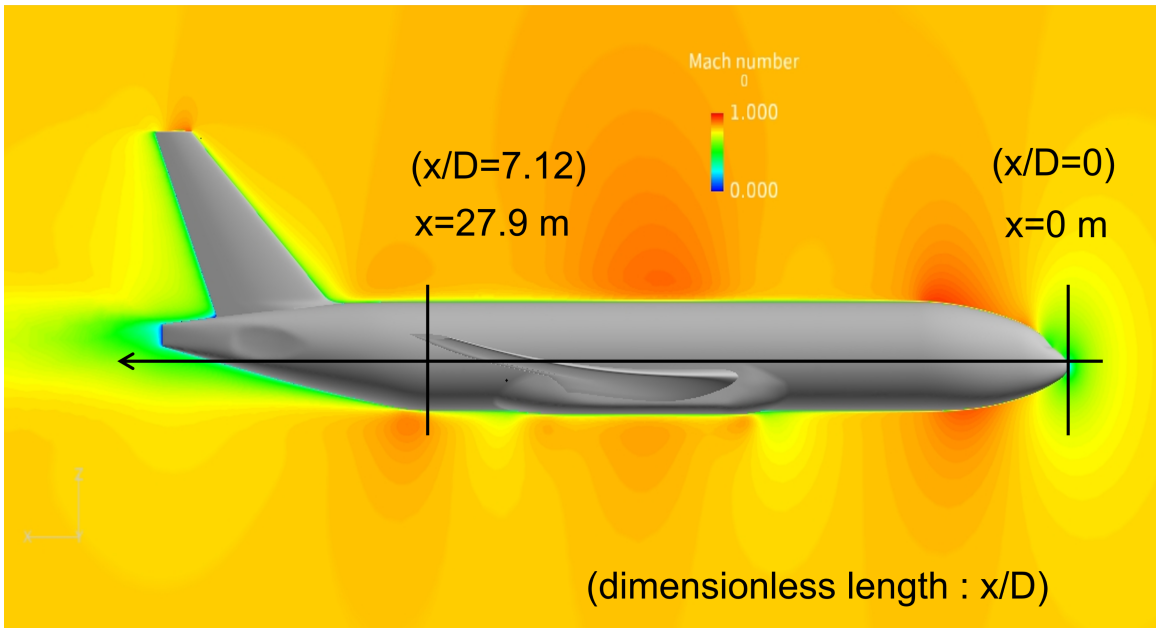



Figure D-1: Meridional contour of Mach number. Boundary layer profile extracted at $x = 27.9m$, i.e. the end of constant-radius fuselage. Figure courtesy of MHI.

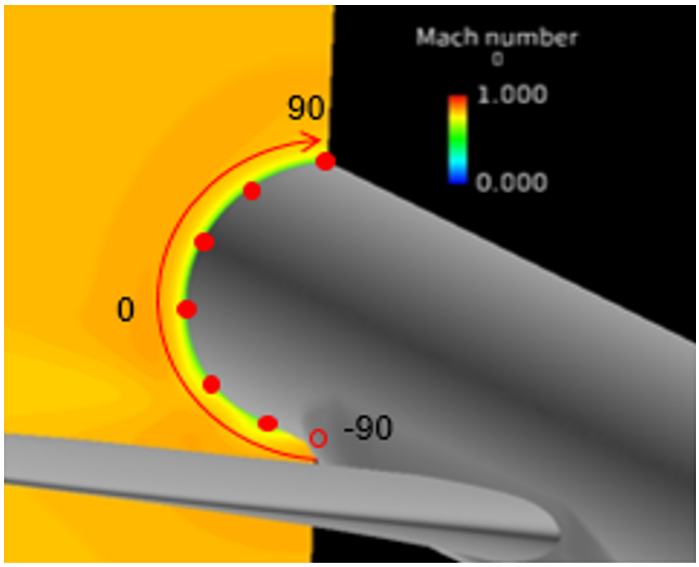



Figure D-2: Seven circumferential locations to extract boundary layer profiles. Figure courtesy of MHI.

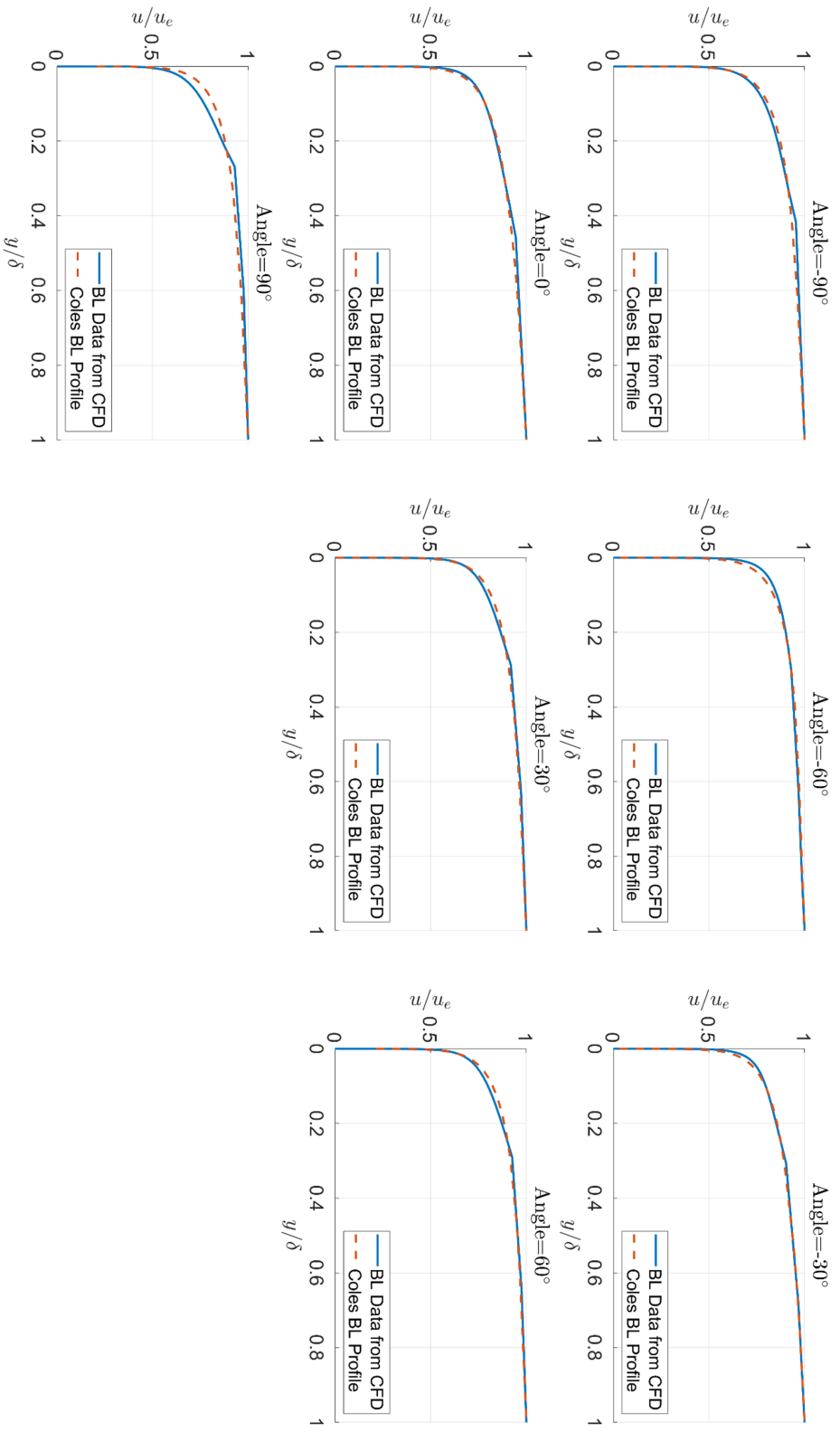



Figure D-3: CFD boundary layer approximations by 2D Coles profile. The approximation by the 2D Coles boundary layer profile is 99% accurate in terms of the kinetic energy deficit at all the circumferential locations except 90°.

THIS PAGE INTENTIONALLY LEFT BLANK

# Appendix E

# Geometry of Tail and Tail-Integrated Propulsors

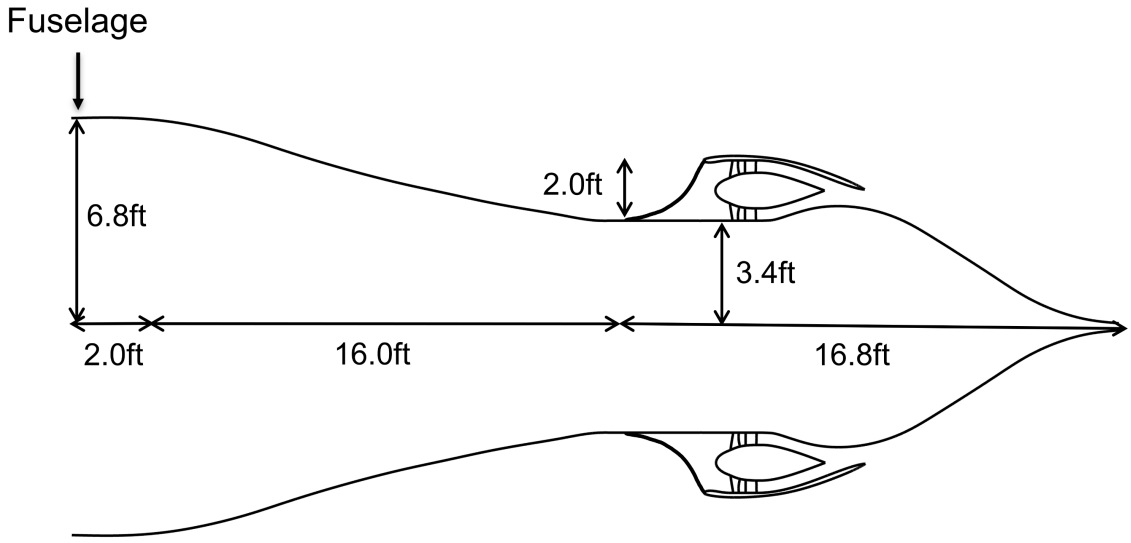



Figure E-1: Centerline profiles of the axisymmetric tail with top and bottom BLI propulsors. Actual dimensions included.

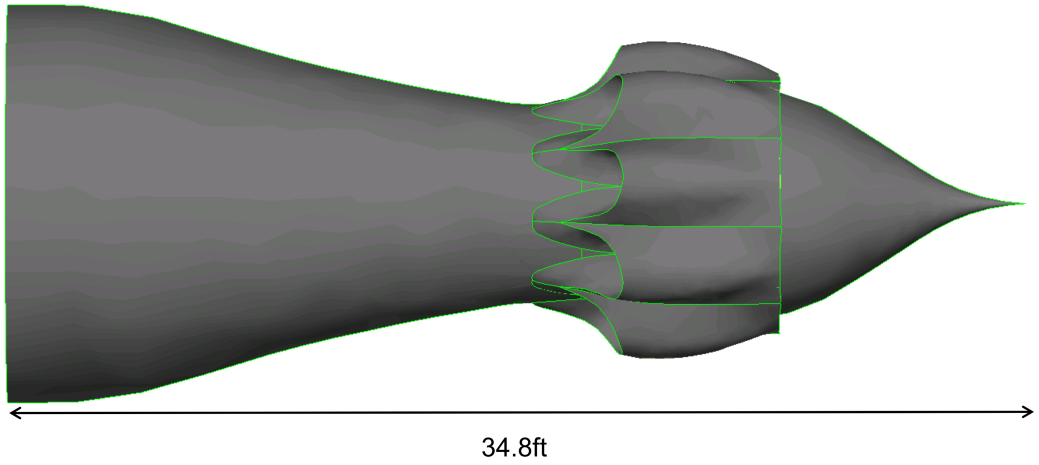



Figure E-2: Side view of the axisymmetric tail with integrated BLI propulsors.

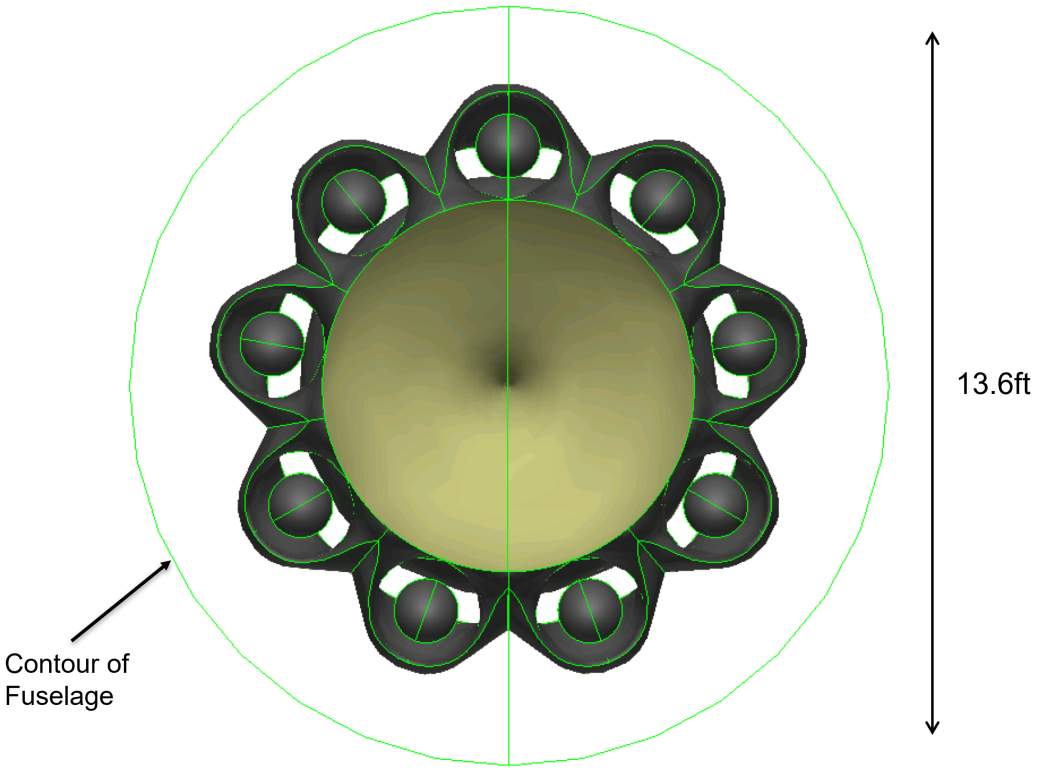



Figure E-3: Front view of the axisymmetric tail with integrated BLI propulsors. The tail upstream of the integrated propulsors is hidden to make the propulsors visible.

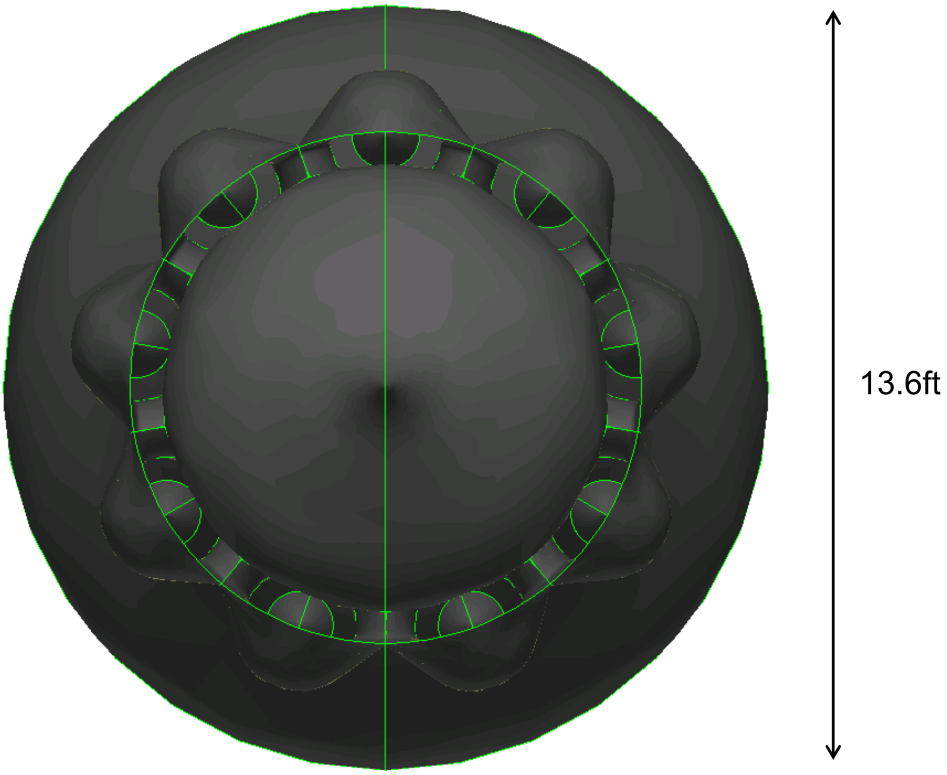



Figure E-4: Rear view of the axisymmetric tail with integrated BLI propulsors.

THIS PAGE INTENTIONALLY LEFT BLANK

# Bibliography


[1] Steven R. Allmaras, Forrester T. Johnson, and Philippe R. Spalart. Modifications and clarifications for the implementation of the Spalart-Allmaras turbulence model. Seventh International Conference on Computational Fluid Dynamics, Big Island, Hawaii, July 2012.

[2] Krishan Chana and Robert Miller. The Effect of Reaction on Compressor Performance. *Journal of Turbomachinery*, pages 1–15, 01 2021.

[3] Yuankang Chen. Topics on Conceptual Design of the D8 aircraft : Fuel Burn Uncertainty Estimate and BLI Propulsor Loss Modeling. Master's thesis, Massachusetts Institute of Technology, Department of Aeronautics and Astronautics, 2017.

[4] Jeffrey J. Defoe and Zoltán S. Spakovszky. Effects of Boundary-Layer Ingestion on the Aero-Acoustics of Transonic Fan Rotors. *Journal of Turbomachinery*, 135(5), 06 2013. 051013.

[5] J. D. Denton. Loss Mechanisms in Turbomachines. ASME 93-GT-435, May 1993.

[6] Mark Drela. Power Balance in Aerodynamic Flows. *AIAA Journal*, 47(7):1761–1771, 2009.

[7] Mark Drela. Development of the D8 Transport Configuration. AIAA 2011-3970, June 2011.

[8] Mark Drela. *TASOPT 2.00 Transport Aircraft System OPTimization Technical Description*, 2020.

[9] V. Jerez Fidalgo, C. A. Hall, and Y. Colin. A Study of Fan-Distortion Interaction Within the NASA Rotor 67 Transonic Stage. *Journal of Turbomachinery*, 134(5), 05 2012. 051011.

[10] Razvan V. Florea, Dmytro Voytovych, Gregory Tillman, Mark Stucky, Aamir Shabbir, Om Sharma, and David J. Arend. Aerodynamic Analysis of a Boundary-Layer-Ingesting Distortion-Tolerant Fan. ASME GT2013-94656, June 2013.

[11] Marshall C. Galbraith, Steven R. Allmaras, and David L. Darmofal. A Verification Driven Process for Rapid Development of CFD Software. AIAA 2015-0818, January 2015.

[12] Marshall C. Galbraith, Steven R. Allmaras, and David L. Darmofal. SANS RANS Solutions for 3D Benchmark Configurations. AIAA 2018-1570, January 2018.

[13] Daniel Giesecke and Jens Friedrichs. Aerodynamic Comparison Between Circumferential and Wing-Embedded Inlet Distortion for an Ultra-High Bypass Ratio Fan Stage. ASME GT2019-90425, June 2019.

[14] Michael B. Giles and Niles A. Pierce. An Introduction to the Adjoint Approach to Design. *Flow, Turbulence and Combustion*, 65:393–415, 2000.

[15] Chana Goldberg, Devaiah Nalianda, Pericles Pilidis, and Riti Singh. Performance Assessment of a Boundary Layer Ingesting Distributed Propulsion System at Off-Design. AIAA 2017-5055, July 2017.

[16] Y. Gong. *Computational Model for Rotating Stall and Inlet Distortion in Multistage Compressors*. PhD thesis, Massachusetts Institute of Technology, Department of Aeronautics and Astronautics, 1999.

[17] D. K. Hall, E. M. Greitzer, and C. S. Tan. Analysis of Fan Stage Conceptual Design Attributes for Boundary Layer Ingestion. *Journal of Turbomachinery*, 139(7), 03 2017. 071012.

[18] D. K. Hall, E. M. Greitzer, and C. S. Tan. Mitigation of BLI Circumferential Distortion Using Non-Axisymmetric Fan Exit Guide Vanes. ASME, June 2022.

[19] D. K. Hall, E. M. Greitzer, A. Uranga, M. Drela, and S. A. Pandya. Inlet Flow Distortion in an Advanced Civil Transport Boundary Layer Ingesting Engine Installation. *Journal of Turbomachinery*, 144(10), 04 2022. 101002.

[20] David K. Hall, Aidan Dowdle, Jonas Gonzalez, Lauren Trollinger, and William Thalheimer. Assessment of a Boundary Layer Ingesting Turboelectric Aircraft Configuration using Signomial Programming. AIAA 2018-3973, June 2018.

[21] Brenda M. Kulfan. Universal Parametric Geometry Representation Method. *Journal of Aircraft*, 45(1):142–158, 2008.

[22] A.B. McKenzie. *Axial Flow Fans and Compressors: Aerodynamic Design and Performance*. Gower Technical, London: Ashgate, 1997.

[23] Theoklis Nikolaidis, Soheil Jafari, David Bosak, and Pericles Pilidis. Exchange Rate Analysis for Ultra High Bypass Ratio Geared Turbofan Engines. *Applied Sciences*, 10(21), 2020.

[24] Valdo Pagès, Pierre Duquesne, Stéphane Aubert, Laurent Blanc, Pascal Ferrand, Xavier Ottavy, and Christoph Brandstetter. UHBR Open-Test-Case Fan ECL5/CATANA. *International Journal of Turbomachinery, Propulsion and Power*, 7(2), 2022.

[25] Andreas Peters. *Ultra-Short Nacelles for Low Fan Pressure Ratio Propulsors*. PhD thesis, Massachusetts Institute of Technology, Department of Aeronautics and Astronautics, 2014.

[26] A Plas, D Crichton, M Sargeant, T Hynes, E Greitzer, C Hall, and V Madani. Performance of a Boundary Layer Ingesting (BLI) Propulsion System. AIAA 2007-450, January 2007.

[27] Philippe R. Spalart and Steven R. Allmaras. A One-Equation Turbulence Model for Aerodynamics Flows. *La Recherche Aérospatiale*, 1:5–21, 1994.

[28] Tze Sing Tse and Cesare A. Hall. Flow Field and Power Balance of a Distributed Aft-fuselage Boundary Layer Ingesting Aircraft. AIAA 2020-3779, August 2020.

[29] F. M. White. *Viscous Fluid Flow*. McGraw Hill, New York, NY, 1974.

[30] Tianbo Xie and Alejandra Uranga. Development and Validation of Non-Axisymmetric Body-Force Propulsor Model. AIAA 2020-3686, August 2020.